Doctoral Thesis

Search for physics beyond the standard model in same-sign di-electron events at the LHC

Author(s):
Milenović, Predrag

Publication Date:
2011

Permanent Link:
https://doi.org/10.3929/ethz-a-007128845 →

Rights / License:
In Copyright - Non-Commercial Use Permitted →

ETH Library

Dissertation ETH Nr. 20107/2011

Search for physics beyond the Standard Model in same-sign di-electron events at the LHC

A dissertation submitted to the

ETH Zürich

for the degree of

Doctor of Sciences

presented by

Predrag Milenović

Magister of Physics, University of Belgrade

citizen of Serbia.

accepted on the recommendation of

Prof. Dr. Günther Dissertori examiner
Prof. Dr. André Rubbia co-examiner
Prof. Dr. Petar Adžić co-examiner

2011

Zusammenfassung

Die Resultate, dir in dieser Dissertation präsentiert werden, wurden vom Autor erarbeitet während seiner wissenschaftlichen Forschungstätigkeit im Gebiet the experimentellen Hoch-Energie Physik als Mitglied des Instituts für Teilchenphysik an der ETH Zürich. Die experimentellen Messungen wurden mit dem "Compact Muon Seleniod" Experiment (CMS) am CERN durchgeführt, dies in enger Zusammenarbeit mit Forschern von der ETH Zürich und der CMS Kollaboration.

Im ersten Teil der Arbeit werden die grundsätzlichen Konzepte des "Large Hadron Colliders" (LHC) und des CMS Experiments erklärt, sowie die zum Verständtnis der Arbeit notwendigen technischen Details erläutert. Fortfolgend begründen wir die Notwendigkeit eines ausgeklügleten Kontroll- und Sicherheitssystems für das elektromagnetische Kalorimeter (ECAL) des CMS Experiments, und beschreiben die Arbeit des Autors während der Entwicklung und der Realisierung dieses Systems. Diese Arbeit beinhaltet die Entwicklung des ECAL Sicherheits Systems (ESS), das Testen dessen Prototypen, die Implementierung dessen genauer Funktionsweise, sowie dessen Einführung und Unterhalt im CMS Experiment. Im Speziellen beinhaltet die Arbeit die Entwicklung von redundanten Hardware Systemen für das Auslesen der Sensoren Daten, sowie der entsprechend notwendigen ESS Kommunikationsprotokolle.

Im zweiten Teil dieser Dissertation wird das Standart Modell der Teilchenphysik erklärt, auf die wichtigsten seiner Imitationen hingewiesen und Studien der Teilcheninteraktionen im TeV Bereich motiviert. Die minimale supersymmetrische Erweiterung des Standard Modells wird im Detail besprochen und eine Strategie für die Suche nach physikalischen Phänomenen solcher supersymmetrischen und ähnlicher Erweiterungen des SM dargelegt. Besondere Gewichtung erhält die Erklärung einer Methode zur Abschätzung des Untergrunds in der Suche nach neuer Physik in Kollisionsereignissen mit leptonischen Endzuständen. Im letzten Teil wird eine Datenanalyse zur Suche nach solchen Phänomenen, die über das SM der Teilchenphysik hinausgehen vorgestellt, die im Jahre 2010 mit $35\,\mathrm{pb}^{-1}$ ausgetragen wurde. In dieser Suche nach neuer Physik in Kollisionsereignissen mit zwei gleich geladener Leptonen wird die oben genannt Methode zur Abschätzung des Standard Modell Untergrunds erfolgreich angewandt. Da keine signifikante Abweichung von dem erwarteten Untergrund des Standard Modells gefunden wurde, konnten die Resultate der Analyse dazu verwendet werden, theoretische Modelle der neuen Physik einzuschränken. Im Falle der sogenannten eingeschränkten minimalen supersymmetrischen Erweiterung des Standard Modells konnten Beschränkungen an das Modell gesetzt werden, die diejenige früherer Experimente übertreffen.

Summary

The work and results presented in this thesis have been accomplished as a part of the scientific research the author has performed in the field of experimental high energy physics as a member of the Institute for Particle Physics at ETH Zürich. The research has been conducted with the **C**ompact **M**uon **S**olenoid (CMS) experiment in CERN, in close collaboration with colleagues from the ETH Zürich and the CMS collaboration.

In the first part of the thesis we present the concepts of the **L**arge **H**adron **C**ollider (LHC) and the CMS experiment and introduce the technical details necessary to understand all the aspects of the work and the results presented in the thesis. We then explain the necessity for a sophisticated Detector Control and Safety System of the **E**lectromagnetic **Cal**orimeter (ECAL) of the CMS experiment and present the work that has been accomplished during the realisation of the system. It includes the development of the **E**CAL **S**afety **S**ystem (ESS), testing of its prototypes, implementation of the distinctive solutions and the commissioning and operation of the system within the CMS experiment. Some of the notable solutions include the development of the redundant hardware system for the sensor readout and the development of the dedicated ESS communication protocol. The system has been in full operation and performing remarkably well since the year 2008. This work has been performed in a close collaboration with colleagues from the CMS Belgrade Group, University of Belgrade.

In the second part of the thesis we describe the concepts of the **S**tandard **M**odel (SM) of particle physics, outline its main limitations and present the motivation to study the physics of particle interactions at energies above TeV. We describe in detail the Supersymmetric extension of the Standard Model and present a strategy for search for physics phenomena that can be described by this class of models. We argue that the strategy allows for search for several other classes of extensions of the SM. We then present an extended experimental method for the prediction of rates of background processes with one or more fake leptons. The method provides a scheme for handling different types of backgrounds independently and has been developed together with other colleagues from ETH. Finally, we present the full physics analysis performed in the year 2010 with the goal to search for physics beyond the SM in events with a pair of same-sign electrons. The analysis has been performed with sample of data collected in proton-proton collisions corresponding to an integrated luminosity of $35\,\mathrm{pb}^{-1}$. It has been conducted in a direct collaboration with other colleagues from CMS collaboration as a part of the broader combined CMS analysis. No excess over the expected number of events in the signal region has been observed and the combined results of the CMS analyses have been used

to set new limits on the theoretical models for physics beyond the SM. In the case of the constrained Minimal Supersymmetric extension of the SM, we have extended the limits previously imposed by the other experiments.

Contents

II   Search for physics beyond the Standard Model   57

5   Physics at the Large Hadron Collider   59

6   Event reconstruction   89

Part I

The Experimental Apparatus

Chapter 1

The Large Hadron Collider

> ...like smashing two Swiss watches together
> to figure out how they work.
> R Feynman, describing proton-proton machines[1]

During the course of the 20th century, physicists have been inexorably pushing back the frontiers of our understanding of the world of subatomic particles. In the first decades of this pursuit to understand the Nature at subatomic scales, scientific experiments were largely based on natural radioactive sources and cosmic rays. It took almost a half of the century before man-created particle accelerators entrenched as primary tools and became indispensable in searches for new phenomena in particle physics.

Today, we can distinguish between two main approaches in the design of particle accelerators and corresponding physics experiments: accelerators with fixed-target experiments and colliders. In the first approach only one beam of particles is accelerated to a desired energy and scattered against a fixed block of a target matter. In the collider approach two beams of particles are accelerated separately to desired energies and then brought into collisions.

In either of these approaches, there are three key aspects which define the discovery potential and the performance of an accelerator and its experiments. The first key aspect is the maximum energy which particles can obtain in the accelerator. This energy directly determines the scientific reach of the experimental programme: if the energy of probing particles is extremely high, the targeted matter can be examined at very short distances. Furthermore, if thresholds of potential discoveries are defined by minimum energy needed to induce new phenomena, the higher the collision energy, the wider the range of new effects that can be explored.

In order to draw meaningful conclusions from experimental results physicists need to collect data that have sufficient statistical accuracy. For this reason, the second key aspect in an accelerator design is the overall interaction rate that it can provide to experiments. The likelihood of producing a certain reaction is described by a number σ called the cross-section, which is the effective area a target particle presents to an incident particle for

---

[1]as quoted in James Gleick, Genius: The Life and Science of Richard Feynman, 1992

that reaction to occur. A number which describes how frequently per unit area incident and target particles have a chance to encounter each others is called the instantaneous luminosity $\mathcal{L}(t)$. The overall rate of an interaction $X \to Y$ is then the product of the cross section $\sigma(X \to Y)$ of that reaction and the accelerator instantaneous luminosity $\mathcal{L}(t)$. Consequently, the total number of scattering reactions in a time-interval $t_2 - t_1$ for a certain process $X \to Y$ is simply given as:

$$N_{reactions}(X \to Y) = \int_{t_1}^{t_2} \sigma(X \to Y)\mathcal{L}(t)dt = \sigma(X \to Y) \cdot \mathcal{L}_{int}(t_1, t_2), \qquad (1.1)$$

where we assume that the cross-section $\sigma(X \to Y)$ does not depend on time and $\mathcal{L}_{int}(t_1, t_2)$ is the integrated luminosity for a given time-interval $[t_1, t_2]$. The equation (1.1) quantitatively expresses how the requirement for high statistical accuracy of experimental data actually translates into the requirement for high integrated luminosity of an accelerator.

The third key aspect in an accelerator design is the type of particles that will collide. The choice of the colliding particles is important since it directly determines the type of physical interactions that can occur in collisions and, hence, determines the spectrum of phenomena that can be studied. In addition, the particles participating in collisions can be composite objects themselves, such as protons or heavy ions. In this case, the particle energy is shared among its constituents and the energy available to induce new phenomena is lower and determined by the energy in the reference frame of colliding constituents, and not in the frame of the parent particles. Finally, the combination of signs of charges of colliding particles puts technical restrictions on the configuration and implementation of the magnetic field in a circular accelerator apparatus.

In addition to these aspects, there are many other technical aspects that need to be evaluated carefully when considering the accelerator design. These include the choice between the linear and circular accelerator geometry, the radiation energy loss per turn in case of circular accelerators, the percentage of time the collisions are actually taking place, as well as the level of various background interactions.
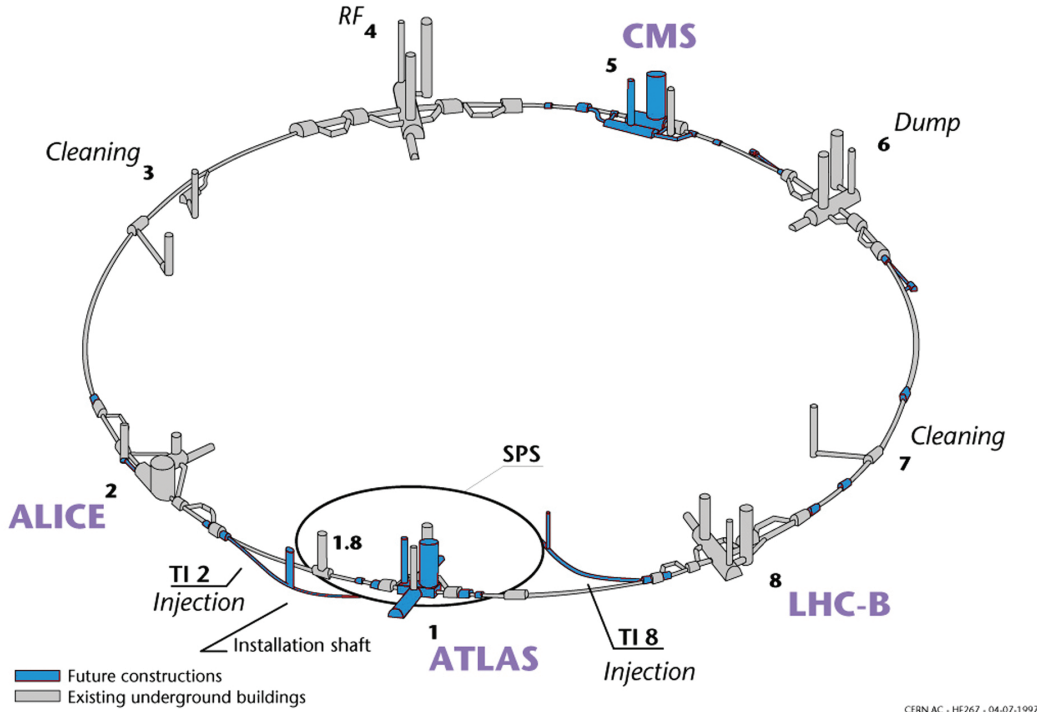
In the following two sections we will present the design of the LHC [1] at the **C**onseil **E**uropéen pour la **R**echerche **N**ucléaire (CERN) and how the key aspects described above have led to the particular choice of technologies employed at the LHC. We will primarily discuss the design parameters of the LHC which are important for its experimental programme and give an overview of the collider performance during its operation in years 2010 and 2011.

1.1   Collider design and operational parameters

The general aim of the LHC is to enable experimental studies of particle physics phenomena at energy scales of a few TeV, and search for rare processes with cross-sections below $1 \times 10^{-39} \, \text{cm}^2$ [2, 3]. In order to fulfil these goals the LHC has been designed as a two-ring superconducting accelerator and a collider capable of providing proton-proton collisions with a centre of mass energy of up to 14 TeV and with instantaneous luminosity as high as

$\mathcal{L} = 10^{34}\,\mathrm{cm}^{-2}\,\mathrm{s}^{-1}$ [4, 5, 6]. The LHC machine and supporting services have been installed and commissioned in the period between years 2001 and 2008 in the 26.7 km long circular tunnel which was constructed in CERN for the **L**arge **E**lectron-**P**ositron Collider (LEP) between years 1984 and 1989 [7, 8]. The plane of the tunnel is situated at a depth between 45 m and 170 m below the surface with an inclination of 1.4% towards the Lake of Geneva.
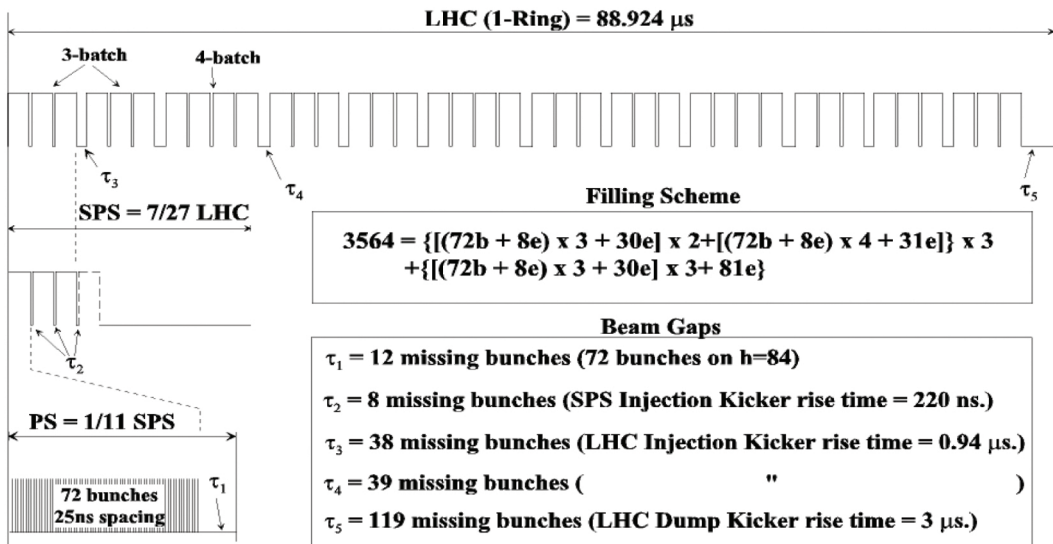
Figure 1.1: The LHC underground installations with locations of the four main experiments (ATLAS, ALICE, CMS, LHCb) and locations of systems for cleaning, acceleration (RF) and dumping of proton beams. Adapted from [1].

The entire LHC is composed of eight 3 km long arc sections and eight 528 m long straight sections named **I**nsertion **R**egions (IRs) [4, chapter 3]. These eight IRs are sections of the LHC where the physics experiments and systems for acceleration, cleaning and dumping of proton beams are installed (Figure 1.1). The eight arc sections of the LHC are identical and composed of 23 cells. Each cell is 107 m long and contains three magnetic dipole systems which provide the field necessary to bend beams along a circular orbit, and two magnetic quadrupole systems which provide the field necessary to focus beams alternately in the horizontal and vertical planes. Furthermore, each of these cells contains several other systems which provide a higher-order multipole magnetic field necessary for fine corrections of the beam orbit [4, chapter 7].

In order to obtain proton beams with energy of 7 TeV, the complete procedure of proton acceleration in the LHC is divided in two phases: the pre-acceleration phase per-

formed in several stages by the complex of existing accelerators[2] in CERN and the main acceleration phase performed at the LHC itself. At the first step of the pre-acceleration phase protons are obtained from hydrogen atoms in a duoplasmatron device and accelerated in **Lin**ear **Ac**celerator **2** (LINAC2) to 50 MeV [6, chapter 3]. After being grouped in bunches and accelerated in the LINAC2, protons are injected into four **P**roton **S**ynchrotron **B**ooster (PSB) rings, ramped up to 1.4 GeV, and then transferred to the **P**roton **S**ynchrotron (PS) where their energy is further increased to 25 GeV. During this process in PSB and PS protons are squeezed in very tight bunches and a base bunch structure of the LHC is prepared. In periods when the LHC is operated at nominal luminosity the base bunch structure coming out of the PS is planned to be a sequence of 72 bunches with length of 4 ns and time spacing of 25 ns.

Figure 1.2: Time structure of proton bunches in the PS, SPS and LHC. In total, 2808 bunches are injected per proton beam. The time needed to fill one LHC ring is approximately 4 minutes [1].

In the last step of the pre-acceleration phase several batches of base-structure bunches are dispatched from the PS to the SPS, accelerated to 450 GeV and transferred into the two beam lines of the LHC. At the end of this step a total of 2808 bunches, each containing about 1.15×10^{11} protons, should be circulating in each of the two LHC beam lines. Figure 1.2 shows in a schematic way the time structure of the LHC proton bunches, while the details of the complete pre-acceleration phase and the bunch time structure can be found in the volume 3 of the LHC Design Report [6].

The main acceleration phase is performed at the LHC beam acceleration system which is installed at the IR4. This acceleration system gradually ramps up the proton energy from 450 GeV to 7 TeV using a 400.8 MHz superconducting **R**adio **F**requency (RF) cavity system [4, chapter 6]. The exact RF frequency of 400.8 MHz has been chosen to match

---

[2]The existing accelerators needed to be upgraded to support the LHC operation.

the bunch length in order to ensure that injected beams are captured with minimal losses. The eight RF cavities with $5.5\,\mathrm{MVm}^{-1}$ field strength provide an acceleration voltage of up to $16\,\mathrm{MV}$ per beam.

In order to keep the $7\,\mathrm{TeV}$ proton beams on projected quasi-circular orbits, the LHC magnetic dipoles need to be able to produce a magnetic field of $8.33\,\mathrm{T}$ corresponding to an electrical current of around $11\,700\,\mathrm{A}$. For this reason, the LHC magnetic dipoles have been designed and implemented as Niobium-Titanium (NbTi) superconducting coils and have to be cooled down to and operated at a temperature of $1.9\,\mathrm{K}$ [4, chapter 7]. The development of the technology to produce this type of superconducting cables and implement them in 1232 magnetic dipoles along the $26.7\,\mathrm{km}$ long tunnel was one of the major challenges of the entire LHC project.

Once accelerated to the energy of $7\,\mathrm{TeV}$, the LHC proton bunches are focused to the transverse size of $16\,\mathrm{\mu m}$ and brought into collision at four IRs, commonly named **I**nteraction **P**oints (IPs). In order to avoid direct collisions of bunches outside of the centres of IPs, beams are directed onto each other with an angle of $285\,\mathrm{\mu rad}$ in the vertical plane. The instantaneous luminosity of the LHC at an IP fully depends on the beam bunch structure, beam parameters and how well these can be controlled. In the case when beams have approximately Gaussian spatial distributions and equal parameters, the instantaneous luminosity can be expressed as:

$$\mathcal{L} = \frac{N_b^2 n_b f_{rev}}{4\pi(\sigma_{xy})^2} F, \tag{1.2}$$

where N_b is the number of protons per bunch, n_b is the total number of bunches which collide at the given IP, f_{rev} is the bunch revolution frequency and σ_{xy} is the r.m.s. of the transverse beam size at that IP. The factor F is the geometrical luminosity reduction factor ($F < 1$) which originates from the non-zero beam crossing angle.

The LHC beam parameters have been optimised to maximize the expression (1.2) and to achieve the required luminosity at each IP taking into account various performance limitations and machine boundary conditions [4, chapter 7]. Table 1.1 summarises values of beam parameters which need to be reached in order to achieve a peak luminosity of $1 \times 10^{34}\,\mathrm{cm}^{-2}\mathrm{s}^{-1}$.

The instantaneous luminosity of the collider is not constant over the time, but it slowly degrades due to head-on bunch collisions, multiple Coulomb scattering within each bunch and scattering of protons on residual gas atoms inside of beam pipes. For this reason, the maximum integrated luminosity achievable by the collider depends on the length of its luminosity lifetime, on the actual choice of the length of collision runs, and on practically attainable beam turnaround time[3]. It is expected that for the optimal choice of run times, assuming that the LHC will be operated for about 200 days per year, the collider can achieve a total integrated luminosity of 80 to $120\,\mathrm{fb}^{-1}$ per year. The detailed analysis of the LHC performance and its efficiency can be found in [1, chapter 3].

Table 1.1 shows that high luminosity at the LHC is practically achieved by colliding

---

[3]time between beam dump and the moment when beams are again stable and ready for collisions.

a very large number of very densely packed proton bunches. The direct consequence of having very high density proton bunches is that the actual number of proton-proton interactions per bunch crossing becomes very high. These interactions are dominated by

Table 1.1: The LHC operational parameters for 7 TeV beams at peak luminosity at interaction points of its high luminosity experiments

Beam parameter	Symbol	Parameter value
Number of protons per bunch	N_b	1.15×10^{11}
Number of bunches	n_b	2808
Revolution frequency	f_{rev}	11.245 kHz
Full crossing angle at IP	θ_c	285 μrad
R.m.s. of bunch length	σ_z	7.55 cm
R.m.s. of transverse bunch size	σ_{xy}	16.7 μm
Crossing angle factor	F	0.836
Instantaneous luminosity per bunch	$\mathcal{L}$/bunch	3.56×10^{30} cm^{-2}s^{-1}
Instantaneous luminosity	$\mathcal{L}$	1×10^{34} cm^{-2}s^{-1}

the inelastic proton-proton scatterings which produce relatively low momentum particles in the final state and have a large cross-section $\sigma^{pp}_{inelastic}$ of about 75 mb[4] [9]. In the case of a peak luminosity of 1×10^{34} cm^{-2}s^{-1}, the number of these "non-hard" proton scatterings per one bunch crossing, the $N_{p.u.}$, is approximately:

$$N_{p.u.} = \frac{\mathcal{L}}{n_b} \frac{\sigma^{pp}_{inelastic}}{f_{rev}} \approx 25.3.$$

Therefore, in case of the nominal beam parameters experiments should expect to have in average about 25 "non-hard" proton scattering events overlaid on top of any hard proton-proton scattering. This phenomenon is commonly named the "pile-up" effect and, together with the short time gap of 25 ns between collisions, has imposed serious restrictions on the design of experiments at the LHC. In chapters 2 and 3 we will discuss in details how these, as well as other restrictions, have dictated the design and performance of the CMS experiment and its electromagnetic calorimeter.

1.2 The physics experiments

The LHC, designed as a collider with unprecedented performance, offers an opportunity for a rich experimental programme in several unexplored domains of particle physics. In order to fully exploit this scientific potential, four large-scale and three smaller experiments have been constructed, commissioned and are being operated today at four IPs of the LHC.

---

[4]in the case of the proton-proton collisions at a centre-of-mass energy of 7 TeV.

The two largest experiments are the ATLAS [10] and CMS [11] experiments, installed at the IP1 and the IP5, respectively. They have been designed as two complementary experiments with very broad scientific programme, including both searches for new phenomena and precision measurements in particle physics.

The third large-scale experiment is the LHCb experiment, which has been installed at the IP8. It has been primarily designed to study CP violation in B meson decays [12] and the objective of the LHC is to provide to this experiment a peak instantaneous luminosity of $1 \times 10^{32}\,\mathrm{cm}^{-2}\mathrm{s}^{-1}$.

The fourth large-scale experiment is the ALICE experiment [13], installed at the IP2. It is a dedicated heavy-ion collision experiment which should study the behaviour of the nuclear matter at very high energies and densities, and in particular it should explore the formation of the quark-gluon plasma. The goal of the LHC is to provide to the ALICE experiment a peak luminosity of $1 \times 10^{27}\,\mathrm{cm}^{-2}\mathrm{s}^{-1}$ for the nominal accelerator operation with Pb ions. More details on the operation of the LHC as an ion collider and the values of beam parameters which need to be achieved in order to reach the nominal mode of operation can be found in [4, chapter 21].

In addition to these four large experiments, the LHC hosts three smaller-scale experiments: TOTEM [14], LHCf [15] and the recently approved MoEDAL experiment [16]. The TOTEM experiment has been installed at the IP5 in the vicinity of CMS, and it is dedicated to the measurement of the total cross-section and study of the elastic and diffractive scattering of protons. The LHCf experiment has been designed to study neutral hadrons emitted in the very forward region of proton collisions and it has been installed at the IP1 in the vicinity of ATLAS. Its physics goal is to provide data for calibration of hadron interaction models that are used in the study of extremely high-energy cosmic rays. The purpose of the MoEDAL experiment is to search for massive stable or pseudo-stable particles and magnetic monopoles, and it has been installed at the IP of the LHCb experiment.

In chapters 2 and 3 we will present the details of the design of the CMS experiment and discuss thoroughly its most important performance issues. The details on the design and performance of the other six experiments can be found in references specified above.

1.3 Performance during operation in 2010 and 2011

The construction phase of the **L**arge **H**adron **C**ollider (LHC) was officially completed on the 10th September of 2008, after almost 15 years of prototyping of required technologies and about 8 years of installation and commissioning of collider components. Unfortunately, on the 19th September of 2008 a serious accident occurred in the IR5 of the LHC [17]. As a direct consequence, the plans for the LHC operation had to be considerably altered and rescheduled. The new plans have established that the LHC should provide proton beams of 3.5 TeV during its initial operation from 2010 until 2012, and that it will be prepared to operate with proton beams of up to 7 TeV only after a long shut-down period in 2013 and 2014 [18].

The first planned collisions between proton beams at a centre-of-mass energy of 7 TeV took place on the 30th March 2010, setting a new record for the highest energy achieved in man-made particle collisions. During the course of the year 2010, the main emphasis in LHC operations was put on the commissioning of the collider and on a gradual increase of its instantaneous luminosity, while still providing its experiments with an integrated luminosity of up to 100 pb^{-1}.

Table 1.2: The performance figures for 3.5 TeV beams during the LHC operation in 2010 and 2011 (as of 1st June 2011) [19, 20]. By the end of 2011, the LHC delivered integrated luminosity of 5.57 fb^{-1}, with the peak instantaneous luminosity being 3.6×10^{33} cm^{-2}s^{-1}.

Performance figure	Units	in 2010	by mid 2011
Peak stable luminosity	cm^{-2}s^{-1}	2.1×10^{32}	12.6×10^{32}
Maximum luminosity delivered in one fill	pb^{-1}	5.62	37.65
Total luminosity delivered	pb^{-1}	47	560
Maximum number of colliding bunches		348	1042
Max average events per bunch crossing		2.67	8.93
Longest time with stable beams per fill	hours	18.3	17.9
Shortest turnaround time to stable beams	hours	2.75	2.4

By the end of the year 2010, the LHC was showing a very good performance and it was routinely operating with bunches of the nominal intensity of 1.15×10^{11} separated by time gaps of 150 ns. The peak instantaneous luminosity of 2.1×10^{32} cm^{-2}s^{-1} was achieved with beams containing 348 proton bunches. During this period, the LHC delivered 47 pb^{-1} of integrated luminosity to ATLAS and CMS, enabling them to perform a range of important physics measurements and to initiate first searches for new phenomena. Some of the most important LHC performance figures are presented in Table 1.2, while the detailed information on the collider operation in the year 2010 can be found in the proceedings of the Chamonix 2011 workshop on the LHC performance [19].

In March 2011, the LHC resumed its operation with the goal to further improve its performance and to achieve the peak instantaneous luminosity of 5×10^{33} cm^{-2}s^{-1} by the end of the year 2012. In the period until the 1st June 2011, the LHC has already demonstrated an excellent performance and achieved a peak instantaneous luminosity of 1.26×10^{33} cm^{-2}s^{-1} with beams containing 1042 proton bunches separated by time gaps of 50 ns. By the end of the year 2011, the LHC has delivered 5.57 fb^{-1} of integrated luminosity to its high luminosity experiments, reaching the peak instantaneous luminosity of 3.6×10^{33} cm^{-2}s^{-1}. This amount of delivered collision data should allow a wide range of topics from the LHC experimental programme to be studied thoroughly. More details on the performance of the collider during the first half of the year 2011 and on plans for future operation of the LHC can be found in [20].

Results of the physics analysis presented in Part II of this thesis are obtained by

analysing collision data collected during the LHC operation in the year 2010. The prospects of the analysis method presented in the Part II are discussed in the light of the expected LHC performance in years 2011 and 2012.

Chapter 2

The Compact Muon Solenoid experiment

> No one believes a hypothesis except its originator
> but everybody believes an experiment except the experimenter.
> W. Beveridge [1], 1950.

2.1 The experimental challenges

Some of the most demanding challenges for high-luminosity experiments at the LHC have come from the collider design itself and the fact that it collides very densely packed bunches of protons with time gaps of only 25 ns. These challenges had a major impact on the design of the experiments with three important consequences.

First, each of the experiments had to be able to efficiently disentangle signals coming from two or more successive bunch crossings. In order to fulfil this requirement, it was an imperative to use or to develop sophisticated detector technologies and highly performing readout electronics which are capable of registering and processing signals from collisions on a time scale of 20-50 ns. Second, the experiments had to be implemented in a way that minimises the probability for particles created in pile-up events to traverse the same detector element as a particle coming from a potentially interesting hard-scattering event. For this reason, the experiments had to be designed with a very fine readout granularity. Finally, the experiments were restricted to develop or employ only those detector technologies and readout electronics that are capable of sustaining enormous fluxes of particles over extended periods of the experiment operation. This was a necessary condition in order to minimize the damage of the detector material structure that could lead to a deterioration of the performance and, eventually, a break-down of the detector.

These experimental challenges were entirely driven by the design of the collider and did not depend directly on the research objectives of the particular experiment. In addition, each experiment at the LHC had to fulfil specific requirements that were dictated by

---

[1]W.I.B. Beveridge, The Art of Scientific Inverstigation, Hainemann, London 1950.

research objectives of its own scientific programme. In the following sections we will present the most important requirements imposed on the CMS experiment by its scientific programme and how these have led to the final design concept of the experiment. We will present the design of each of its detector systems and give a brief overview of its performance during the operation in the year 2010.

2.2 Design of the experiment

The scientific programme of the CMS experiment covers a broad spectrum of topics from the precision measurements of various phenomena in particle physics at energies of a few $100\,\mathrm{GeV}$ to the searches for new particles and phenomena at energies of up to a few TeV [11]. In order to be capable of conducting its scientific programme successfully, the experiment had to meet several demanding performance requirements.

First, the experiment had to be able to efficiently detect and measure the leptons produced with a relatively low momentum in the decays of heavy-flavour hadrons, as well as the leptons produced with a very high momentum in the decays of hypothetical particles which could have masses of up to a few TeV. This requirement implied the necessity for an experiment with high performance of the identification of charged leptons and a very good relative resolution for the measurement of their transverse momentum in the range from a few GeV up to a few TeV.
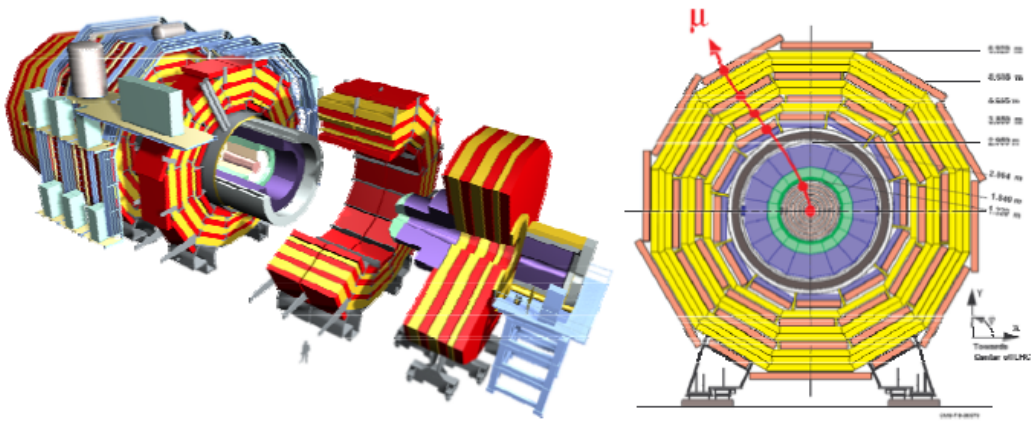
Second, the experiment had to ensure that the reconstructed mass spectrum of the most important hypothetical particles could be clearly observable above the spectrum continuum that originates from the irreducible background processes. In order to achieve this, the experiment needed to have an excellent mass resolution of about 1% for all the particles of masses up to a few hundreds GeV that decay into photons, electrons or muons.

Third, it was essential to provide a reliable measurement of the total transverse energy of all particles produced in an event and detected by the experiment. This ability allows the experiment to infer properties of particles which weakly interact with the matter by observing the imbalance of the total transverse energy in the event. The way to achieve this was to design the calorimetry of the experiment that could measure particle energies in the 360 degrees of the azimuthal angle and down to a fraction of a degree in the polar angle with respect to the incoming beams.

Fourth, it was crucial to be able to discriminate between hypothetical heavy particles decaying into photons over similar hadronic processes. This requirement implied an excellent performance in separation of electron and photons from other hadronic particles. In addition, the experiment required a very good identification of jets of particles originating from heavy quarks and tau leptons.

Finally, the experiment had to be able to reduce the interaction rate of 1×10^9 events/s to an affordable data storage rate of a few hundred recorded events per second. For this reason, a very fast, very selective and at the same time very efficient system which will trigger the event reconstruction only in case of potentially interesting scatterings had to be designed.

In order to be able to cope with all experimental challenges and to be able to meet all the performance requirements, the CMS experiment [11] has been designed as a multi-layer system of detectors with a high-field magnetic solenoid which houses a silicon-based tracking system, a homogeneous scintillating-crystals-based electromagnetic calorimeter and a brass-based hadronic calorimeter, as well as the iron return yoke placed outside of the solenoid and equipped with a redundant muon detection system. The experiment has a total length of 21.6m, a diameter of 14.6m and weights 12.500 tons. All subsystems of CMS are interconnected by means of the data acquisition and trigger system.

Figure 2.1: Perspective and transversal views of the CMS experiment and its multi-layer system of sub-detectors together with the adopted coordinate system [11].

The CMS experiment has adopted a right-handed coordinate system with its origin centred at the nominal collision point at the geometrical centre of the experiment, the y-axis pointing vertically upward, and the x-axis pointing radially inward, toward the centre of the LHC. The z-axis lies along the LHC beam axis. The angle θ is the polar angle with respect to the z-axis and ϕ is the azimuthal angle with respect to the LHC plane. The rest frame of the hard collision is generally boosted relative to the lab frame along the beam direction. For this reason, the detector solid angle segmentation is considered in units of "pseudorapidity", which is approximately invariant under boosts along the z direction. The pseudorapidity η is related to the polar angle θ and is defined as $\eta = -\ln(\tan(\theta/2))$. The transverse momentum component orthogonal to the z-axis is given by $p_T = p\sin\theta$ and similarly $E_T = E\sin\theta$ represents the transverse energy of a physics object with the measured energy E.

2.2.1 The magnet system

The CMS magnet has been designed as a 13 m long, 4 T superconducting solenoid with the main goal to provide a sufficiently large trajectory bending power in the regions of the tracking and the muon system. It represents the heart of the experiment and

the configuration of its magnetic field has significantly influenced the overall design and attributes of the CMS apparatus.

The magnetic field of $4\,\mathrm{T}$ is necessary to provide sufficiently efficient momentum measurements and electromagnetic charge assignments both within the tracking system inside of the magnet and within the muon system outside of the magnet. The bore of the magnet consists of the 220 tonnes cold mass with the 4-layer winding made from a stabilised reinforced NbTi conductor. It had to be large enough to host the tracking system and both calorimeters in its interior. This requirement has imposed a direct demand on the size of the inner radius of the solenoid and consequently a direct demand on the volume of space and instrumentation which will be permeated with the magnetic field. The magnetic field of the CMS solenoid stores an enormous amount of energy, which amounts to about 2.6 GJ at the full current of $19.14\,\mathrm{kA}$.

The flux delivered by coils through the interior of the solenoid is returned through a massive 4-layer iron yoke composed of five barrel rings and two endcaps. This iron yoke houses the muon systems, both in the barrel and endcap parts of the experiment. For this reason, any muon traversing the detector experiences opposite deflections as it transits from the interior of the solenoid to the exterior (see Figure 2.1, right).

Due to several operational requirements, the CMS magnet has been operating with a magnetic field of $3.8\,\mathrm{T}$ during the data-taking periods in 2010 and 2011. A complete description and details of the design and the implementation of the CMS magnet, its specially constructed superconducting coils, as well as the complex procedures of the magnet operation can be found in [11] and references therein.

2.2.2 The tracking system

The CMS tracking system has been designed to provide a precise reconstruction of the trajectories and momenta of charged particles coming from collisions, as well as to help in identification of heavy particles which have a life time that allows them to travel a considerable distance from the collision point before decaying into lighter particles.
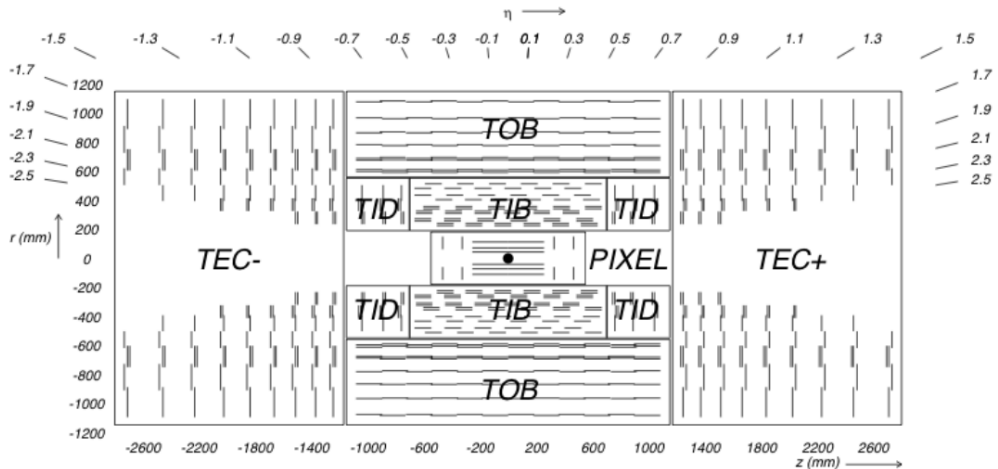
The system consists of two main components, shown schematically in Figure 2.2 [11]. The innermost component is a silicon pixel detector which covers the region from 4 to 15 cm in the radial direction, and 49 cm on either side of the collision point along the LHC beam axis. Outside of the pixel detector lies a silicon strip detector which covers the region from 25 to 110 cm in the radial direction, and up to 280 cm on either side of the collision point along the LHC beam axis.

The silicon pixel detector has 66 million active elements with the instrumental surface area of about $1\,\mathrm{m}^2$. It has been designed to provide the determination of up to three high precision three-dimensional points of charged particles trajectories. The detector consists of three concentric cylindrical layers and four disks which close the barrel ends. The barrel layers have an active length of 53 cm and are located at average radii of 4.3, 7.3, and 10.2 cm. The endcap disks occupy regions between radii 4.8 and 14.4 cm at mean longitudinal distances of 35.5 and 48.5 cm from the interaction point. The system provides an efficient three-hit coverage in the region of pseudo-rapidity $|\eta| < 2.2$ and efficient two-hit coverage

in the region $|\eta| < 2.5$. The 3.8 T magnetic field in CMS causes significant azimuthal Lorentz drift of the collected electrons which enhances the azimuthal charge sharing and therefore improves the resolution in that direction.

The silicon strip detector has 9.3 million active elements with the instrumental surface area of $198 \, \text{m}^2$. The detector consists of three large subsystems. The Tracker Inner Barrel and Disks (TIB/TID) extend in radius to 55 cm and are composed of four barrel layers, supplemented by three disks at each end. The TIB/TID delivers up to four measurements using $320 \, \mu m$ thick silicon microstrip sensors. The TIB/TID is placed within the Tracker Outer Barrel (TOB), which has an outer radius of 116 cm and extends to 118 cm in the z direction. The TOB consists of six barrel layers with $500 \, \mu m$ thick microstrip sensors. Beyond this z range, the Tracker EndCaps (TEC) instruments the region $124 < |z| < 280$ cm and $22.0 < r < 113.5$ cm. Each TEC is composed of nine disks that are instrumented with up to seven rings of radial-strip silicon detectors. The inner two layers of the TIB and TOB, the inner two rings of the TID and TEC, and the fifth ring of the TEC include a second microstrip detector module that is mounted back-to-back at a stereo angle of $100 \, \text{mrad}$ and that enables a measurement of the orthogonal coordinate. Assuming fully efficient planes and not counting hits in stereo modules, there are from 8 to 14 high precision measurements of track impact points in the region of $|\eta| < 2.4$.
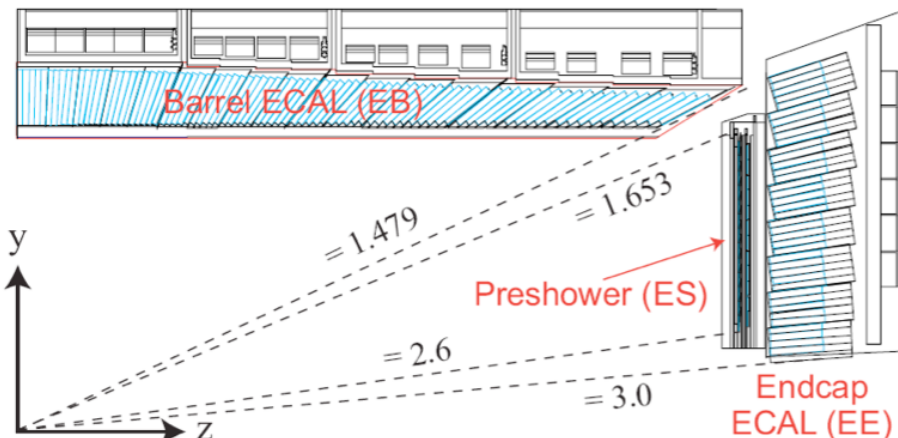
Figure 2.2: A longitudinal schematic view of the inner tracking system and multi-layer structure of its "pixel" and "silicon strip" sub systems [11].

There is a delicate balance between two intentions: to have enough material in order to make the intended measurements of charged particles and not to have too much material in order to avoid unwanted interactions (e.g., nuclear interactions, bremmsstrahlung, photon conversions, multiple particle scattering). The CMS tracking system has been optimised for such a balance, providing high-precision tracking and vertex measurements at the cost of 0.4-1.8 radiation lengths depending on the pseudorapidity.

The CMS tracking system also allows for the reconstruction of several other observ-

ables. One of the most important is the reconstruction of the event's primary vertex (PV). Using the information from several reconstructed charged tracks, the location of the primary collision in three-dimensional space can be measured with high precision. With high luminosity conditions, multiple primary vertices are expected from pile-up. Thus, it is vital to be able to match charged tracks accurately to these respective vertices for a consistent event reconstruction. Another important ability is to reconstruct secondary vertices (SV) originating from short-lived, heavy-flavor decays (e.g., B and D mesons). These are essential for the identification of particle jets originating from heavy quarks and the reconstruction of tau leptons. Related to secondary vertex reconstruction is the measurement of the transverse impact parameter d_0, which is useful to discriminate muons and electrons of resonance decays from those of delayed decays of heavy-flavor mesons.

In addition, the wide linear range of the strip channel output provides a measure of energy loss per unit of path length. For a given medium, this observable depends largely on the velocity of the traversing particle and, when combined with the measured momentum of a track, enables one to determine the mass and eventually identify the traversing particle. More details on the tracker implantation and its performance during its operation in the year 2010 can be found in [21, 11].

Figure 2.3: Longitudinal schematic view of the electromagnetic calorimeter and its pre-shower sub detector [11].

2.2.3   The electromagnetic calorimeter

The CMS electromagnetic calorimeter (ECAL) has been designed as a homogeneous crystal calorimeter with excellent energy resolution and very high granularity. The design has been largely motivated by the expected intense operating conditions of the LHC and the strict performance requirements necessary to study photon production at the LHC, in particular to pursue the discovery of the Higgs boson decay into two energetic photons ($H \rightarrow \gamma\gamma$). The calorimeter has been organized into two regions of pseudorapidity: the

barrel ($|\eta| < 1.479$) and the endcap ($1.479 < |\eta| < 3.0$), constructed with lead tungstate crystals that are arranged in a projective geometry. The crystals are 25.8 radiation lengths long in the barrel, and 24.7 radiation lengths in the endcap region. In the barrel region the front face of the crystal is approximately $22 \times 22\,\mathrm{mm}^2$, corresponding to a granularity of $\Delta\eta \times \Delta\phi = 0.0174 \times 0.0174$.

In the endcap region there is a lead-silicon-strip Preshower (ES) detector consisting of two orthogonal silicon strip detectors that have a strip pitch of 1.9 mm. One plane of the detector is at a depth of 2 radiation lengths and the other is at a depth of 3 radiation lengths. The **A**valanche **P**hoto **D**iodes (APDs) are used to detect and amplify the scintillation light in the barrel region and **V**acuum **P**hoto **T**riodes (VPTs) while used in the endcap region of the ECAL. The longitudinal schematic view of the electromagnetic calorimeter and its pre-shower sub-detector is shown in Figure 2.3. A more detailed description of the Electromagnetic Calorimeter and especially the parameters that have impact on its performance will be presented in the following chapter.

2.2.4 The hadronic calorimeter
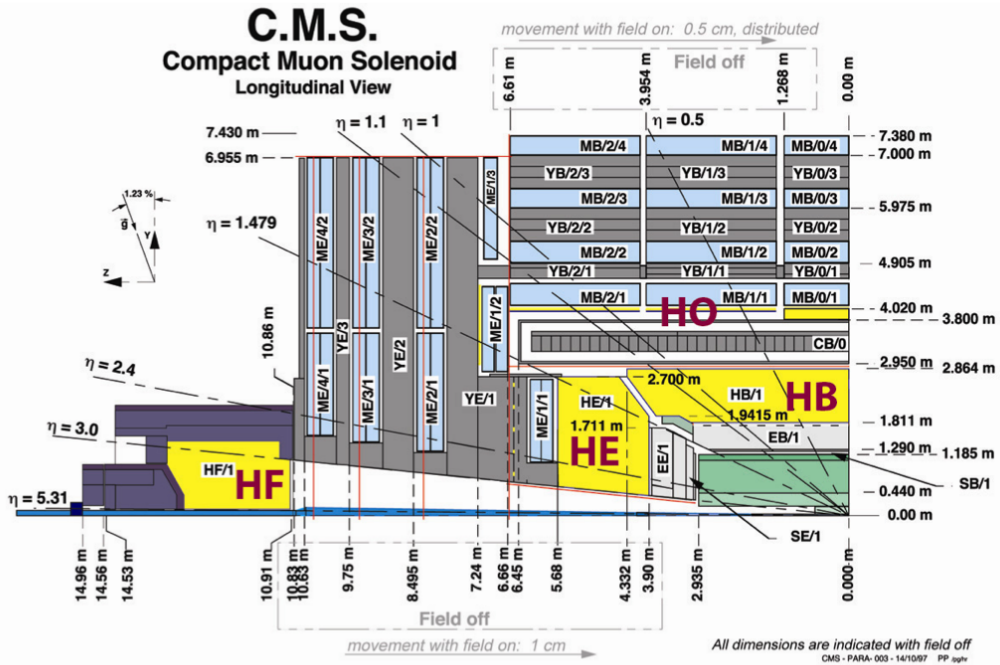
The **H**adronic **Cal**orimeter (HCAL) has been designed to completely absorb neutral and charged hadrons and measure their absorbed energies, providing the basis for the reconstruction of jets of particles originating from quarks and gluon, as well as the calculation of the missing transverse momentum. It is located behind the ECAL and consists of four sub-detector components. These are commonly referred to as the HCAL barrel (HB), endcap (HE), forward (HF), and outer (HO). They cover a total pseudorapidity range up to $|\eta| < 5.0$, making the CMS detector almost perfectly hermetic (see Figure 2.4).

The HB spans 1.77 m to 2.95 m in radius, and provides about 5.8 (10.6) interaction lengths at $|\eta| = 0(1.3)$. In cases where a single hadron carries a large energy from the collision event, the hadronic shower induced in the HB may not be completely contained and may continue in region of the magnet and beyond. This effect would cause a potentially large missing energy signal as well as an incorrectly reconstructed jet. The HO component of the HCAL has been installed in the exterior region of the magnet with a goal to mitigate this effect giving rise to the 11.8 interaction lengths in total.

The HB, HE, and HO are sampling calorimeters which employ a combination of steel and brass absorber material to induce hadronic and electromagnetic showers. The photons generated from these showers are sampled at several longitudinal depths by layers of plastic scintillator tiles. These tiles are embedded with wavelength shifting (WLS) fibers, which collect the scintillation light and send it to the clear fibers which direct this light to the dedicated optical decoder units (ODUs). The ODUs arrange the fibers into readout towers covering an area of 0.087×0.087 in $\eta - \phi$ plane and direct the light from each tower to channels of hybrid photo diodes (HPD) which have been designed to operate in a high magnetic field.

The HF sub-detector is a Cerenkov light detector made up of quartz fibers embedded within a 165 cm long steel absorber. There are two types of fibers within the HF: the long HF fibers which span the whole length of the HF and the short HF fibers which

begin at a distance of 22 cm inside of the detector. The difference between signals read out from the long and short fibers is used to distinguish between electrons and photons and hadrons. The **P**hoot **M**ultiplier **T**ubes (PMTs) are connected to the fibers via light guides and convert detected light to electrical signals.

Figure 2.4: A longitudinal schematic view of the CMS experiment and its hadronic calorimeter. The hadronic calorimeter consists of the barrel (HB), endcap (HE), forward (HF), and outer (HO) part, as designated in yellow colour on the figure.
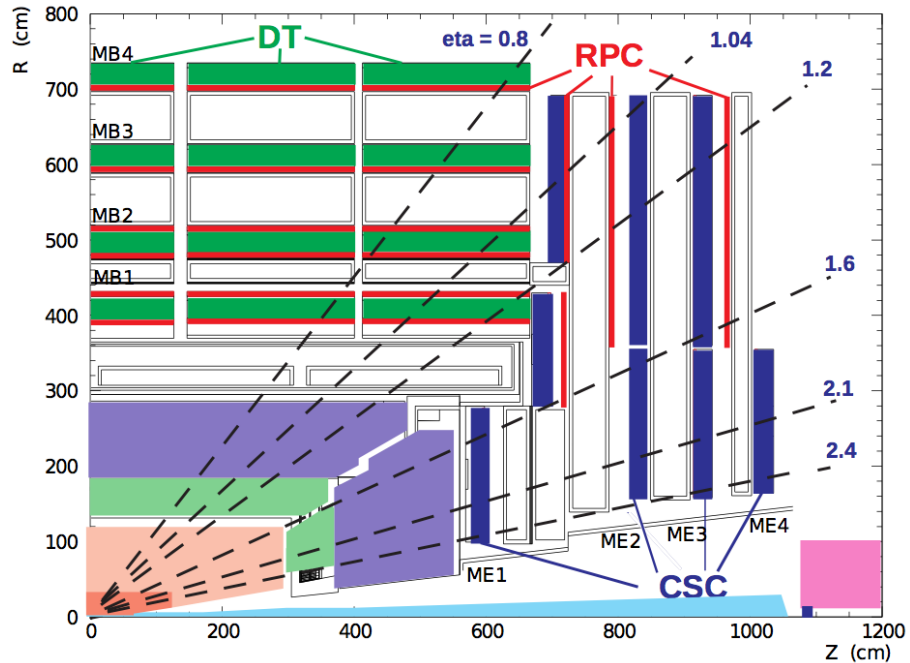
The energy is reconstructed from the digitized charge measurements. In HB, HE, and HO the four consecutive time samples are summed together. The signal in HF is very fast and has a width of about 10 ns which is mostly contained within one 25 ns sample. Individual channels are combined into a projective tower structure which combines information from ECAL and HCAL. More details on the design and implementation of the HCAL, as well as on the algorithms used to reconstruct the deposited energy can be found in [11] and corresponding references.

2.2.5 The muon system

The CMS muon system has been designed with a goal to provide robust muon identification and high precision momentum measurements over the entire kinematic range of muons expected from the LHC collisions. These design requirements have been in part motivated by the requirement to improve the potential for the discovery of the Higgs boson decay into four energetic mouns ($H \rightarrow ZZ \rightarrow \mu\mu\mu\mu$).

The CMS muon system consists of three types of gaseous tracking detectors (Figure 2.5). In the barrel region ($|\eta| < 1.2$) where the muon rate is expected to be low and where the returning magnetic field is weak, **D**rift **T**ube (DT) chambers are installed. The barrel DT chambers cover the pseudorapidity region $|\eta| < 1.2$. The drift tube system is organised in four stations which form concentric cylindrical shells around the magnet in the barrel. Each station consists of 8 layers of tubes measuring the position in the bending plane and 4 layers for the longitudinal plane. The stations are interspersed in between the various layers comprising the iron yoke which returns the magnetic field of the solenoid. These stations span the z-dimension in the form of 5 wheels, which are provided by the frame of the yoke.

Figure 2.5: A schematic longitudinal view of the CMS experiment and its muon tracking system. The muon tracking system consists of three types of gaseous tracking detectors: DT chambers, the CSCs and the RPC system. It spans the pseudo rapidity range $|\eta| < 2.4$.

In the endcaps region ($0.9 < |\eta| < 2.4$) where the muon rates and background levels are expected to be high and where the magnetic field is strong and non-uniform, the CSC are employed. The CSCs are modelled on the basis of the multi-wire proportional chamber technology. A CSC consists of 6 layers, each of which measures the muon position in 2 coordinates. Each endcap features 4 stations spanning the z-direction. Station 1 is composed of 3 rings of chambers stacked in the radial direction while stations 2, 3 and 4 contain two rings by design. The implementation of the station 4 in the ring 2 has not actually been completed as of 2011 and their installation is planned in the coming years.

The Resistive Plate Chambers (RPC) represent the third system. These are installed as a complementary triggering system with an excellent time resolution to reinforce the

measurement of the correct beam-crossing time at the highest LHC luminosities. The RPCs are located in both the barrel and endcap regions, and they cover a large portion of the rapidity range $|\eta| < 1.6$. The RPCs are parallel-plate double-gap gaseous chambers, operated in avalanche mode to ensure good operation at high rates.

The whole muon system covers the pseudorapidity interval $|\eta| < 2.4$ with no acceptance gaps ensuring a very good muon identification. In case of the magnetic field of 4 T, the offline reconstruction efficiency for the muons is expected to be in the range 96% - 99%. More details on the design of the CMS muon system can be found in [11].

2.3 The online event selection

The LHC has been designed to collide the bunches of protons at a rate as high as 40 MHz. The bunch-crossing separation of 25 ns offers the CMS detector an opportunity to read-out and record data. If all of the zero-suppressed data from the millions of electronic channels in the detector were to be read out for a single bunch-crossing which induces 20 collisions, it would yield in average about 1 Mbyte of data. By multiplying this figure by the bunch crossing frequency, one could easily conclude that it is not only impractical, but technologically prohibitive to stream and store such vast amounts of data at such high rates. Furthermore, the vast majority of these collisions will involve relatively soft physics processes, such as minimum-bias QCD events. On the other hand, the production of top-quarks will occur at a rate of the order of a few Hz. Similarly, the exotic and hypothetical physics processes could occur more rarely. For this reason, a dedicated online selection system, commonly named the trigger system, is required to filter the collision events as they occur before valuable resources are consumed. The trigger system plays its role at the beginning of every CMS event selection.

There are two stages of triggering and event rate reduction at CMS. The first stage is called the Level-1 Trigger (L1), which is composed of customized hardware and electronics designed for quick and efficient on-site processing of the digitized data that is reported from various sub-detectors. The second stage is called the High-Level Trigger (HLT), which consists of a farm of about a thousand commercial processors. The L1 is hardware-based, while the HLT is a software-based filtering system. The combined L1+HLT system is designed to reduce the event rate via the following sequence: LHC (40 MHz), L1 (100 kHz), HLT (300 Hz) and storage. Thus, the rate of data is ultimately reduced by roughly 5 orders of magnitude.

The L1 trigger system makes "accept-reject" decisions for each bunch-crossing based on a very crude information, for it has only 3.2 μs time to process and judge an event. The high-resolution version of the data is buffered in the onboard front-end electronics of the sub-detectors until the L1 accepts the event, at which point the finer data is transferred downstream to the HLT, where more sophisticated and refined event analysis can take place.

Three main tiers constitute the L1 trigger system: the local, the regional, and the global. The local tier builds so called trigger primitives, which can be understood as the

quanta of the entire trigger system. Trigger primitives are crude blocks of data, which reflect very basic quantities reported from the calorimeter systems and from the muon system. The regional tier of the L1 trigger system performs a synthesis of the information provided by the trigger primitives and ranks them according to some predetermined criteria. Ranking can be based on the quality of the measurement represented by the trigger primitive. Also, some trigger primitives can be judged to have more potential to reflect interesting physics than others. The global tier of the L1 receives the ranked information and executes quick algorithms to determine if the event should be accepted at this stage and propagated to the HLT. If the L1 accepts the event, then the higher resolution detector data is read out and sent to the HLT filter farm for a more thorough examination.

Aside from the content of the trigger primitive information, the global L1 decision can be contingent on the status of the sub-detectors and the Data Acquisition System (DAQ). The LHC will deliver about 128 bunch crossings in the 3.2 μs of time which takes the L1 to render its decision. This latency has a few consequences. In order to prevent buffer overflows, a few trigger rules are imposed. No more than $1 : 2 : 3 : 4$ events from the L1 trigger can be accepted per $75 : 625 : 2500 : 6000$ ns. This results in a small dead time (about 1%) where the LHC is delivering collisions, but the CMS detector cannot record the data. More details related to the L1 triggers for the tracking, calorimeter and muon systems can be found in [11].
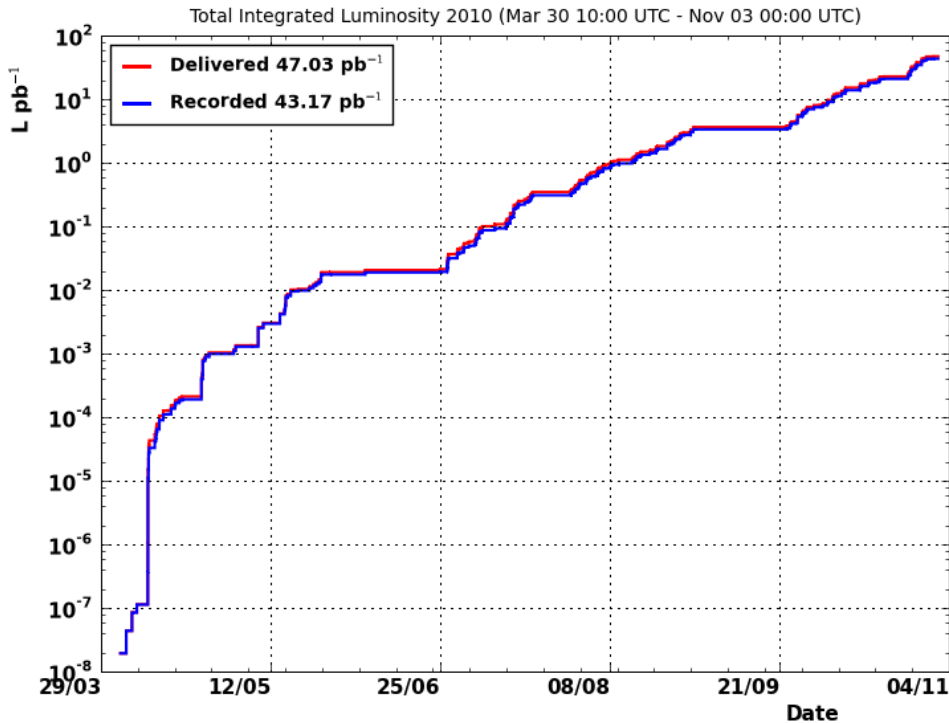
The HLT operates with a latency of up to 1 second and its purpose is to perform a more refined analysis of the L1-seeded objects. The L1 trigger will provide the HLT with muon, electron, photon, and jet candidates, as well as a few other coarsely calculated quantities (e.g., missing transverse energy). To assess the attributes of some of these objects, the data from the tracking system needs to be unpacked. It is a time consuming process to read out the data from the millions of channels in the Tracker, which is why the current CMS L1 trigger is blind to what occurs in the Tracker. Even with the extra time afforded to the HLT, only regional track reconstruction can be performed in the vicinity of the L1 objects. Aside from this exception, the full event reconstruction-level information is performed and is available to the filtering algorithms which run at the HLT.

The performance of the CMS trigger system is not solely evaluated by its rate reduction. Like any event selection filter, the trigger system will occasionally fail to accept events which it should accept. The frequency with which an event selection filter succeeds in accepting an event when it is supposed to is known as the signal trigger efficiency. Ideally, for a robust filter, the signal trigger efficiency should be about 100%. However, this is not true in general and depends on the definition of the signal.

At the HLT where the data is finer and the filtering algorithms can afford to be more complicated, there could be a large number of causes for events to be mistakenly rejected. For this reason, a significant amount of effort has been invested to understand, commission, and validate the trigger filters. This effort has been done both with the help of simulation and with the help of the analysis of real collision data.

2.4   Luminosity measurement and data collection

One of the very important aspects of the operation of CMS is also the precise determination of the luminosity delivered to the experiment by the LHC. This value enables an overall normalisation of the number of events studied in physics analyses and provides a key input to most of the physics analyses.

Figure 2.6: Integrated luminosity versus time delivered to (red), and recorded by (blue) the CMS experiment during the stable LHC beams.

The CMS performs the measurement of the delivered luminosity in two steps. In the first step the absolute luminosity scale is determined using the "beam separation scan method" pioneered by S. van der Meer at CERNs Intersecting Storage Rings in the 1960s and described in [22]. In this method, the size and shape of the beam interaction region is measured by recording the relative interaction rate as a function of the transverse beam separations. The absolute luminosity scale is then computed from the measured beam current and the measured transversal profile of the beams. This measurement is not performed for every run, but only when the LHC operation mode changes significantly.

In the second step, the relative luminosity is measured to determine the differences between the run periods with distinct beam conditions. In this step, the luminosity is measured by two online and two offline methods which exploit the physics properties of collision processes and the excellent performance of the HF calorimeter and the Tracking

system of the CMS. These four methods have shown to provide mutually consistent results and the total systematic uncertainty on the combined luminosity measurements was determined to be 4.0% in the year 2010. All of these four methods were used for the luminosity measurement in 2010 and are discussed in details in [23].

The luminosity recorded by the CMS during the year 2010 was not equal to the luminosity delivered by the LHC. The difference was a consequence of non-ideal operational procedures and synchronisation of the CMS experiment with the LHC operation. In addition, the CMS experiment is an aggregation of large number of complex sub-detectors and, hence, occasional non-ideal functioning of these can not be ruled out. The data taken during the periods when a part of the detector has not been operational at the satisfactory level, could have not been used in the physics analysis. Fortunately, the performance and the availability of the whole CMS experiment and its sub-systems were very good reaching about 84% during the year 2010.

The time profiles of the delivered and of the recorded integrated luminosity during the year 2010 are shown in Figure 2.6. The LHC has in total delivered $47 \, \mathrm{pb}^{-1}$ to the CMS experiment in 2010, while the overall data-taking efficiency of the CMS was 92% and it recorded $43 \, \mathrm{pb}^{-1}$ of this data to tape. The integrated luminosity that corresponds to the part of the full 2010 dataset that is available for physics analyses was:

$$\mathcal{L}_{int}^{(2010)} = \int_{2010} \mathcal{L}(t)dt = (35.9 \pm 1.4)pb^{-1}, \tag{2.1}$$

This is the dataset that has been used for the physics analysis and the search for physics beyond the SM presented in this thesis. We will see that the systematic uncertainty on the luminosity measurement of 4% will be the dominant systematic uncertainty in the analysis.

Until the end of November 2011 the LHC has in total delivered $5.73 \, \mathrm{fb}^{-1}$ of integrated luminosity to the CMS experiment. The overall data-taking efficiency of the experiment was again about 92% and it recorded $5.2 \, \mathrm{fb}^{-1}$ of the data to tape.

Chapter 3

The Electromagnetic calorimeter

> Necessity, who is the mother of invention.
> Plato[1]

3.1 Design of the calorimeter

The ECAL of the CMS experiment has been designed with the primary goal to provide identification and measurement of high energy photons and electrons produced in the LHC collisions [24]. The ECAL is positioned in the area just outside of the CMS Tracker and inside of HCAL and the superconducting CMS magnet. A part of the hadrons produced in the proton-proton collision deposits the energy inside of the ECAL before being absorbed in the HCAL. For this reason, the ECAL also participates in the measurement of the energy of jets of particles, which can have a significant fraction of pions decaying to photons and electrons depositing a part of the energy in the form of electromagnetic showers.
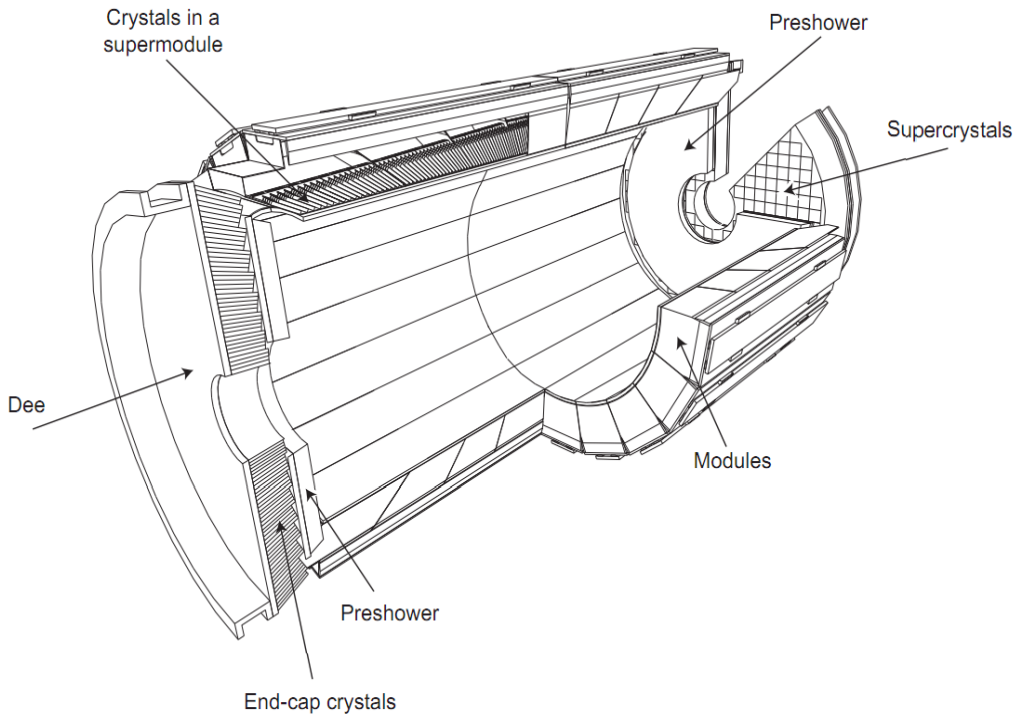
The design of the CMS ECAL detector has been dictated by the requirements on an excellent energy and angular resolution of the detector, which is necessary to be sensitive to the decay of a Higgs boson into two photons ($H \rightarrow \gamma\gamma$). In addition, the calorimeter had to be able to provide a fast response and to sustain the radiation doses expected during the operation of the LHC.

In order to provide the required performance, the CMS ECAL has been designed as a homogeneous crystal calorimeter composed of the barrel part and two endcap parts. The barrel part of the ECAL extends in the region $|\eta| < 1.479$ and comprises 36 Supermodules in total, each covering 20 degrees in ϕ. The Supermodules are arranged in two halves of barrel with 18 Supermodules each. Every Supermodule comprises of 1700 lead tungstate (PbWO$_4$) crystals. The crystal has a truncated pyramid shape with a front face of about 22×22 mm^2 and a length of 230 mm, which coressponds to about 25.8 radiation lengths. The lead tungstate crystals are characterised by a small Moliere radius of 2.19 cm, a short radiation length of 0.89 cm and a very fast response time [24]. The crystal axes

---

[1]Plato, The Republic.

are inclined at an angle of 3 degrees relative to the direction of the nominal interaction point, in both the azimuthal ϕ and η projections. Scintillation light from the crystals is detected by two avalanche photodiodes (APDs) of an active area of 5×5 mm^2 each. The APDs have been specially developed for CMS by Hamamatsu, providing a gain of 50 and approximately 4.5 photoelectrons per MeV at 18 °C. These are connected in parallel to the on-detector readout electronics which is organised in readout units that collect and process the signal in groups of 5×5 crystals.

Figure 3.1: Schematical representation of the design of the CMS ECAL [11].

Each endcap part of the CMS electromagnetic calorimeter, covering $1.479 < |\eta| < 3.0$, consists of 2 halves which are commonly named Dees due to their D shape. Crystals are grouped in 5×5 matrices to form supercrystals (SC). Each of the four Dees contain 128 standard SCs and 18 special partial SCs, containing in total 3662 crystals. The crystals are focussed at a point 1.3 m farther than the nominal interaction point along the beam line, with off-pointing angles between 2 and 8 degrees. In contrast to the barrel part of the ECAL, in the endcaps all crystals have the same geometrical shape. Due to the presence of the strong magnetic field and the high radiation dose, the endcaps require a special type of photodetector. For this reason, the scintillation light is detected by Vacuum Phototriodes (VPTs) with an active area of 280 mm^2, produced specially by NRIE for CMS. In addition, a Preshower detector (ES) is placed in front of each Dee and each of the two ESs disks comprise of 4 planes of silicon strip sensors.

The dependence of the energy resolution of a calorimeter on the energy E (in GeV)

of the incident particle, can be parametrized as:

$$\frac{\sigma_E}{E} = \frac{s}{\sqrt{E}} \times \frac{n}{E} \times c, \tag{3.1}$$

where s represents the stochastic term, n represents the noise term and c represents the constant term.

The stochastic term originates from the Poisson fluctuation of the generated charge in the electromagnetic shower, as well as the shower lateral containment in the cluster matrix. The charge multiplication inside the photodetectors together with the quantum efficiency and fluctuation in the light collection efficiency of the APDs and VPTs are contributing factors to the stochastic term and it is the dominant term for low energy measurements.

The noise term reflects the dependence on the electronics noise and has a constant value not related to the energy of the incident particle. In the ECAL test beams the noise term was determined during the dedicated runs where no real beam was present. The noise term in the LHC conditions will also include the noise from pile-up events.

The constant term depends on non-uniformity of the longitudinal light collection, leakage of energy from the rear face of the crystal and the accuracy of the detector inter-calibration constants. Other important factors are the thermal stability and the high voltage stability, which both affect the APDs gain. A temperature stability of the level of $0.05\,\text{C}°$ and a high voltage stability of the level of $30\,\text{mV}$ and crucial in order to reduce the contribution to the constant term to the level of 0.1% or less. The target value for the constant term, which dominates the resolution at high energies, is 0.5% for both the barrel and the endcaps.

More details about the ECAL detector performance and especially the stabilization and control of the electronic noise, high voltage, temperature and the crystal transparency monitoring system will be presented in the following section. We will show that the operating conditions of the ECAL were in line with the requirements and that the observed transparency, high voltage and temperature fluctuations are controlled well, thus providing a negligible contribution to the constant term of the energy resolution. A particular focus will be put on the temperature stability and the safe operation of the ECAL.
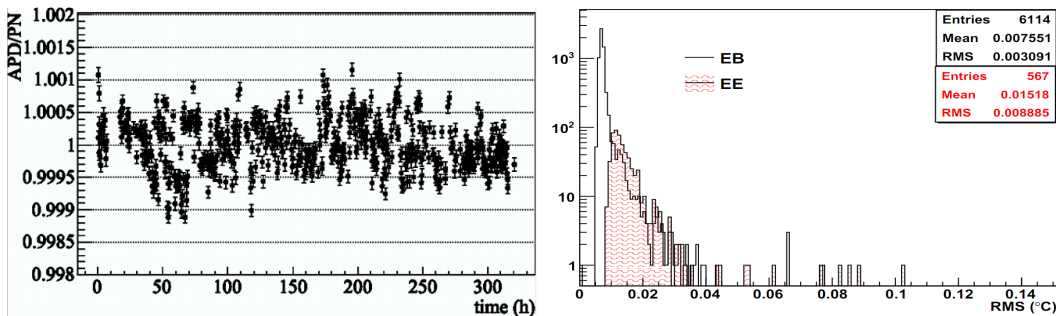
3.2 Control and stability of calorimeter parameters

The previous section describes how the physical requirements for high performance of the ECAL have dictated the choice of active and passive components used in the realization of this complex sub-detector. The same section describes the challenges that need to be overcome in order to provide the required performance of the calorimeter resolution. This section reviews the stability of the parameters that can influence the resolution of the ECAL and introduces the motivation for the implementation of dedicated control and safety system of the detector. It primarily refers to the system for crystal transparency control, the system for the control of high and low voltages necessary for the operation

of ECAL photo-diodes and readout electronics, as well as the system necessary to control the temperature stability of ECAL crystals and photodiodes. The following section will focus on the design and implementation of the detector control and safety systems.

3.2.1 Control of the crystal transmission

The performance of the ECAL lead tungstate crystals will be affected by the high levels of ionising radiation and flux of hadrons. The degradation of their performance is expected to be reflected only in the change of the transparency through the mechanism of creation of radiation-induced absorption centres in the crystal [25, 26]. Consequently, an "in situ" calibration of the response of crystals is essential for maintaining the desired resolution of the calorimeter during the operational lifetime for many years. For this reason, it was necessary to design and implement a dedicated transparency monitoring system which could control and correct the response of the crystals.

Figure 3.2: The measured stability of the crystal response when illuminated by the blue laser over a period of two weeks. The response is characterised by the ratio of signals from the APD and the PN diode (left). The temperature stability, represented by the rms of the measurements of dedicated thermistors over a period of two months (right). The measurements presented in these figures have been collected during the ECAL operation in the year 2010 [27].

The system for the monitoring of the crystal transparency is based on the injection of short pulses of laser light of appropriate wavelength in each crystal of the ECAL via dedicated optical fibers [28]. Comparing the response of APDs to the pulses of light measured by a reference PN diode, the changes to the transmission response can be corrected "in-situ" for each of the crystals. The main features of the system are:

- two sources of laser light, where the wavelength of one source (440 nm) is near the maximum emission spectrum of the crystal and the wavelength of the other one (495 nm) is present for an extra cross check of the complete readout chain;

- a pulse energy of 1 mJ, which corresponds to the energy of approximately 1.3 TeV in the ECAL readout system and has uncertainty on the intensity of less than 10%;
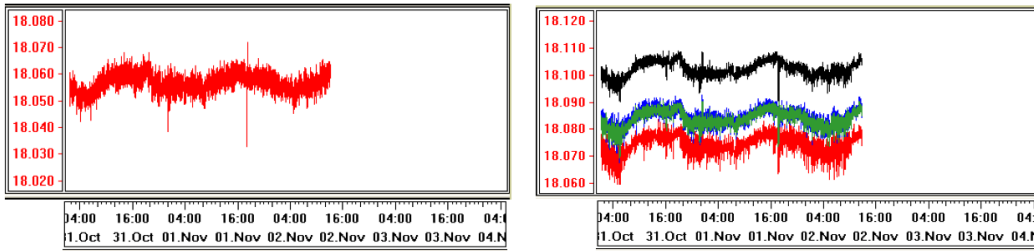
- a width of the signal pulse of 40 ns with the maximum frequency of about 80 Hz.

A large number of tests have been conducted in order to characterise the performance of the system and the tests have shown that the system can provide a successful control of systematic uncertainties in the calorimeter resolution [29]. Given the importance of this system for a proper operation of the ECAL, it was clear that a precise control of the operation of this system is necessary.

Although the high rate of radiation induced damage is expected from LHC operation in late 2011 and beyond, it was important that the light monitoring system itself is extremely stable, to better than 0.2%, already during the operation in the year 2010. Figure 3.2 (left) shows the measured ratio over time of the APD signal with respect to the reference value from a PN diode, when illuminated by the blue laser light of the monitoring system. The observed variation of less than 0.03% ensures that the stability of the system is much better than that needed to achieve a constant term in the ECAL energy resolution of 0.5%. More details on these tests can be found in [27].

3.2.2 Stabilization of the bias voltage and crystal temperature

The temperature-dependence of the amplification factor of the APDs and temperature-dependence of the number of scintillation photons generated in the crystals, implies the necessity for stabilisation of the temperature of the entire mass of crystals and APD diodes to better than 0.05 C°. Given that the power dissipation of the CMS Tracker readout electronics in front of the ECAL crystals is enormous (the total power of heat dissipation amounts to about 200kW [28]), the fulfilment of this requirement posed a technological challenge.
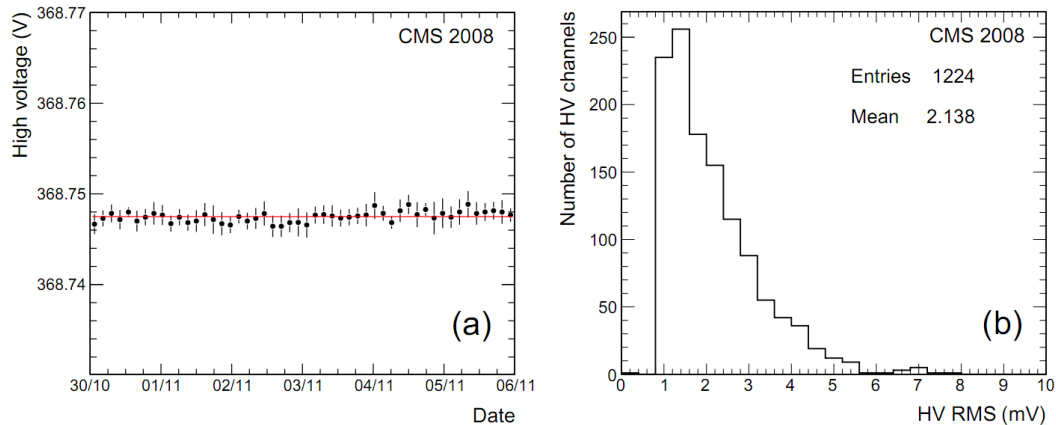
Figure 3.3: Temperature stability of the incoming water of the cooling system and crystal temperature shield for four modules of one ECAL super-module [private communication with S.Zelepoukine, 2006].

After a thorough analysis of many different solutions for the cooling system and the temperature stabilization, the CMS ECAL Collaboration has opted for a water cooling system (ECAL Cooling System), with the following features [28]:

- the system needs to provide a water flow greater than 70 liters per second in order to ensure an effective removal of thermal energy dissipated in the vicinity of ECAL crystals and APD diodes;

- the temperature of cooling water needs to be precisely regulated at 18.00 ± 0.01 C°, necessary for a proper stabilisation of the temperature of crystal and APD diodes;

- each ECAL Supermodule needs to be supplied with an independent water cooling;

- the system should provide a thermal shield between the Tracker detector and the ECAL crystals, as well as a thermal shield between the ECAL crystals and the ECAL readout electronics.

- the system should provide additional cooling for the ECAL readout electronics.

The ECAL Cooling system was designed according to these specifications and each Supermodule and each end-cap are independently supplied with water as a coolant at 18.00 ± 0.01 C°. The water runs through a thermal screen placed in front of the crystals which thermally decouples them from the silicon tracker, and through pipes embedded in the aluminium grid in front of the electronics compartments. Regulation of the water temperature and the water flow, as well as the opening of valves is performed by a dedicated Siemens PLC system. This system is connected to a PC via a Siemens S7 connection and monitored by the dedicated control system which will be described in the following section.

Figure 3.4: Stability of the output voltage for channels of the CAEN HV system during the CRAFT period. It was monitored during one week of data taking. Each data point has been averaged over a three hour time period (left). Distribution of the RMS of the readings for each HV channel during this period (right).

During the various ECAL test campaigns in the period from 2003 until 2007, several prototypes of the Cooling System were analysed. The results of these tests [30] confirmed that the latest prototype of the system met all necessary criteria and the final implementation was based on it. Figure 3.3 shows the temperature stability of the incoming water of the Cooling System and crystal temperature shield for all four modules of the tested Supermodule during a period of 3 days. Figure 3.2 (right) illustrates the temperature stability over a period of two months during the ECAL operation in the year 2010 and illustrates the system performance.

The APDs require also a power supply system with a stability of the bias voltage of the order of a few tens of mV. For this reason, a custom HV power supply system has been designed for the CMS ECAL in collaboration with the CAEN Company. The system is based on a standard control crate SY1527 hosting eight A1520PE boards specially designed for this application. Up to nine channels can be hosted on a single A1520PE board and each channel can give a bias voltage of up to 500 V with a maximum current of 15 mA. The operating APD gain of 50 requires a voltage between 340 and 430 V. In total, there are 18 crates and 144 boards. Every SY1527 crate communicates with a board controller via an internal bus and has to be operated by the dedicated control system via an Object linking and embedding for Process Control (OPC) server.

The ECAL digitalisation electronics located on the very front-end electronics cards also require a very stable low voltage in order to maintain a constant signal amplification. The system uses low voltage regulators that guarantee this stability. The power is supplied by a dedicated LV system that is based on multichannel MARATON Power Supplies (PS) from Wiener. In total there are 108 PSs for the ECAL barrel and 28 PSs for the ECAL end-cap. All of the LV PSs are water-cooled and have to be operated by the dedicated control system via CAN-bus.

The HV system was tested during several beam-tests in the period from 2002 until 2007. The final tests have been conducted during the CRAFT data taking period in 2007. The stability of the barrel HV channels during this period have been estimated by the distribution of the RMS of the readings of each individual channel. The average fluctuation of the high voltage was 2.1 mV, while more than 97% of the total number of channels have shown fluctuations below 5 mV. This was fully consistent with the initial specifications. The Figure 3.4 shows the high voltage stability of the channels of the CAEN HV systems during these tests.
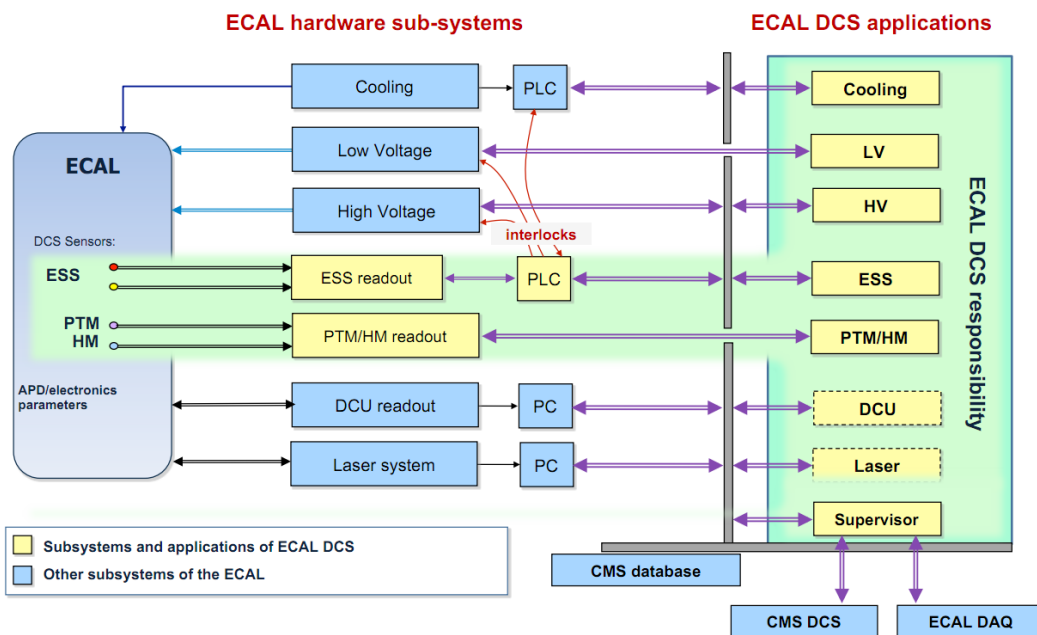
3.3 Design of the detector control system

The ECAL Detector Control System (ECAL DCS) was designed with a goal to provide an autonomous control and monitoring of working conditions of the ECAL detector, monitoring of the parameters of the ECAL readout electronics, as well as control of the correct functioning of all ECAL subsystems. Following the requirements discussed in the previous section, the control system of the ECAL has been implemented to provide and ensure the following functionality:

- an autonomous and accurate monitoring of the crystal and APD diode temperatures (18.00 ± 0.01 C°) and humidity levels inside of each ECAL Supermodule;

- an autonomous and sufficiently precise monitoring of the air temperatures inside the ECAL Supermodules, the proper operation of the Cooling System, and the presence of any water leakage inside Supermodules. It also had to ensure an autonomous shutdown of the ECAL subsystems operation in potentially unsafe conditions;

- sufficiently precise monitoring of ECAL readout electronics operating parameters

(operating temperature, intensity of the corresponding currents and voltages) based on data obtained through the ECAL system for data aquisition (ECAL DAQ);

- a software control and monitoring of the procedure of parameterization, start-up and operation of ECAL systems for high and low voltages, the ECAL cooling system, as well as the ECAL laser monitoring system;

- a possibility for an early detection of abnormal conditions, distribution of warnings and alarms, execution of predefined control actions, as well as distribution of corresponding interlock signal in order to ensure safe operation of the detector;

- connection with the general CMS detector control system (CMS DCS), with the general system for the safe operation of the entire CMS experiment (CMS DSS) and with the system that operates the CMS experiment (CMS Run Control).

Figure 3.5: A functional block diagram of the ECAL DCS system with its interconnections to the various subsystems of the ECAL detector.

The final design of the ECAL DCS and the interconnections between all the relevant ECAL subsystems are presented in a block diagram shown in Figure 3.5. The figure shows the internal structure of the ECAL DCS and its main components, but also illustrates the overall complexity of the ECAL DCS system. The components of the ECAL DCS can be divided in three separate functional groups:

- ECAL DCS software components for a direct control of subsystems that provide necessary services to the ECAL;

- The PTM / HM system for accurate monitoring of the temperature of the crystals

and APD diodes, as well as monitoring of the humidity levels inside the ECAL Supermodules;

- The ESS with a role to ensure a safe operation of the detector and all its subsystems.

The first group represents the hardware subsystems that provide necessary services to the ECAL. The ECAL DCS team has direct responsibility for the implementation of the software control of these systems, while it is not responsible for the hardware implementation of these subsystems. The other two groups represent the hardware systems which are an integral part of the ECAL DCS. For this reason, the ECAL DCS had full responsibility on the development and implementation of both hardware and software applications for these systems. Those subsystems outside of the ECAL DCS responsibility are shown in Figure 3.5 in blue, while the ECAL DCS systems are shown in yellow.

In the following section we will give a brief overview of the implementation and performance of the PTM / HM and ESS system. The details on the implementation of individual software components of the ECAL DSC system are beyond the scope of this thesis and will be only briefly described.

3.3.1 Precision temperature and humidity monitoring

The PTM / HM system consists of two independent systems: the PTM and the HM system. The purpose of the PTM system is to provide precision temperature measurements and to monitor the stability of the temperature distribution in the environment of the ECAL crystals and photo-detectors. In addition, it provides archiving of the temperature distribution history for use in the ECAL data processing.

Figure 3.6: Photographs of ELMB and custom made PTM/HM electronic boards [31].

In order to provide this functionality, 360 high quality NTC thermistors [32] with very good long-term stability have been installed in the ECAL Supermodules and 80 have been installed in the ECAL Endcap Dees. Sensors are individually pre-calibrated by the manufacturer and then tested and sorted in the lab to ensure a relative precision better than 0.01 degrees.

The purpose of the HM system is to monitor the relative humidity (RH) of the air inside the ECAL electronics compartments and to provide early warnings about high
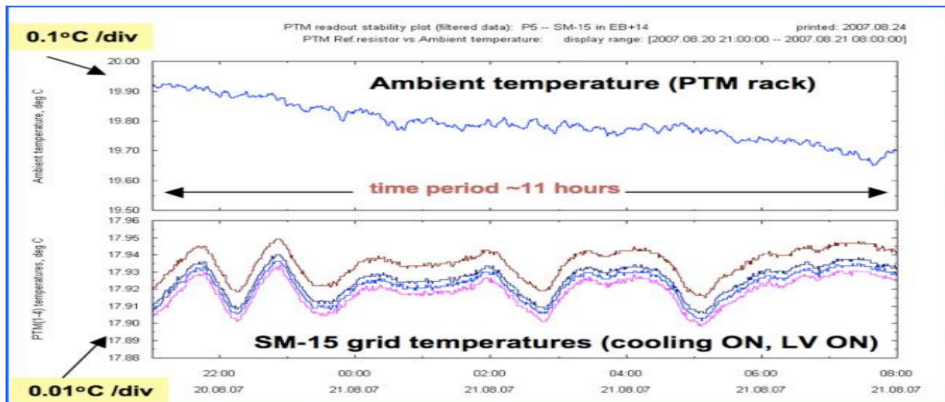
humidity conditions that may potentially lead to water condensation inside the detector. There are 176 HM sensors with 5-7% RH precision placed inside the ECAL.

Both PTM and HM sensor samples were tested for their capability to work in an environment with high radiation levels and the strong magnetic field that will be present in the ECAL region of CMS. Sensors have shown the ability to maintain their operational parameters unchanged during the expected running life time of the ECAL.

The readout systems of both PTM and HM systems are based on Embedded Local Monitor Board (ELMB) modules designed by the ATLAS experiment [33]. The ELMB module is a compact plug-on card with one embedded high-precision 16-bit ADC, one 64 channel differential analogue input multiplexer, one ATMEL AVR RISC microprocessor and one CAN bus interface (Figure 3.6, left). Each ELMB module is plugged on a specific PTM/HM electronic board that provides signal mapping/routing for 64 channels (Figure 3.6, right). In addition, PTM is using a specifically designed circuit board for thermistor excitation, while HM is using transmitters from the sensor manufacturer to excite the RH sensors and provide the conditioning of their signals.

The PTM/HM readout electronics has been implemented on 6U-size boards that have been installed in PTM/HM standard 6U Euro-crates. The complete configuration comprises four crates installed in two standard LHC racks. This configuration provides a readout system for 512 channels of the PTM and 192 channels of the HM system.

Figure 3.7: Performance of the PTM readout system (for the ECAL SM-15) [31].

All PTM/HM readout electronics is located on the balcony in the CMS experimental cavern (UXC), outside the CMS detector. The readout electronics has been successfully tested for the long-term operation in this environment [31]. The position of the PTM/HM outside CMS offers an additional advantage allowing easy access to the readout system for its maintenance and module replacement during CMS shut-down periods.

After the raw sensor signals are digitized with the ADC of the ELMB, the data are sent by the ELMB microcontroller via a CAN bus to the DCS PC hosting the PTM/HM application, which is located in the CMS service cavern (USC). All ELMBs located within the crates inside one rack are connected to a single CAN bus.

The performance of the PTM readout system in terms of resolution and noise levels

has proven to be outstanding. Temperature fluctuations from the noise introduced in the system are of the order of 0.001 C° in the range of 18 - 22 C°. An example of the performance of the PTM readout system, as well as of the stability of the cooling system connected to the SM-15 inside CMS at P5 is presented in Figure 3.7.

The implementation of the HM readout system is identical to the method of implementation of the PTM readout system, with a difference that the HM uses humidity sensors UPS600 produced by Ohmic Instruments Company. Both systems have been implemented at CERN laboratories in collaboration between researchers from IHEP Protvino and researchers from the Institute for Particle Physics of ETH Zürich.

3.3.2 The ECAL safety system

The systems for control and stabilization of operation of parameters of the ECAL represent extremely important subsystems of this detector. The proper functioning of these systems and proper procedures of their operation are vital for safe operation of crucial components of the ECAL: the lead-tungstate crystals, the APD detectors and the ECAL readout electronics. In order to provide this functionality, the CMS ECAL Collaboration has decided to implement the ECAL Safety System.

The ESS was designed as a dedicated and completely autonomous system. The responsibility of the system is to safeguard the proper functioning of all the ECAL subsystems thus representing the heart of the ECAL DCS. Complete development of the ESS system, as well as testing and implementation of its hardware and software components, have been performed in close collaboration between the CMS Belgrade group of Institute of Nuclear Sciences "Vinca" in Belgrade and the Institute for Particle Physics of ETH Zürich. The prototype evaluation campaigns have been performed both in the test areas at CERN and at PSI. The design, evaluation, testing and implementation of the ESS represent an important work and contribution to this thesis and will be presented in details in chapter 4.

3.3.3 Software implementation

In accordance with an official recommendation of the appropriate CERN LHC groups, all ECAL DCS applications have been developed using the commercial supervisory control and data acquisition software WinCC Open Architecture (WinCC OA) [34], formerly Prozess Visualisierungs und Steuerungs System (PVSS), and standard Joint Controls Project (JCOP) Framework components [35]. The CERN developed JCOP Framework provides extensions to WinCC OA for the high energy physics domain and was used to facilitate the development process.

The heart of each control system at the LHC is a Finite State Machine (FSM) implemented with SMI++ [36], a derivative of the former DELPHI controls software. The FSM enables a high level of abstraction and simplified representation of detector control systems by introducing a finite set of well defined states, in which each of its subsystems can be, and rules that govern transitions between these states. The FSM states of

each subsystem depend on the current status of the underlying hardware. At the same time, the FSM enables logical grouping of DCS subsystems into a hierarchical tree-like structure, where "parent" states are uniquely determined by states of its "children" and system-specific logic. Each "parent" in such a FSM tree can issue an action command to its "children". Action commands at the lowest level imply appropriate commands from the control software to the hardware that is being controlled.

The CMS ECAL controls software has also been implemented in this way. The software granularity is driven by the ECAL subsystem structure. The HV, LV, Cooling, PTM/HM and ESS are controlled by independent applications. On top of these applications, there is the ECAL Supervisory application that implements FSM hierarchical structuring of the whole ECAL controls software. One of the advantages of this implementation is the minimization of human failures, as well as better overview for operators and for subsystem experts of the status of their subsystems. The ECAL Supervisory application provides a software layer with automatic control actions in case of potentially unsafe ECAL operation. In the majority of the situations when some harmful conditions were detected, the protective mechanisms implemented in this layer took care of switching the detector off prior to the actions of the ESS. In all the cases, the systems reacted properly, moving the ECAL to a safe state and preventing it to be switched on without an expert intervention.

In addition, the ECAL DCS applications include numerous other features. These include: full parameterization and visualization of each subsystem, archiving of all relevant data to the CMS Conditions database, as well as loading from and storing to the CMS Configuration database the start-up and operational parameters for all DCS subsystems. The ECAL DCS group has also developed a tool for an automatic installation and configuration of its software components. The tool makes it easy to maintain the cluster of ECAL DCS computers and minimizes the downtime of CMS after serious data loses on these PCs. The information needed to restore each system is provided by datasets inside the CMS Configuration DB. More details on the software implementation of the ECAL DCS and its performance during the CMS operation in years 2010 and 2011 can be found in [37].

Chapter 4

Implementation of the ESS

4.1 Design of the system

In chapter 3 we have discussed that the ECAL Safety System has been designed with the main task to secure the proper functioning of all the relevant ECAL subsystems. The criteria for the design of the system, set by the CMS ECAL collaboration [28] were rigorous in terms of the required system performance and its overall reliability. In particular, the system had to provide the following functionality:
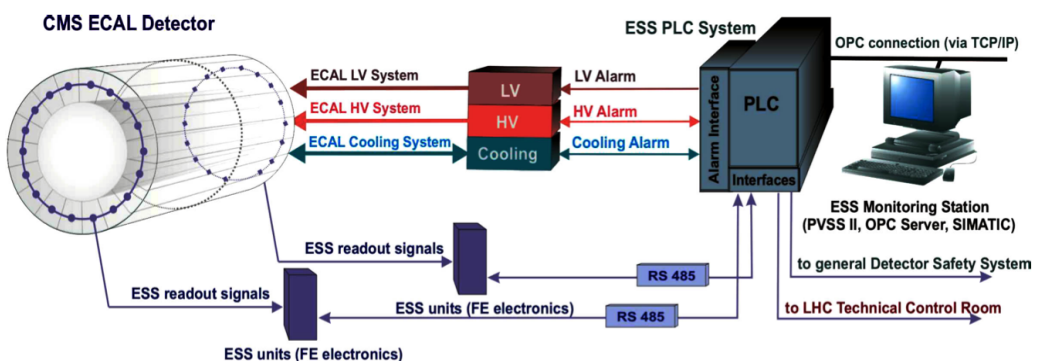
- a full autonomy in every aspect of its operation;

- an independent, continuous and reliable readout of the temperature of the environment of the front-end electronics of the ECAL readout system. The initially specified accuracy of the ESS system for sensing temperature was about $0.1\,^{\circ}$C;

- an independent, continuous and reliable readout of the signals from the sensors for the detection of the presence of water (WLD sensor) inside of the ECAL;

- continuous archiving of sensor data and storage of an appropriate information about the ECAL sub-systems in an efficient and reliable way in the CMS Conditions database. This feature would allow for the analysis of the system status and performance of the complete ECAL;

- reliable hardware interconnections with the ECAL Cooling System for the hardwired exchange of critical system information (temperature and flow of the cooling water, the proper functioning of hardware and the ECAL Cooling PLC system etc.).

- reliable hardware interconnections with the CMS DSS for sending the hardwired alerts on the proper functioning of the ESS, and for accepting general hardwired alerts in critical or unsafe situations;

- reliable hardware interconnections for interlocking of the ECAL HV and LV systems;

- a fast and reliable response in case of abnormal conditions or an external alarm by the DSS or ECAL Cooling System. The abnormal conditions include critical changes in temperature or the presence of water in the ECAL. The required ESS reaction in a critical situation involves generation of appropriate hardware and software signals in a defined time sequence, as well as the remote alerts to the operators and experts (via the GSM network);

- radiation tolerance in accordance with official specifications of radiation doses and hadron fluences expected in the CMS experiment during the lifetime of LHC [28, 11];

- maximally achievable level of reliability of system components with low level needs for service and maintenance of its equipment.

4.1.1 The three layers

In order to realize the system that fully meets all the specified criteria, the ESS has been implemented in a way which could be easily understood if we decompose the system into three independent, mutually interconnected, logical layers (Figure 4.1):

- a layer which performs the multiplexing, correction and analog-to-digital conversion of signals from the ESS sensors. This is the Front-End (FE) layer of the ESS;

- a layer whose function is to download and process the data from the FE layer of the ESS and other relevant ECAL sub-systems, and to generate necessary control signals and hardwired interlocks. This is the PLC layer of the ESS;

- a layer of software to monitor and control the entire system, as well as to perform certain predefined automatic actions. This is the Software layer of the ESS.

Figure 4.1: A functional diagram of system layers and their interconnections with other systems and services.

Implementation of the first layer of the system included the selection and calibration of appropriate temperature sensors and WLD sensors, the choice of the possible methods for signal multiplexing and control of various systematic effects, as well as the choice of

systems for the readout of sensor data and its transmission to a higher layer of the ESS. This first layer has been implemented using NTC thermistors of 470 Ohms as temperature sensors [38], radiation tolerant Maxim 4582 multiplexers for channel selection and the Resistive Bridge Front End (RBFE) discrete-component electronics for signal amplification and eventual correction of systematic effects. The Microchip PIC18F452 microcontroller with ADC converter has been chosen to process the sensor data, control the electronics and to serially send the data to a higher layer of the ESS. All these functionalities have been implemented within the dedicated ESS Readout Units (RU).

Implementation of the second layer included the choice of a reliable system that allows autonomous data collection and processing of signals from the lower ESS layer, autonomous generation of hardwired interlock signals, as well as the implementation of redundant logic in the system. This layer of the ESS has been implemented using specially designed ESS Interlock Units (IU) and a redundant pair of industrial programmable logic controllers, Siemens PLC S7-400H and S7-300 [39]. The PLC system has been chosen for serial communication with the lower layer of the ESS, as well as for the processing of the collected information. Communication with the Software layer of the ESS has been implemented via the direct S7 connection with the dedicated PLC S7-431 module for IP communications over the Ethernet.

The highest layer of the system has been implemented as a complete software layer and its main role is to provide the visualization, control and archiving of the status of crucial ECAL subsystems. In accordance with the recommendation of the appropriate official LHC Group, the ESS layer has been developed as a Finite State machine and as part of the entire ECAL DCS system using a commercial SCADA environment PVSS and the LHC JCOP Framework of standard components. In the following sections we will present in details the implementation of each of these layers of the ESS.

4.2 The readout system
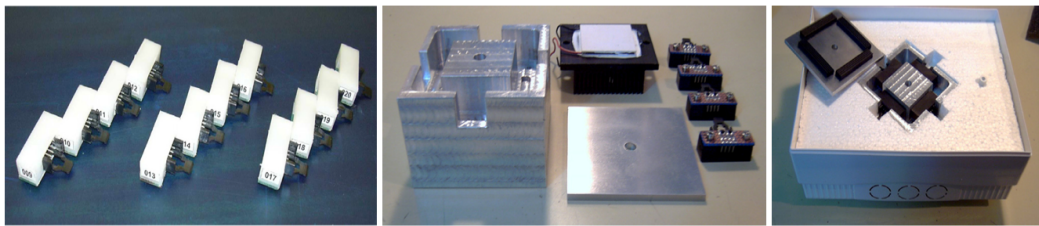
4.2.1 Temperature sensors and calibration

The ESS for measurement of the temperature of front-end electronics in ECAL Supermodules is based on the NTC thermistors produced in SMD technology by the company EPCOS [38]. Given the fact that each ECAL Supermodule is physically divided into four modules, it was decided to have one measuring point in the center of each module. In order to achieve greater reliability and easier identification of faulty sensors during the operation of the ESS, it was decided to provide redundancy by adding an additional NTC temperature sensor at each measurement point.

Due to restrictions imposed by the front-end electronics of the ESS readout system (amplification gain, saturation limit, the input resistance and capacitance) and by the internal characteristics of the selected PIC microcontroller (input range, resolution of the ADC conversion), it was shown that the best performance can be achieved by measuring the temperature of the system using NTC thermistors with characteristic resistance of 470 Ohms. It has also been shown that the selection of these temperature sensors allows

to easily achieve the required temperature resolution in the temperature range from 10 to 50 °C [40].

Each measurement location has been equipped with two NTC thermistors closely soldered to a specially reinforced plate made of radiation-resistant material, equipped with 4-pin connectors for easy installation of these sensor pairs inside the ECAL module (Figure 4.2). The sensor pairs at the measuring positions of all four modules of an ECAL Supermodule are connected to the ESS via specially produced cables and the ESS connector (D-SUB25) at the patch panel of the Supermodule. The ESS cables are made from radiation-resistant and heat-resistant materials and contain four groups of two pairs of crossed wires (2 STP) with appropriate shielding to reduce the electromagnetic interference. The patch panel of each Supermodule is connected to the ESS FE electronics located outside of the CMS detector, via specially produced cable with 9 STP. The position of the ESS FE electronics in the CMS cavern is such that the length of these cables ranges from 40 m to 100 m. All of the ESS cables have been manufactured according to strict specifications by the team responsible for the integration of these components in CMS.

Figure 4.2: The ESS sensor pairs ready for installation in ECAL Supermodules (left), a custom made system for automatic calibration of ESS sensor pairs (middle, right).
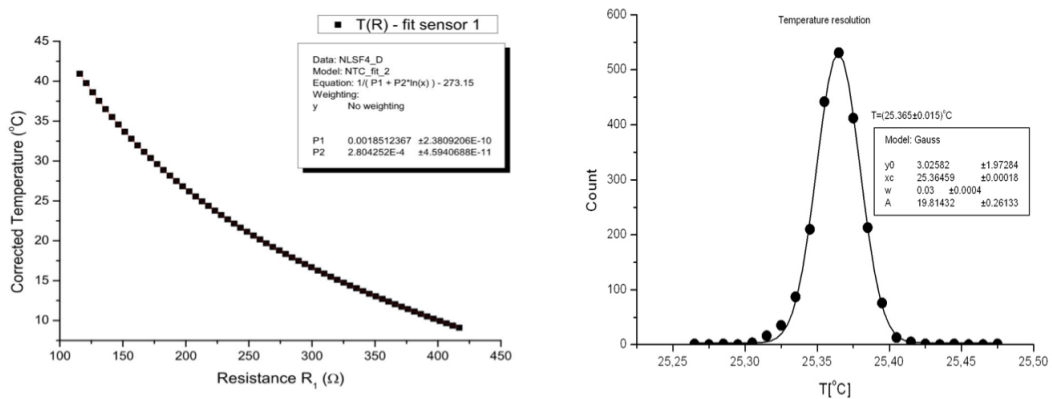
Calibration of the ESS temperature sensors was performed using an automatic calibration system created especially for this purpose. The automatic calibration system consisted of a thermal "bath" with a high thermal capacity, an insulation layer for thermal separation from the external environment, digitally controlled thermoelectric devices that operate on the principle of Peltier's effect, and a pre-calibrated laboratory thermometer as a primary reference scale (Figure 4.2). The calibration of sensors has been performed by fitting the results of measurements of sensor resistance to a nonlinear fitting function for the NTC sensors [38]:

$$T[^{\circ}C] = [a + b\ln(R[\text{Ohms}] - R_{\text{cable}})] - 273.15^{\circ}K \qquad (4.1)$$

where R_{cable} was the measured resistance of the cables between the patch panel of a Supermodule and the ESS FE electronics. The calibration procedure was conducted in the absence of these cables so that the cable resistance was $R_{\text{cable}} = 0$.

The measured R_{cable} values can vary in the range from about 4 Ohms to about 50 Ohms, depending on the exact location of a Supermodule in the final position of ECAL in CMS.

Given that this value is approximately 10 % of the nominal resistance of the NTC thermistor, it was clear that this correction had to be taken into account in order to perform a calibration of the system with sufficiently high precision. For this reason, the ESS connector on the patch panel of each Supermodule has been equipped with a pair of corresponding short-circuited pins whose sole purpose is to accurately measure the R_{cable} value in the final Supermodule positions.

Figure 4.3: The result of the calibration of a ESS sensor pair.
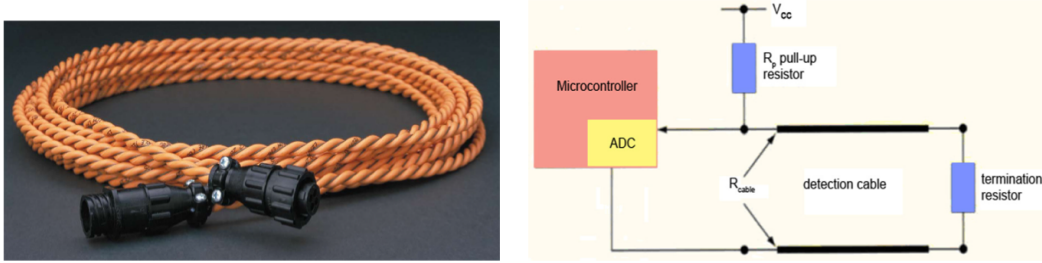
The calibration procedure, based on the known functional dependence of temperature, was adjusted to enable automatic calibration of temperature sensors with an uncertainty of about $\pm 0.02\,^{\circ}$C. Figure 4.3 illustrates the results of the calibration of temperature sensors by the method described above.

4.2.2 The leakage detection system

The stabilization of the temperature of the ECAL thermal shield and front-end electronics has been performed by implementing the ECAL water cooling system. For this reason, the system for detecting the presence of water due to possible leaks from the cooling system had to be implemented within the ESS. This subsystem of the ESS is based on a commercially available cable-sensor for detection of water and conductive fluid (WLD sensor), produced by the RLE Technologies company [41]. The sensor-cable is composed of two copper conductors with standard non-conductive insulation and two wires with sensitive polymer coating (Figure 4.4). These conductors have been physically-separated from the metallic walls of a Supermodule by non-conductive trays along the entire length of the sensor cable.

The principle of detecting the presence of water or conductive fluid with this the sensor is simple. At one end of the sensor-cable the conductors with a sensitive polymer layer are electrically connected with the appropriate terminator resistance (Figure 4.4). At a time when the sensor-cable comes into contact with a conductive fluid, or when a fluid makes contact between the two sensitive polymer conductors on the cable, there will be

a considerable drop of the resistance that is measured between the free ends of the two conductors. Therefore, the detection of the presence of conductive fluid in the system is based on the detection of the change of the sensor resistance. The principal scheme of a circuit for detecting the presence of water with the described WLD cable is shown in Figure 4.4, right. In the case of ESS WLD cables, the value for the terminator of 87 kOhm has been selected.

Figure 4.4: The WLD sensor ready for assembly (left) and a functional scheme of the sensor readout method (right).

A thorough testing of the WLD system based on the scheme depicted in Figure 4.4 showed that the sensitivity and stability of the sensor response decreases after long periods of sensor exposure to the DC. On the other hand, it was necessary to design a system that will be able to maintain its performance for long periods of operation. For this reason, the final solution for the ESS WLD readout system has been implemented with a PIC microcontroller which provided the bias voltage to the WLD sensor with periodic changes in its polarity with a frequency of 10 ms. The dedicated testing has shown that this type of readout has eliminated all the possible effects of sensor performance degradation that could occur as a result of long-term polarization of its polymer material.

### 4.2.3   The front-end electronics

The electronics of the Front-End (FE) layer of the ESS is based on radiation-resistant, bi-directional analog Maxim 4582 multiplexer [42] and radiation-resistant RBFE electronics specially implemented with discrete components. The basic characteristics of the Maxim 4582 multiplexers are contact resistances of only 150 Ohms and a very low leakage current in the OFF state of about 1 nA at 25 °C, which are very important features in low resistance measurement applications.
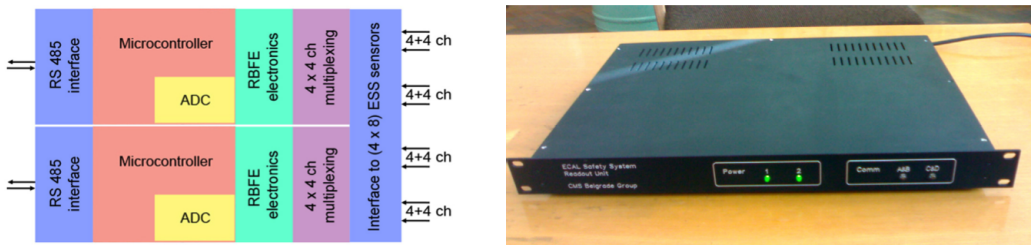
The RBFE component of the FE electronics has been implemented in a discrete technology and includes: bi-directional programmable current source with intensity of 50 μA, differential amplifier with gain 50 (input range from -50 to +50 mV, the output range 0 - 5V) and analog switches for selection of one of 8 different modes of measurement. The implementation of the digital RBFE has allowed for the selection of the particular measurement mode by selection of the polarity of the bidirectional power source, the polarity of the differential amplifier, as well as selection of the reference resistor or the NTC

thermistor. The readout of each sensor consists of the measurement results in these 8 measurement modes (ADC_i, where i=1..8), and the true resistance of the NTC temperature sensor is determined by the formula:

$$R_{therm} = R_{ref} \frac{(ADC_1 - ADC_4) + (ADC_2 - ADC_3)}{(ADC_5 - ADC_8) + (ADC_6 - ADC_7)} \tag{4.2}$$

where the R_{ref} is the resistance of the reference resistor integrated in the RBFE electronics. The main advantage of the FE system with the digital RBFE is its ability to mitigate virtually all systematic effects of long term voltage drifts and induced offsets due to the non-ideal characteristics of the system components (voltage offset at the inputs of individual discrete components of the FE electronics, thermocouple effects at the electrical junctions of different materials, temperature and supply voltage dependences, etc.). One RBFE configuration of the FE readout system reads a total of 16 ESS temperature sensors.

Figure 4.5: A block diagram of the redundant configuration of the front-end electronics within a single ESS Readout Unit (left) and a photo of one ESS Readout Unit ready to be installed at P5 (right).

The functioning of the FE components is digitally controlled by a dedicated Microchip PIC 18F452 microcontroller designed in CMOS FLASH technology [43]. The microcontroller, in addition to other properties, is characterized by its 8-bit data bus, 10-bit A/D converter, three I/O ports and one port for serial communication. The microcontroller performs A/D conversion and digital filtering of the output signal of the RBFE electronics in all of the 8 modes of measurement. The collected measurement results are sent by the PIC MCU via a custom ESS protocol over a serial RS485 connection to a higher layer of the ESS.

The complete FE layer for the readout of both the temperature and the WLD sensors consists of 12 readout units equipped with the ESS FE electronics. In order to ensure a high level of availability of the system, the readout units are designed so that each component of the FE readout electronics has a redundant pair within the same unit. In this way, each unit has two microcontrollers and two RBFE components. Therefore, each unit is able to read a set of 4×4 redundant temperature sensors and two WLD sensors, corresponding to four different Supermodules of the ECAL.

In order to reduce the loss of information about the temperature inside of a module in an ECAL Supermodule, the information from the sensor of each module is "divided" between redundant subsystems of a ESS readout unit. In particular, information from the

sensor of each module is distributed to a redundant set within the ESS readout unit so that all the "left" sensors in sensor pairs are read by one, while the "right" sensors are read by the other redundant part of the ESS readout unit. In accordance with the principle of redundancy, each unit has a pair of redundant systems and power electronics within the unit. In the following section we will describe the process of the ESS communication and the complete higher layer of the ESS which has also been implemented in a fully redundant way.

A block diagram of the redundant configuration of the FE electronics within a single ESS Readout Unit and the final design of the ESS Readout Unit ready for installation are shown in Figure 4.5. All initially anticipated ESS Readout Units have been fully designed and implemented by the CMS Belgrade Group in collaboration with the Institute of Particle Physics of ETH Zürich, and supplied to CERN by the end of the year 2006.

4.3 The interlocking system

4.3.1 The PLC system

The part of the ESS that is responsible for autonomous and reliable acquisition and processing of the signals from the lower FE layer, as well as for an autonomous and reliable generation of the interlock signal, has been implemented using the industrial Siemens PLC system of the S7-400H family, and the Siemens PLC system of the S7-300 family [39]. The distribution of interlock signals between the ESS and other ECAL subsystems (HV, LV and Cooling System) has been implemented using specially designed ESS Interlock Units (ESS IUs). The decision on the implementation of the ESS PLC systems in this way has been made in accordance with an officially established LHC policy on the implementation of control systems in the LHC experiments [44].

The whole ESS PLC system has been implemented in the form of a distributed redundant configuration with Profibus communication between the two of its subsystems. The first part of the system is implemented as a PLC system of the Siemens S7-400H family with the following modules:

- S7 PS 407 10A - two modules for a redundant power supply system;

- S7 CPU 414-4H CPU - two CPU modules for redundant information processing;

- S7 CP 443-1 - two Ethernet modules for redundant communication with the software part of the ESS.

The function of this subsystem is to process information received from the lower layers of the ESS and to generate appropriate interlock signals and distribute them via communication and digital I/O modules installed in the second part of the distributed PLC system. The 414H PLC CPU modules are configured to operate in a redundant mode and are connected to each other via a dedicated optical-fiber link for a full synchronisation of their operation.

The second part of the system has been implemented as a Siemens S7-300 PLC system, distributed over the Profibus protocol, and with the following modules:

- 2 x IM 153-2 S7 - two modules for redundant communication with the S7-400H PLC part of the ESS;

- 2 x S7 CP 341 - two modules for redundant RS485 communication with the FE layer of the ESS;

- 2 x S7-321 modules 32xDIx24V for receiving external hardwired alarms from the ECAL Cooling System and the CMS DSS;

- 5 x S7-322 modules 32xDOx24V for sending hardwired interlock signals to the HV and LV systems of ECAL and to the CMS DSS.
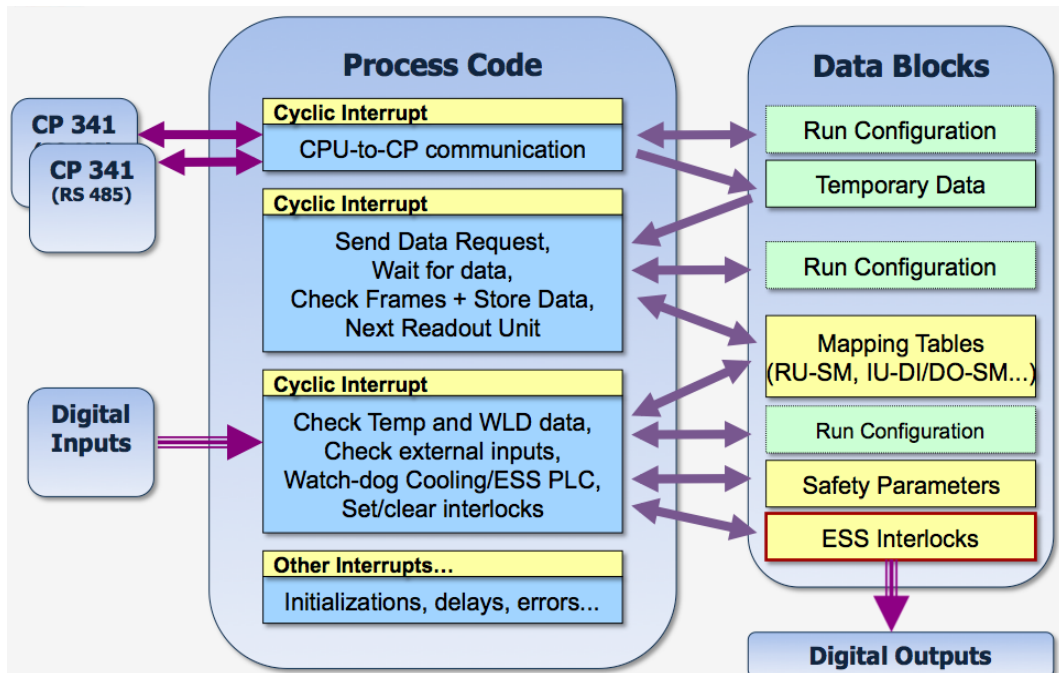
Figure 4.6: A photograph of the ESS PLC system and an interlock unit configured as described in the text, installed in the ECAL Integration Centre (left), and a photo of the ESS PLC system in stalled at the UXC area at P5 (right).

The role of this subsystem is to collect information from sensors of a lower layer of the ESS via RS485 serial interfaces and to trigger appropriate interlock signals for the other ECAL detector subsystems. The interlock signals are of the relay type and are distributed to the appropriate system through specially designed ESS interlock units that also enable local visualisation of the status of interlock signals.

The ESS has been designed in such a way that its readout units and the PLC system communicate and exchange sensor data and control information continuously. Since one of the main objectives of the ESS has been a very high degree of reliability, a specific ESS multi-point communication protocol that provides reliable information exchange between ESS readout units and the PLC system has been designed. The design of the ESS protocol has been based on parts of international IEC standards for telecontrol protocols EIA RS-485:1983, UART FT 1.2, IEC 870-5-1 and IEC 870-5-2. The implementation of the ESS

protocol within the PIC MCUs of each readout unit and within the ESS PLC has been a huge effort and its accomplishment has marked a major milestone in the development of the ESS.

The ESS PLC system has been implemented in such a way that all of its critical components have a redundant partner. It has been configured and programmed as a "fault-tolerant" system for most of the anticipated critical situations. The system has also been designed and configured in such a way that in all other problematic situations (e.g. loss of the power supply) it behaves as a simple "fail-secure" system - by design it generates interlock signals and takes all the ECAL detector subsystems safely to their OFF state. Figure 4.6 shows the photograph of the ESS PLC interlock system installed in the underground service cavern of the CMS experiment.

Figure 4.7: A functional diagram of the code organisation and operational logic of the the PLC system used for the ECAL Safety System.

The complete ESS PLC system has been designed and programmed in a collaboration between the ETH Zürich and the CMS Belgrade Group, and has passed several reviews of the system software by the expert body nominated by the CMS ECAL collaboration in the year 2007. The functional block diagram of the logic of the ESS PLC code is presented for illustration in Figure 4.7. Its detailed description is beyond the scope of this work.

4.3.2   Digital signal filtering

The main requirements that the digital filter for the ESS signals had to satisfy have not been based on the need for ideal characteristics of signal transmission functions. Instead,

these were based on the need for a system that could provide a quick response to all low frequency changes in the temperature signal, and the need for a stable and robust system with minimal memory requirements. All requests, along with their detailed specifications, can be systematised as follows:

- a fast response to the impulse and step excitation. The speed of the filter response was one of the important requirements for the synthesis of the ESS filter. The filter had to be able to achieve 90 % of the new equilibrium value not later than 5-7 readout samples after the time of the change of the excitation signal;

- a small "overshoot" value for the filter response to the step excitation. Since CMS has predefined the thresholds for activation of temperature alarms, it must not be allowed that any of these levels gets activated as a result of the "overshoot" in the response to the external excitation. The requirement was set that the size of the "overshoot" should not exceed 15% of the change of the amplitude of the excitation;

- a low order of the digital filter. The low order filter was a direct consequence of the minimal memory requirements. This type of filter could be easily implemented in the micro-controller with limited memory resources used in the ESS Readout Units;

- a low frequency pass filter. Since the expected temperature change is very slow even in critical situations, it was highly desirable that the filter effectively removes all the high-frequency components in the signal. The requirements were set in such a way that the position of the frequency bandwidth limit was supposed to be in the zone of 5-10 Hz, with the suppression in the no-pass band of about 60 dB;

- full stability and tolerance with respect to the effects of digitisation and the choice of initial conditions. Given that this is a system of high importance for the control and proper operation of the ECAL, these requirements had to be fully respected.

The condition that the filter must have small memory requirements immediately implied the selection of the IIR filter type [45]. The analysis of the impulse and step response of the IIR filters of the order N = 2, based on analog Butterworth, Chebyshev and Elliptic filter functions [45, 46], have led us to the conclusion that the best features were offered by the second-order Butterworth filter.
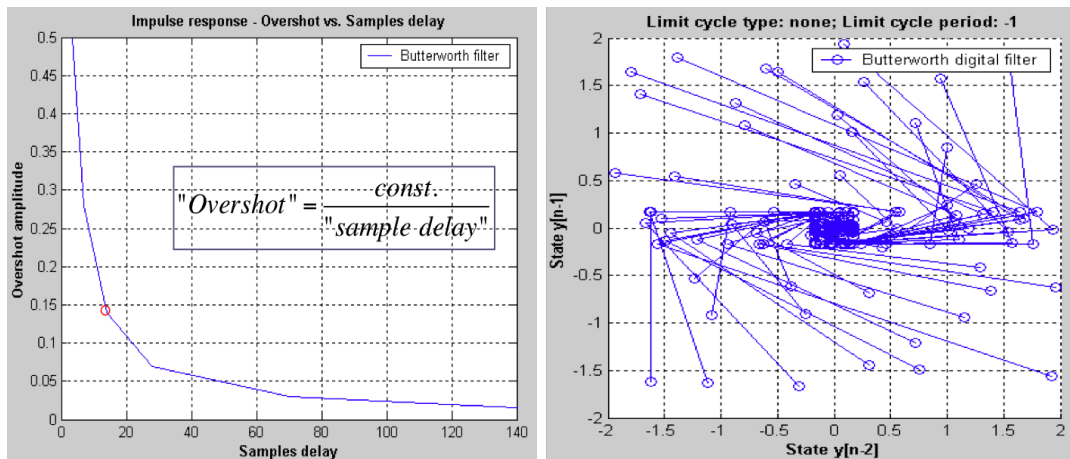
Requests for a small "overshoot" and the rapid response to the excitation are mutually contradictory. It was therefore necessary to find an appropriate "working point" of the filter and an optimal set of parameters that would achieve the desired filter characteristics. Figure 4.8 (left) shows the dependence of the magnitude of the "overshoot" on the delay of its response expressed in the number of sampling steps. The same figure shows the selected working point which corresponds to a maximum "overshoot" of less than 15 %, with a delay of the filter response of about 7-8 samples (time required to reach 90 % of the excitation signals).

After fixing all parameters of the filter described, a discrete transfer function of the filter was derived. The resulting transfer function of this filter represented in the non-

factorised form was:

$$H(z) = \frac{0.020083 + 0.040167z^{-1} + 0.020083z^{-2}}{1 + 1.561018z^{-1} + 0.641352z^{-2}} \quad (4.3)$$

The transfer function was used to determine the difference equation that was used for the direct filter implementation. The analysis of the position of the poles of the transfer function with the methods described in the reference [46] showed that the filter was stable and resistant to all potentially dangerous digitisation effects. Figure 4.8 (right) shows the results of the simulation analysis [46, 47] of the digital filter in its state space. The analysis was performed in Matlab 7.0.1 and showed that the filter does not have "overflow" limit cycles and that regardless of its initial state, in the absence of an input excitation, the system asymptotically tends to zero value of the output signal. The filter was, therefore, found to be resistant to nonlinear effects of digitisation and the choice of initial conditions.

Figure 4.8: The dependence of the overshoot on the delay in the filter response (left) and the results of a simulation analysis of the selected digital filter in its state space y [n-1], y [n-2] (right).

Based on the considerations presented, it was clear that such a digital filter met all the initial design requirements. In addition, the choice of the Butterworth filter of the second order provided a filter with almost linear phase characteristics. This feature allows that the delay of the spectral components of the signal is almost equal after passing through the filter. Consequently, the designed filter does not introduce any noticeable distortion of the input signal.
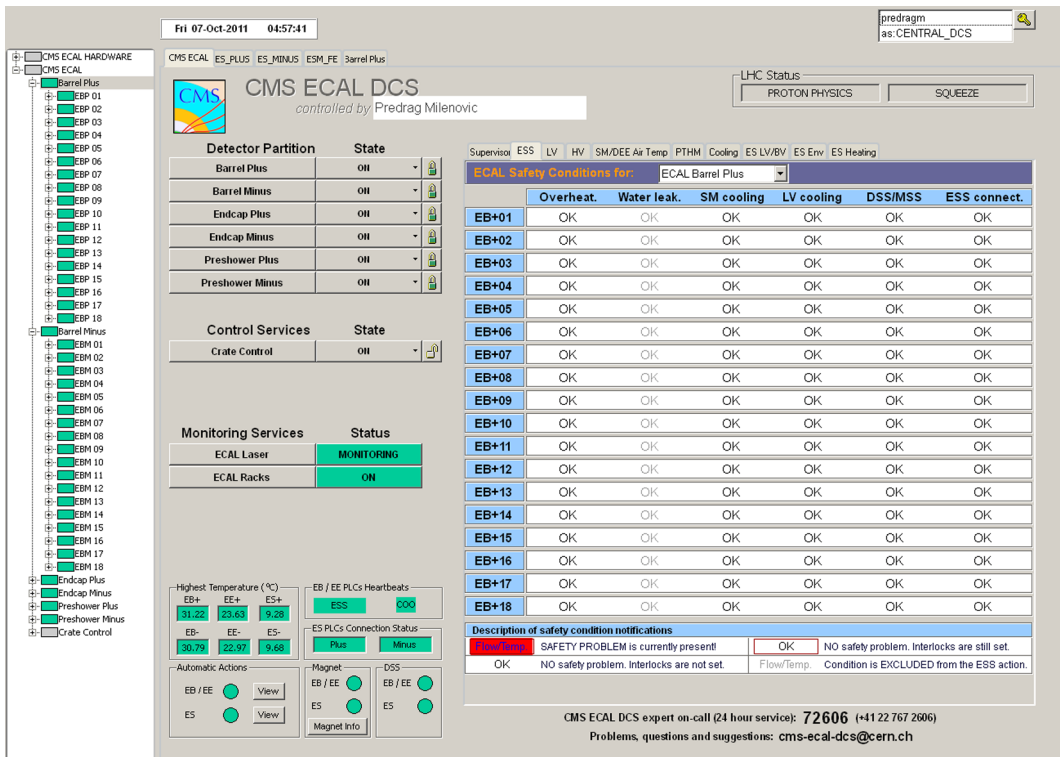
4.4 Monitoring and control

The application for monitoring and control of the ESS have been developed with the supervisory control and data acquisition software WinCC OA and standard JCOP frame-

work components, as described in section 3.3. The system was built over a period of several years and the libraries required for core monitoring and control, excluding the graphical user interface, account for about 5,000 lines of code.

The application was implemented as an independent JCOP Framework component [35]. The component facilitates an automatic creation of the internal structure and the FSM hierarchy of the ESS, the full parameterization of the system and the establishment of the connection with the ESS PLC system. Fully automated installation process allowed the ESS software to be easily installed or reinstalled in each area of the ECAL testing and operation.

Figure 4.9: Screenshot of the ESS summary view within the ECAL DCS application at the P5 with the safety status of the ECAL detector.

The ESS application functionality has been split into the two logical categories. The first part of the application is solely dedicated to the monitoring of the safety operations of the ESS, including the health status of the ESS PLC, communication with the ESS FE system and distribution of hardwired input and output signals. The application allows to manually set and clear interlocks, but does not allow for change of the predefined safety thresholds stored in the ESS PLC. The second part of the application is responsible for the monitoring of the ESS temperature sensors and the water leakage sensors installed in the ECAL and is able to trigger automatic controlled shutdown prior to the safety actions. The application has its own limits for the control actions which are continuously compared to the ones set up in the ESS PLC and are only allowed to be tighter.

The ESS control software also provides some additional functionality. It allows for large number of parameters to be stored to or loaded from the ECAL Configuration Oracle database. It features an internal watch-dog system to monitor communications with the ESS PLC system and capable of sending warning messages in critical situations by e-mail and via the GSM network. It also provides the archiving of the ESS sensor and status information in the ECAL Conditions Oracle database. The screenshot of two user interface panels of the ESS applications is shown in Figure 4.9.

4.5 Testing and performance

In the period from 2002 until the year 2007, numerous tests and evaluations of prototypes of the ESS have been conducted. The tests have been performed during the development of the system in the laboratories of ETH Zürich, during the integration and testing of ECAL Supermodules in the areas 867, 887-H4 and 887-H2 at CERN, as well as with the OPTIS proton beam at PSI in Villingen, Switzerland.

The main goal of the tests carried out in PSI was a complete evaluation of the tolerance of the various ESS components up to doses of radiation and fluences of hadrons that are expected at the locations where these components will be installed in the ECAL and in the CMS experimental cavern. The subsequent tests focused on the study of the system performance and its integration with the other ECAL subsystems. A particular emphasis has been put on resolving the various outstanding issues that we encountered during the process of development and implementation. The most important issues that had to be addressed during these tests were:

- a possibility to calibrate the readout system and sensors to an accuracy better than 0.1 degree Celsius;

- a study of the temperature distribution within a single ECAL module and temperature sensitivity of sensors in the presence of the ECAL front-end electronics;

- a test of the interference of the readout system of WLD and temperature sensors with the general detector ECAL readout system;

- the reliability of the ESS system for the distribution of interlock signals.

Most of these performance analyses on the system prototypes were performed at test areas in CERN. All the issues and concerns listed above have been successfully addressed and solved. The details of these tests and the complete work on the design of the ESS were published and can be found in the references [31, 40].

4.5.1 Irradiation tests of the ESS components

In case of an integrated LHC luminosity of $5 \times 10^5 \, \mathrm{pb}^{-1}$, an absorbed dose of $2 \times 10^3 \, \mathrm{Gy}$ and fluences of neutrons and charged hadrons of about $3 \times 10^{13} \, \mathrm{cm}^{-2}$ can be expected in the barrel part of the ECAL [28]. Similarly, the absorbed dose and fluence of hadrons are

5×10^4 Gy and 2×10^{14} cm^{-2} in the endcap part of the ECAL, respectively. The expected values of the absorbed dose and hadron fluence in the CMS experimental cavern, where the ESS FE electronics is installed, amounts to 1 Gy and 10^{10} cm^{-2} respectively [11]. For this reason, a confirmation of the tolerance of several components of the ESS to radiation effects induced by the corresponding radiation doses was of paramount importance. These components were:

- the sensors and cables for the readout of the ESS sensors as system components which are located inside the ECAL detector;

- the Maxim 4582 multiplexers, RBFE electronics and PIC micro-controller, as well as system components integrated within the readout units, as system components which are located at specified locations inside of the CMS experimental cavern.
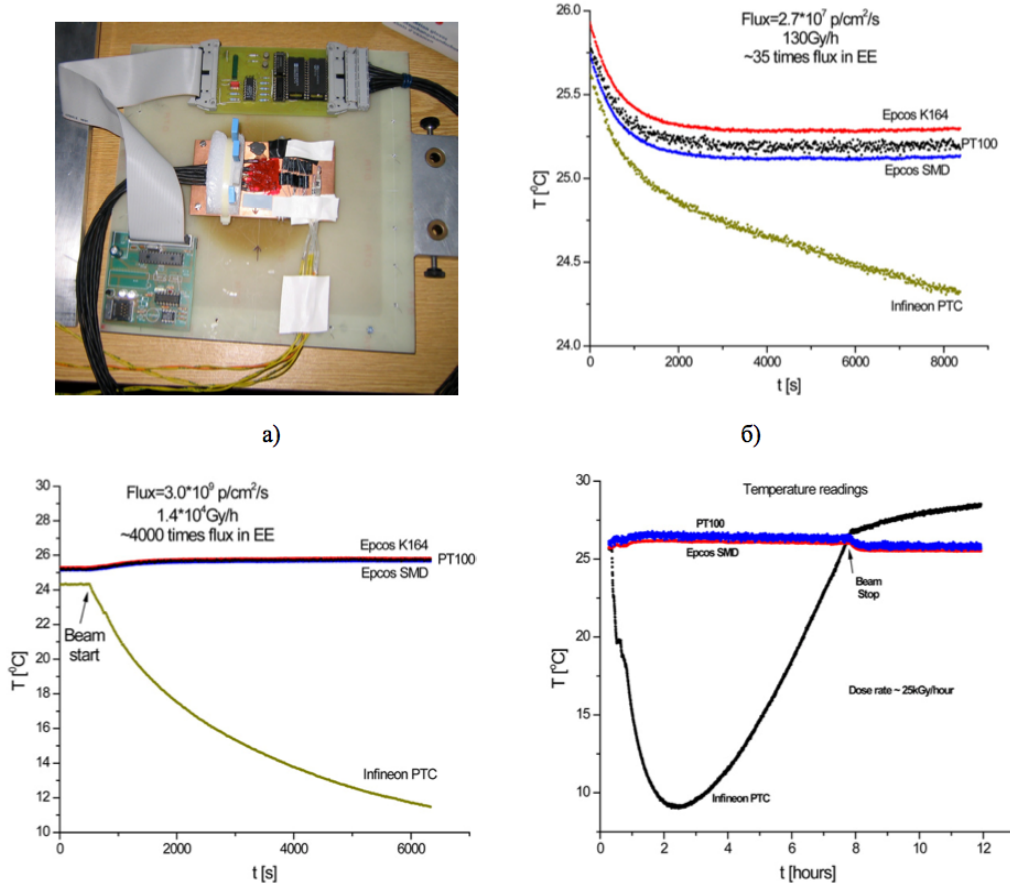
The tolerance of the sensor readout cables (insulation layer made of polyethylene terephtalate) and Maxim 4582 multiplexers to the radiation-induced effects by these doses of radiation were proven in previous studies of other research groups with similar needs at CERN [48]. In order to carry out checks and verification of radiation tolerance of the remaining components of the ESS, the experiments were performed with the OPTIS proton beam at PSI. The aim of the experiments was to test the tolerance of the components to the cumulative effects of radiation (ionization effects, the defects of the crystal lattice), as well as the "instantaneous" single-event effects (SEE) of radiation caused by the deposition of energy due to the passage of a single particle [49].

Irradiation of the temperature sensors was performed with a beam of protons with an energy of 64 MeV and with a maximum flux of 1.1×10^{10} protons cm^{-2} s^{-1}. The beam simulated the effects of both the neutron radiation flux of 4×10^{13} cm^{-2} h^{-1} , and the ionising radiation dose of 25 kGy h^{-1} [50, 51]. Several candidates for the ESS sensors have been tested: EPCOS, Siemens and BTC temperature sensors of the NTC type, as well as one Infineon temperature sensor of the PTC type. In addition, one temperature sensor of the PT100 type (whose radiation resistance has already been verified) was positioned in the vicinity of the other sensors in order to monitor any irradiation-induced warming of the test board.

All temperature sensors were initially exposed to a low flux radiation: in the first iteration the flux was 2.7×10^7 protons cm^{-2} s^{-1}, while in the second iteration it was 3×10^9 protons cm^{-2} s^{-1}. After this iteration, all the sensors were exposed during a period of 8 hours to the maximum available flux of 1.1×10^{10} protons cm^{-2} s^{-1} (equivalent dose of 25 kGy h^{-1}) to the equivalent cumulative dose of 200 kGy and a fluence of 3×10^{14} protons cm^{-2}. During the experiment, the ESS readout system was operational and was continuously reading and archiving the signals from the tested sensors.

Figure 4.10 (upper left) shows the photograph of the test board with tested sensors and components of the FE electronics of the ESS readout system, after one iteration of the irradiation. The results of the tests of temperature sensors for all three iterations are shown in the plots in the same figure. The main result of these experiments was that the NTC type temperature sensors do not exhibit any change of characteristics during the irradiation and, therefore, can safely be used within the ECAL Supermodule. On the

contrary to the NTC sensors, the Infineon PTC sensors showed abnormal behaviour due to radiation defects (Figure 4.10, lower right).

Figure 4.10: A photograph of the board with tested sensors and components of the ESS front-end electronics (upper left), comparative results of sensor response during the exposure to low radiation flux in two cases described in the text (upper right, lower left) and comparative results of sensor response during the exposure to the maximum radiation flux (lower right).

The irradiation of the FE components of the ESS readout system has been performed with the same proton beam energy of 64 MeV, but with a minimal achievable OPTIS beam flux of 2.7×10^7 protons cm^{-2} s^{-1}. The components were irradiated for periods of 30 minutes to the total equivalent dose of 60 Gy and the total neutron fluence of 9×10^{10} cm^{-2} [50, 51]. During the period of irradiation the ESS readout system was operational and its performance was actively monitored. The testing has shown that the FE electronics was functioning reliably during the period of irradiation, without detectable change in any of its analog parameters (S/N ratio, internal offset of discrete components, amplification of the A/D converters, etc.).

An additional goal of the test was to check the tolerance to the single-event effects of radiation. During the period of irradiation of the FE components only one SEE effect

has been observed [31]. The effect has been manifested through the change of the state of one bit of the CMOS FLASH memory of the tested microcontroller. Bearing in mind the equivalent flux Φ_{eq} of the radiation during this test, we have concluded that the effective cross section for the SEE events is practically negligible $\sigma_{\mathrm{SEE}} = N_{\mathrm{SEE}}/\Phi_{\mathrm{eq}} = 5.6 \times 10^{-12}\,\mathrm{cm}^2$, and that the PIC microcontroller can be safely used as a core of the ESS readout system.

4.6   Conclusions

Throughout the whole phase of the prototyping, testing, integration and commissioning of the CMS ECAL, the ESS has been providing constant and reliable support for all the operational tasks, while going through the same development phases itself. Until the beginning of 2009 it has evolved in the fully operational, very stable and robust system, which provides the maximum safety to the ECAL [52].

During the LHC data taking periods from 2009 until the year 2011, the ESS has shown high levels of availability and has proven to be capable of taking protective actions based on anticipated safety hazards. Strengthen with a 24/7 expert on-call service provided by the ECAL DCS team it has contributed to the high level of ECAL readiness for data taking. Statistics from October 2010 to August 2011 from CMS DCS indicate that the ECAL had an overall readiness of 97.8% during periods when LHC was delivering stable colliding beams [37]. In addition to this, outside of LHC data taking periods, the ECAL DCS and the ESS monitor the conditions of the detector and enable parts of the detector to be powered on and off as required.

Based on the current experience, together with the fact that the whole ECAL DCS will be strengthen with the planned hardware and software upgrades [37], we are confident that the ESS and the whole ECAL DCS will continue to provide an excellent support to the operation of the ECAL in the future.

Part II

Search for physics beyond the Standard Model

Chapter 5

Physics at the Large Hadron Collider

> The only voyage of discovery [...] consists not in
> seeing new landscapes, but in having new eyes.
> M. Proust[1], 1923.

5.1 The Standard Model of particle physics

The **S**tandard **M**odel (SM) of particle physics describes the present understanding of the
fundamental constituents of matter and their interactions and is undoubtedly one of the
central achievements of the physics research in the 20th century. It has been formulated
as a renormalizable model in the framework of relativistic quantum field theory [25-34],
which has demonstrated to be a succesful way to describe nature at the energy scales we
have probed in the experiments up to the present day. The framework of the quantum
field theory and its Lagrangian formalism allowed to elegantly accommodate in the model
the essential elements: space-time symmetry, additional internal symmetries, causality
and local interactions.

In general, realistic physics models are built within this framework by providing three
sets of ingredients: the gauge symmetry of the Lagrangian, the set of fermion and scalar
fields and their properties under the gauge transformations, as well as the pattern for
an eventual spontaneous breaking of this symmetry [53]. The dynamics of these models
is completely defined by specifying the most general renormalisable Lagrangian that is
invariant under the given gauge symmetry and that provides a mechanism for the breaking
of this symmetry. Within this framework, the global symmetries are usually not imposed,
but arise indirectly due to the absence of non-renormalisable terms in the Lagrangian.
Any model specified in this way has a finite number of a-priori unknown parameters, which
need to be extracted from the experimental observations before the model predictions can
be tested in details.

The SM of particle physics is formulated within this framework as the model with the

---

[1]M. Proust, In Search of Lost Time, Vol. V: The Captive, 1923.

gauge group of the Lagrangian:

$$G_{SM} = SU(3)_C \times SU(2)_L \times U(1)_Y \tag{5.1}$$

where the subscript "C" designates the colour symmetry related to the strong interactions, while subscripts "L" and "Y" designate the weak isospin symmetry and the "hypercharge" symmetry related to the electroweak interaction. In order to preserve this gauge symmetry, a set of massless vector fields is introduced in the model: the eight gluon fields G_a^μ ($a = 1, ..., 8$), the three weak bosons W_b^μ ($b = 1, 2, 3$), and the single hyper-charge boson B^μ.

The model comprises three generations of fermions, each generation consisting of fermions which are described by a spinor field and transform according to the following five representations of the G_{SM} group:

$$Q_i(\mathbf{3}, \mathbf{2}, +1/6) \ , \ U_i(\mathbf{3}, \mathbf{1}, +2/3) \ , \ D_i(\mathbf{3}, \mathbf{1}, -1/3) \ , \ L_i(\mathbf{1}, \mathbf{2}, -1/2) \ , \ E_i(\mathbf{1}, \mathbf{1}, -1) \tag{5.2}$$

The index $i = 1, 2, 3$ represents the fermion generation and the set of numbers (C, L, Y) designates the representations of the subgroups $SU(3)_C$, $SU(2)_L$ and $U(1)_Y$ of the group G_{SM}. Any fermion can be in one of the two distinguishable states which each transform according to two different representations of the Lorentz group. These two states are commonly named as left- and right-handed states and this particle property is named chirality. In (5.2), $Q_i(3, 2, +1/6)$ and $L_i(1, 2, -1/2)$ represent the pairs of fermions which have left-handed chirality and transform as the weak isospin doublets under $SU(2)_L$. On the other side, the $U_i(3, 1, +2/3)$, $D_i(3, 1, -1/3)$ and $E_i(1, 1, -1)$ represent individual right-handed fermions and transform as the weak isospin singlets under $SU(2)_L$. The three representations Q_i, U_i and D_i describe two quarks, while the two representations L_i, E_i describe one charged lepton and one neutrino in each of the three generations of fermions. According to experimental observations, quarks and charged leptons can be both left-handed and right-handed chiral state. On the other hand, the SM assumes that neutrinos are massless and behave as left-handed fermions. This choice of representations for the fermions is a direct consequence of the observed chiral asymmetry of the electroweak interactions [54]. Every fermion has a corresponding antiparticle and the model comprises the three generations of antiparticles in a way equivalent to the one described above.

The model also comprises a single scalar particle, described by a doublet of complex scalar fields, which transforms according to the representation:

$$\phi(\mathbf{1}, \mathbf{2}, +1/2) \tag{5.3}$$

of the G_{SM} group. The SM also postulates a non-vanishing vacuum expectation value (v.e.v.) for this scalar field:

$$\langle \phi \rangle = \begin{pmatrix} 0 \\ v/\sqrt{2} \end{pmatrix} \tag{5.4}$$

with a symmetry that is lower than the symmetry G_{SM} of the Lagrangian. Consequently, this structure of the vacuum expectation value induces a breaking of the original gauge group into the lower unbroken gauge group:

$$G_{SM} \rightarrow SU(3)_C \times U(1)_{EM} \tag{5.5}$$

and alters the dynamics of the fields in the model in a way which allows for the presence of massive gauge bosons and, hence, the description of short-range interactions [55, 56]. In particular, the model with the altered dynamic features three massive vector fields W^+, W^- and Z^0 which describe the weak interactions, and one massless electrically neutral vector field A^0 which describes the electromagnetic interactions.

The SM Lagrangian, $\mathcal{L}_{SM}$, is the most general renormalizable Lagrangian that is consistent with the gauge symmetry (5.1) and particle content (5.2) and (5.3). It fully defines the dynamics of the fields in the model and can be divided in three parts:

$$\mathcal{L}_{SM} = \mathcal{L}_{gf} + \mathcal{L}_{Yukawa} + \mathcal{L}_{ewsb}. \tag{5.6}$$

The $\mathcal{L}_{gf}$ part describes the free propagation of gauge and fermion fields, the coupling between these fields, as well as the self-coupling of the gauge fields. The fermion fields which describe leptons couple only to the weak gauge bosons, while the quark fields couple to both the weak gauge bosons and the gluon fields. The $\mathcal{L}_{gf}$ features three undetermined parameters, the strengths of the electroweak and strong gauge couplings g_1, g_2, g_3, and its predictions have been thoroughly tested through a large number of experiments conducted at SLC, LEP and Tevatron during several decades of the 20th century.

The $\mathcal{L}_{ewsb}$ part of the Lagrangian describes the propagation and the self-coupling of the scalar field ϕ, as well as its coupling to the gauge fields:

$$\mathcal{L}_{ewsb} = (D_\mu \phi)^\dagger (D^\mu \phi) - \mu^2 \phi^\dagger \phi - \lambda (\phi^\dagger \phi)^2. \tag{5.7}$$

The role of this part of the Lagrangian is to provide a mechanism for the breaking of the electroweak symmetry once the ϕ field acquires a non-vanishing v.e.v. (5.4). The complete mechanism of the spontaneous symmetry breaking and how the presence of one scalar field can allow for the description of massive fermions and bosons has been mastered in 1964 [55, 56, 57, 58]. Today, it is commonly referred to as the Higgs mechanism, while the excitation of this scalar field around the v.e.v. is commonly referred to as the Higgs boson. The $\mathcal{L}_{ewsb}$ contains two parameters μ^2 and λ, which together determine the mass of the scalar m_h and the strength of its self-coupling. These parameters have not been fully understood to date and are only weakly constrained by the experiments performed in the era before the LHC.

The $\mathcal{L}_{Yukawa}$ part contains terms that describe the so-called Yukawa-type of coupling between fermions and the scalar field ϕ:

$$\mathcal{L}_{Yukawa} = -\lambda^d \bar{Q} \phi D - \lambda^u \bar{Q} \tilde{\phi} U - \lambda^e \bar{L} \phi E + h.c. \tag{5.8}$$

After the scalar field ϕ acquires a non-trivial v.e.v. (5.4) and induces a spontaneous symmetry breaking, this type of coupling effectively results in terms which describe the masses of elementary fermions. The masses of the majority of composite matter particles (e.g. baryons) do not arise from this mechanism, but from the interaction energy of their fermionic constituents.

The lepton part of the $\mathcal{L}_{Yukawa}$ involves three undetermined parameters, which are usually chosen to be the physical masses of three experimentally observed charged leptons. The Yukawa interactions for the quark fields are described by ten undetermined parameters. These are commonly chosen to be the physical masses of six experimentally observed quarks and the four parameters which quantify the experimentally observed mixing of the quark weak eigenstates between three generations [59, 60].

Table 5.1: A summary of the main properties of scalar and vector bosons, as well as fermion particles in the Standard Model of particle physics. Every particle has a corresponding antiparticle. All the particles except the Higgs scalar have been experimentally observed.

Names	symbol	spin	el. charge	mass [GeV]
Higgs boson	h	0	0	not yet observed
e.w. gauge bosons	A^0	1	0	0
	Z^0	1	0	91.188 ± 0.002
	$W^\pm$	1	± 1	80.40 ± 0.02
gluons	g	1	0	0
quarks	u	1/2	2/3	$1.7 - 3.3 \times 10^{-3}$
	d	1/2	$-1/3$	$4.1 - 5.8 \times 10^{-3}$
	c	1/2	2/3	1.27 ± 0.09
	s	1/2	$-1/3$	0.101 ± 0.029
	t	1/2	2/3	172 ± 1.3
	b	1/2	$-1/3$	4.19 ± 0.18
leptons	ν_e	1/2	0	$< 0.28 \times 10^{-6}$
	e	1/2	-1	5.11×10^{-3}
	ν_μ	1/2	0	$< 0.28 \times 10^{-6}$
	μ	1/2	-1	0.105
	ν_τ	1/2	0	$< 0.28 \times 10^{-6}$
	τ	1/2	-1	1.77

The SM has an accidental global symmetry

$$U(1)_B \times U(1)_e \times U(1)_\mu \times U(1)_\tau \tag{5.9}$$

where $U(1)_B$ corresponds to the symmetry that conserves the number of baryons and the other three correspond to the symmetries that conserve the number of leptons in each generation separately. The quarks carry baryon number, while leptons and bosons do

not. The SM commonly normalizes this number such that the proton has $B = 1$ and each quark carries the baryon number of $B = 1/3$. In case of the lepton number, in the SM each generation carries its own lepton number, L_e, L_μ and L_τ. The summary of main properties of both bosonic and fermionic particles is given in Table 5.1.

One of the most important steps in the development of the model, was a proof that gauge theories with spontaneous symmetry breaking are renormalizable which has consequently led to the Nobel prize of Physics, awarded to t'Hooft and Veltman for the year 1999. This proof has placed the electroweak interaction in the class of renormalizable non-Abelian gauge symmetries, allowing perturbative calculations of all the relevant processes.

The model formulated in this form incorporates in an elegant and organised way all the elementary fermions observed in nature. It describes all the interactions as local interactions mediated by corresponding gauge bosons, whose dynamics is driven by the Lagrangian $\mathcal{L}_{SM}$. And all of the properties of the model and its predictions have been experimentally verified with great success, including the peculiarities of the dynamics of some of these interactions (e.g. asymptotic freedom in strong interactions [61]). The only missing part is the verification of the existence of the Higgs boson, which has not been observed despite many years of experimental searches. It is expected that the experiments at the LHC collider should give us a definite answer whether the Higgs boson exists and the model outlined above is valid description of nature or not.

The framework of renormalizable field theory also gives us an opportunity to understand the model in a broader way. Namely, any hypothetical theory which properly describes the fields and interactions in the nature at some very high energies can be represented by its own Lagrangian $\mathcal{L}_{HE}^{eff}$. At sufficiently low energies this theory will be described by the unique renormalizable theory with the given low-energy spectrum and symmetries, whose Lagrangian is the $\mathcal{L}_{SM}$. It can be shown that the deviations between the predictions of the two theories can be parametrized through these local low-energy effective field theory considerations as:

$$\mathcal{L}_{HE}^{eff} = \mathcal{L}_{SM} + \sum_{d \geq 4} \sum_i \frac{C_{d,i}}{\Lambda_i^{d-4}} O_i^{(d)} \tag{5.10}$$

where $C_{d,i}$ are dimensionless coefficients and the $O^{(d)}$ are operators of mass dimension $d \geq 4$ built up from fields of $\mathcal{L}_{SM}$ [61]. The Λ_i represent mass scales which are much larger than the masses in the spectrum of $\mathcal{L}_{SM}$ and may depend on the mass scales inherent to $\mathcal{L}_{HE}^{eff}$. This effectively means that, in general, the Lagrangian of the Standard Model can be just an effective field theory approximation of the Lagrangian that describes the physics of particles and their interactions in a more general way. But the effects of the new physics at our scales are expressed via effective operators and, hence, are heavily suppressed. The ultimate goal would be to uncover these effects and to discover the theory that would fully describe the fields and interactions in the nature also at very high energies. This theory might also be able to provide us with the answers to at least some of the limitations and open questions within the Standard Model.

5.2 Limitations of the Standard Model

The Standard Model of particles and their interactions outlined in the previous sections presents a remarkably successful description of most of the observed phenomena in particle physics. Still, although the experimental frontier has advanced into the TeV range with no unambiguous hints of additional new phenomena, it seems clear that the Standard Model will have to be extended to describe physics at higher energies. In particular, a new framework will be required at the scale $M_P = 2.4 \times 10^{18}\,\text{GeV}$, where quantum gravitational effects are expected to become important.

There are at present also many reasons to expect new phenomena at the weak scale $m_{weak} \sim 100\,\text{GeV} - 1\,\text{TeV}$. Namely, even with the Higgs discovered, the SM would have both conceptual and phenomenological shortcomings. In fact, several theoretical arguments indicate that the SM is not the ultimate description of nature:

- the SM can accommodate, but cannot give a fundamental explanation for the observed number of generations of fermions and their mass spectrum;

- the model does not provide a fundamental principle that would exlain so many different types of interactions;

- it has been recently established that neutrinos have a non-zero mass. While this can be naturally accommodated in simple extensions of the SM, there is still no answer on the nature of the neutrinos [62, 63];

- the SM in its current form is unable to predict the asymmetry between the matter and the antimatter needed to explain that Universe is made entirely of matter;

- the model also can not account for a large fraction of the mass of the universe inferred from the recent astrophysical observations.

In the following subsections we will present in detail a few of the important shortcomings. In particular, we will focus on those which potentially can be overcome by a specific class of the extensions of the SM named Supersymmetric extension of the SM. In the section that follows, we will present the details of that class of models and some of the most important phenomenological implications.

5.2.1 The problem of naturalness

The results of the experiments which have performed thorough study and precise measurements of the properties of the electroweak interactions have established that the v.e.v of the SM scalar field should be approximately $174\,\text{GeV}$ and that the mass of the Higgs boson m_h^2 should be approximately of the order of a few $(100\,\text{GeV})^2$ [64]. On the other side, in accordance with the Lagrangian $\mathcal{L}_{SM}$, m_h^2 receives enormous radiative corrections from the virtual contributions of particles that couple, directly or indirectly, to this scalar field. As a consequence, the mass of the Higgs boson in the SM is given by

$$m_h^2 = m_h^{0\,2} + \Delta m_h^2 \tag{5.11}$$

where $m_h^{0\,2}$ is the bare mass parameter indirectly present in the Lagrangian $\mathcal{L}_{SM}$. The size of the contribution of radiative corrections can be roughly estimated as:

$$\Delta m_h^2 \approx \frac{\lambda^2}{16\pi^2} \int^{\Lambda} \frac{d^4p}{p^2} \approx \frac{\lambda^2}{16\pi^2} \Lambda^2, \tag{5.12}$$

where λ is a dimensionless gauge Yukawa coupling, and Λ is the hypothetical energy scale at which the SM is no longer a valid description of nature. Since the contribution from the radiative corrections Δm_h^2 is roughly proportional to Λ^2, it is "natural" to expect the Higgs mass to be within an order of magnitude of Λ [65, 66]. Bearing in mind that unitarity and precision constraints require m_h to be of the order of a few $100\,\text{GeV}$, the previous expectation implies that the scale of the new physics phenomena should be about $\Lambda \leq 1\,\text{TeV}$. Similarly, it has been shown that in case the Higgs boson is not a fundamental scalar field, its composite structure requires the new physics phenomena at the energy scale of electroweak interactions [67]. For all these reasons, the naturalness is considered to be one of the most robust motivations to expect the physics beyond the SM at an energy scale that is accessible to the contemporary and near-future accelerator-based experiments.

5.2.2 Unification of gauge couplings

The SM predictions are consistent with the observed properties of practically all known elementary particles. The model also elegantly explains why some non-trivial phenomena, including the proton decay and the large flavor-changing neutral currents, have not been observed so far. Yet, the model contains 18 parameters whose values are obtained or constrained by experimental observations, but not explained on the basis of some more fundamental principles.

The total number of a priori undetermined parameters may be reduced in theories in which the symmetry of the SM, the G_{SM}, is extended to a larger unifying symmetry group. These classes of theories are motivated by the fact that the SM particle content fits perfectly into multiplets of $SU(5)$, $SO(10)$ and larger groups which include the G_{SM} group [68], thus offering a potential explanation for the observed assignment of particle quantum numbers.

A direct implication of the ideas of these classes of theories is that the gauge couplings of the SM should unify when extrapolated to higher energy scales via appropriate renormalisation group equations[69]. It is known that the gauge couplings do not unify at any scale according to the particle content and the Lagrangian of the SM. But, they do unify in various extensions of the SM which include additional interactions and particles. Together with the other motivations these considerations provide more hints for a possible physics beyond the Standard Model at the weak scale. Additionally, these considerations indirectly select some of the new theories and models as a particularly motivated possibility.

5.2.3 Cosmological evidences for the Dark Matter

During the last two decades, a standard cosmological model of the universe has emerged, providing a detailed specification of the main contributions to the matter and energy content of the universe [70]. A remarkable agreement of its predictions with a large set of astrophysical observations gives it strong empirical foundations [71, 72]. The presence of the dark matter is suggested by a plethora of astrophysical observations: gravitational lensing, the curves of the radial velocities of stars in galaxies, measurements of the cosmic microwave background (CMB), and maps of the large-scale structure of galaxies. Combining all of these indications, as well as the distance probes such as supernovae, the amount of matter content is found to be:

$$\Omega_B = 0.0462 \pm 0.0015 \tag{5.13}$$
$$\Omega_{DM} = 0.233 \pm 0.013 \tag{5.14}$$
$$\Omega_\Lambda = 0.725 \pm 0.016 \tag{5.15}$$

where Λ stands for the cosmological constant which is associated with a vacuum energy necessary to explain the observed accelerating expansion of the universe. Therefore, according to the standard cosmological model, the baryonic matter described by the SM constitutes only about 4% of the total energy and matter currently observable in the universe.

In addition to the determination of the dark matter abundance, the astrophysical observations have shown that the dark matter should be "cold", stable and "dark". This means that it was non-relativistic at the time of the structure formation and it stayed without significant electromagnetic interactions up to the present day. The latter effectively suggests the particles are at most weakly interacting with the other particles and between themselves.

5.3 Supersymmetric extension of the Standard Model

The **Su**per**Sy**mmetry (SUSY) is an extension of the Poincaré symmetry of space-time that postulates a symmetry between the fields which belong to different spin multiplets, and naturally groups them into the larger multiplets of this extended symmetry [73, 74, 75]. The transformations of the new symmetry group, called supersymmetry, naturally transform fermion fields into boson fields and vice versa. On the other side, all SM fields have values of quantum numbers and masses that prevent them from being supersymmetric partners of any other SM field. For this reason, the theoretical requirement for supersymmetry effectively translates into the necessity for additional SM fields which have not been observed so far. The direct consequence is that, if SUSY is a symmetry of nature, it must be a broken symmetry.

One of the important features of all extensions of the SM which incorporate Supersymmetry is that they address several open questions in the Standard Model, and in particular those discussed in the previous section. This is one of the main reasons why

SUSY is the most favoured extension of the SM.

In general, it is expected that a successful extension of the Standard Model will have to be able to provide the following features [76]:

- It should be a theory which effectively contains the Standard Model of particle physics and General Relativity as its perturbative low-energy limit.

- It should provide a "natural" explanation for the apparent hierarchy between the Planck scale and the scale of electroweak symmetry breaking.

- Any additional symmetry in the extended model must be spontaneously broken in order not to reintroduce the problem of naturalness.

- The vacuum expectation value should correspond to a small and positive cosmological constant which we observe today.

In the following sections, we will present a very brief summary of the minimal supersymmetric extension of the standard model, as a potential candidate for a theory that incorporates all the features listed above. We will present all the parameters of this model, the spectrum of its new fields, as well as how it fits into one of the most studied frameworks for the unification of interactions - the framework of minimal supergravity. In the last two sections of this chapter, we will present the phenomenology of the extended models at hadron colliders and characteristic signatures that could be used for their experimental confirmation or rejection. More extensive phenomenological reviews of Supersymmetry and various unification frameworks may be found in [76].

5.3.1 The Minimal Supersymmetric Standard Model

The minimal supersymmetric extension of the standard model (MSSM) is the supersymmetric model with minimal content of additional fields with respect to the standard model. In any SUSY model, all of the bosonic and fermionic fields from the same super-multiplet are grouped into one single object called chiral superfield. The interactions and masses of all particles are determined by their gauge transformation properties and by the appropriately defined analytic function of chiral superfields called superpotential W [73]. The role of W is analogous to the role of the Lagrangian in the non-supersymmetric renormalizable field theories.

The superpotential for the MSSM is:

$$W = \lambda_u H_u Q \bar{U} + \lambda_d H_d Q \bar{D} + \lambda_e H_d L \bar{E} - \mu H_u H_d \qquad (5.16)$$

where Q, U, D, L, and E are the SU(2) quark doublet, up-type quark singlet, down-type quark singlet, lepton doublet, and lepton singlet superfields, respectively, while the λ_x are the dimensionless Yukawa coupling parameters, 3×3 matrices in the fermion generation space. The μ term in (5.16) is the supersymmetric version of the Higgs boson mass term in the Standard Model, while H_u and H_d are two Higgs superfields. These two fields are needed because of the analytical constraints imposed on the superpotential by the structure of the SUSY [73].

The fermions and their scalar superpartners are arranged into muliplets with asymmetric chirality. This arrangement preserves the distinction between the left- and right-handed particles. The gauge bosons and their fermion superpartners are arranged to form gauge supermultiplets. It is a common convention that bosonic superpartners are given names with the prefix "s-" and fermionic superpartners are denoted by the suffix "-ino". Squarks and sleptons are collectively known as "sfermions" and the entire group of superpartner particles are commonly named "sparticles".

Table 5.2: Chiral and gauge supermultiplets in the Minimal Supersymmetric Standard Model. The spin-0 chiral fields are complex scalars, and the spin-1/2 chiral fields are left-handed two-component Weyl fermions.

Names	spin 0	spin 1/2	spin 1	$SU_C(3), SU_L(2), U_Y(1)$
squarks, quarks	$(\tilde{u}_L \tilde{d}_L)$	$(u_L d_L)$	-	$(\mathbf{3}, \mathbf{2}, +\frac{1}{6})$
	$\tilde{u}_R$	u_R	-	$(\mathbf{3}, \mathbf{1}, -\frac{2}{3})$
	$\tilde{d}_R$	d_R	-	$(\mathbf{3}, \mathbf{1}, +\frac{1}{3})$
sleptons, leptons	$(\tilde{\nu}_L \tilde{e}_L)$	$(\nu_L e_L)$	-	$(\mathbf{1}, \mathbf{2}, -\frac{1}{2})$
	$\tilde{e}_R$	e_R	-	$(\mathbf{1}, \mathbf{1}, \mathbf{1})$
Higgs, higgsinos	$(H_u^+ H_u^0)$	$(\tilde{H}_u^+ \tilde{H}_u^0)$	-	$(\mathbf{1}, \mathbf{2}, +\frac{1}{2})$
	$(H_d^0 H_d^-)$	$(\tilde{H}_d^0 \tilde{H}_d^-)$	-	$(\mathbf{1}, \mathbf{2}, -\frac{1}{2})$
wino, W boson	-	$\tilde{W}^\pm \tilde{W}^0$	$W^\pm W^0$	$(\mathbf{1}, \mathbf{3}, \mathbf{0})$
bino, B boson	-	$\tilde{B}^0$	B^0	$(\mathbf{1}, \mathbf{1}, \mathbf{0})$
gluino, gluon	-	$\tilde{g}$	g	$(\mathbf{8}, \mathbf{1}, \mathbf{0})$

In this framework, the Yukawa matrices determine the masses and the mixing angles of the ordinary quarks and leptons, after the neutral scalar components of H_u and H_d obtain non-vanishing v.e.v.s. Since the top quark, bottom quark and tau lepton are the heaviest fermions in the SM, it is common to make the approximation that only the 3rd generation components of each Yukawa matrix are relevant.

The Higgs boson sector itself consists of eight degrees of freedom. After the neutral scalar components of H_u and H_d obtain non-vanishing v.e.v.s, three of these give rise to massive W and Z bosons, but the other five remain and form the physical MSSM Higgs bosons with spin 0: h^0, H^0, A^0, $H^\pm$.

The remaining supersymmetric particle content of the MSSM consists of four neutral colourless gauginos (spin 1/2), four charged colourless gauginos (spin 1/2), nine sleptons (spin 0), 12 squarks (spin 0) and eight gluinos (spin 1/2). Table 5.2 summarizes the chiral and gauge supermultiplets in the MSSM, including the SM fields. The grouping of particles into supermultiplets indicates their common gauge transformation properties. Additionally, all the states with the same quantum numbers may mix, and physical mass eigenstates are in general superpositions of the gauge interaction eigenstates.

In addition to the previous particle content, most SUSY extensions of the Standard Model include the supersymmetric partner of the graviton, commonly named gravitino

(spin 3/2). Although not technically required, it is an interesting possibility since it offers an appealing way for the description of gravity by requiring that the supersymmetry is a local symmetry. For this reason, gravitino is naturally present if the SUSY should play a main role in the unification of the SM with gravity.

Table 5.3: Summary of the hypothetical new particles in the Minimal Supersymmetric Standard Model (in case of the negligible sfermion mixing for the first two families).

Names	spin	R-parity	gauge eigenstates	mass eigenstates
Higgs bosons	0	+1	$H_u^0 \ H_d^0 \ H_u^+ \ H_d$	$h^0 \ H^0 \ A^0 \ H^\pm$
squarks	0	-1	$\tilde{u}_L \ \tilde{u}_R \ \tilde{d}_L \ \tilde{d}_R$	(same)
	0	-1	$\tilde{s}_L \ \tilde{s}_R \ \tilde{c}_L \ \tilde{c}_R$	(same)
	0	-1	$\tilde{t}_L \ \tilde{t}_R \ \tilde{b}_L \ \tilde{b}_R$	$\tilde{t}_1 \ \tilde{t}_2 \ \tilde{b}_1 \ \tilde{b}_2$
sleptons	0	-1	$\tilde{e}_L \ \tilde{e}_R \ \tilde{\nu}_e$	(same)
	0	-1	$\tilde{\mu}_L \ \tilde{\mu}_R \ \tilde{\nu}_\mu$	(same)
	0	-1	$\tilde{\tau}_L \ \tilde{\tau}_R \ \tilde{\nu}_\tau$	$\tilde{\tau}_1 \ \tilde{\tau}_2 \ \tilde{\nu}_\tau$
neutralinos	$\frac{1}{2}$	-1	$\tilde{B}^0 \ \tilde{W}^0 \ \tilde{H}_u^0 \ \tilde{H}_d^0$	$\tilde{\chi}_1^0 \ \tilde{\chi}_2^0 \ \tilde{\chi}_3^0 \ \tilde{\chi}_4^0$
charginos	$\frac{1}{2}$	-1	$\tilde{W}^\pm \ \tilde{H}_u^+ \ \tilde{H}_d^-$	$\tilde{\chi}_1^\pm \ \tilde{\chi}_2^\pm$
gluino	$\frac{1}{2}$	-1	$\tilde{g}$	(same)

At the beginning of this section it was shown that, if supersymmetry is indeed one of the symmetries of nature, it must be a broken symmetry. Although many different superpotential terms could be added to break SUSY, only a subset of them is allowed if the SUSY is required to solve the problem of naturalness and of the gauge hierarchy [?]. These terms are commonly named as the "soft" SUSY-breaking terms, and they Lagrangian terms with mass dimension 3 and below [73, 74]. In the case of the MSSM, these terms are:

$$
\begin{aligned}
\mathcal{L}_{soft}^{MSSM} = \quad & m_{\tilde{Q}}^2 |\tilde{Q}|^2 + m_{\tilde{U}}^2 |\tilde{U}|^2 + m_{\tilde{D}}^2 |\tilde{D}|^2 + m_{\tilde{L}}^2 |\tilde{L}|^2 + m_{\tilde{E}}^2 |\tilde{E}|^2 + \\
& + \frac{1}{2} \left(M_3 \tilde{g}\tilde{g} + M_2 \tilde{W}\tilde{W} + M_1 \tilde{B}\tilde{B} \right) + \\
& + m_{\tilde{H}_u}^2 |\tilde{H}_u|^2 + m_{\tilde{H}_d}^2 |\tilde{H}_d|^2
\end{aligned}
\tag{5.17}
$$

and effectively represent unknown parameters of the model which correspond to masses of sfermions ("m-terms"), masses of gauginos ("M-terms"), Higgs boson couplings, and trilinear scalar couplings ("A-terms"). The expression (5.17) is the most general soft supersymmetry breaking Lagrangian that is compatible with the gauge invariance in the MSSM.

In addition to the parameters above, there are two other important parameters: the

μ parameter, which enters in the mass terms in equation (5.17), and

$$\tan \beta \equiv \frac{\langle H_u^0 \rangle}{\langle H_d^0 \rangle} \tag{5.18}$$

which parameterizes how the SM Higgs vacuum expectation value is distributed between the two neutral Higgs scalars.

The mechanism by which soft SUSY breaking can be realised in nature has been the focus of an extensive theoretical work over several decades, and is nicely summarised in Refs [76]. While many of the details are beyond the scope of this work, it is worth mentioning that in its most generic form, soft SUSY breaking introduces 110 new parameters to the theory, none of which have counterparts in the Standard Model. These parameters take the form of 30 masses, 41 phases and 39 mixing angles [76]. Thus, in principle, the requirement of supersymmetry breaking appears to introduce a tremendous arbitrariness in the Lagrangian, contrary to the original motivation of the supersymmetry itself.

The presence of soft SUSY breaking terms additionally modifies the mixing of the sparticles of the MSSM. The particular details of the mixing is in general model-dependent. The gauge eigenstates of fermion super-partners of the third generation (i.e., $\tilde{t}_L$, $\tilde{t}_R$, $\tilde{b}_L$, $\tilde{b}_R$, $\tilde{\tau}_R$, $\tilde{\tau}_R$) are particularly prone to mixing due to their large Yukawa couplings. Additionally, the neutral higgsinos ($\tilde{H}_u^0$ and $\tilde{H}_d^0$) and the neutral electroweak gauginos ($\tilde{B}^0$ and $\tilde{W}^0$) mix to form four mass eigenstates commonly named neutralinos. These are denoted as $\tilde{\chi}_i^0$ (where i = 1,2,3,4). The charged higgsinos ($\tilde{H}_u^+$ and $\tilde{H}_d^-$) and the winos ($\tilde{W}^\pm$) mix to form two mass eigenstates called charginos. These are denoted as $\tilde{\chi}_i^\pm$ (where i = 1,2). The summary of the mass eigenstates of the MSSM is given in Table 5.3.

5.3.2 Direct implications of the MSSM

In case that the SUSY is realised in nature, equation (5.12) is incomplete and needs to include contributions from the scalar superpartners of the respective fermions. It can be shown that the contributions from the fields which follow different spin-statistics carry different algebraic signs. Furthermore, if supersymmetry is exact, the Yukawa couplings are identical between superpartners and the fact that the spins are different by a half-integer amount directly leads to the cancellation of these contributions. The direct consequence of this feature it that by mitigating the quadratically divergent corrections to the Higgs mass, the supersymmetry makes the Standard Model a more natural theory.

We have discussed at the beginning of this chapter that the conserved quantities known as baryon number and lepton number are consequences of the accidental global symmetries in the Standard Model. In the context of the MSSM, it is convenient and instructive to directly enforce this symmetry by postulating a conserved quantum number called the R-parity, defined as

$$P_R = (-1)^{3(B-L)+2s} \tag{5.19}$$
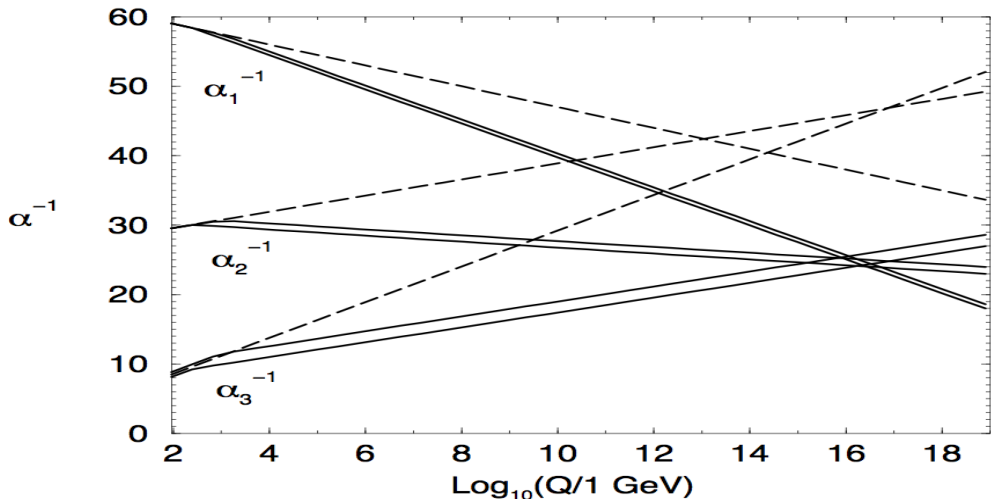
where s refers to the spin quantum number, and ensures that particles within the same

supermultiplet have different R-parities. Standard Model particles are thus endowed with even R-parity ($P_R = +1$) while squarks, sleptons, gauginos, and higgsinos are endowed with odd R-parity ($P_R = -1$). If R-parity proves to be a conserved quantum number in nature, which is both theoretically and experimentally well-motivated, its direct consequences are [73]:

- the sparticle with the lowest mass, commonly called the lightest supersymmetric particle or the LSP, is stable and does not decay. If the LSP does not carry an electromagnetic charge it only couples weakly to ordinary matter. In this case the LSP would be a candidate for dark-matter;

- in all interactions the sparticles must be produced in pairs in order to conserve P_R;

- each sparticle can decay to an odd number of lighter sparticles. Subsequent sparticle decays will occur until a stable LSP has been produced.

In general, the enforcement of R-parity is well-motivated phenomenologically by proton decay constraints and the hope that the LSP will provide a good dark matter candidate. However, the conservation of the R-parity has other important phenomenological consequences and they are especially related to search strategies for experimental evidence of the supersymmetry at colliders. A detailed discussion on this topic will be presented in the next section.
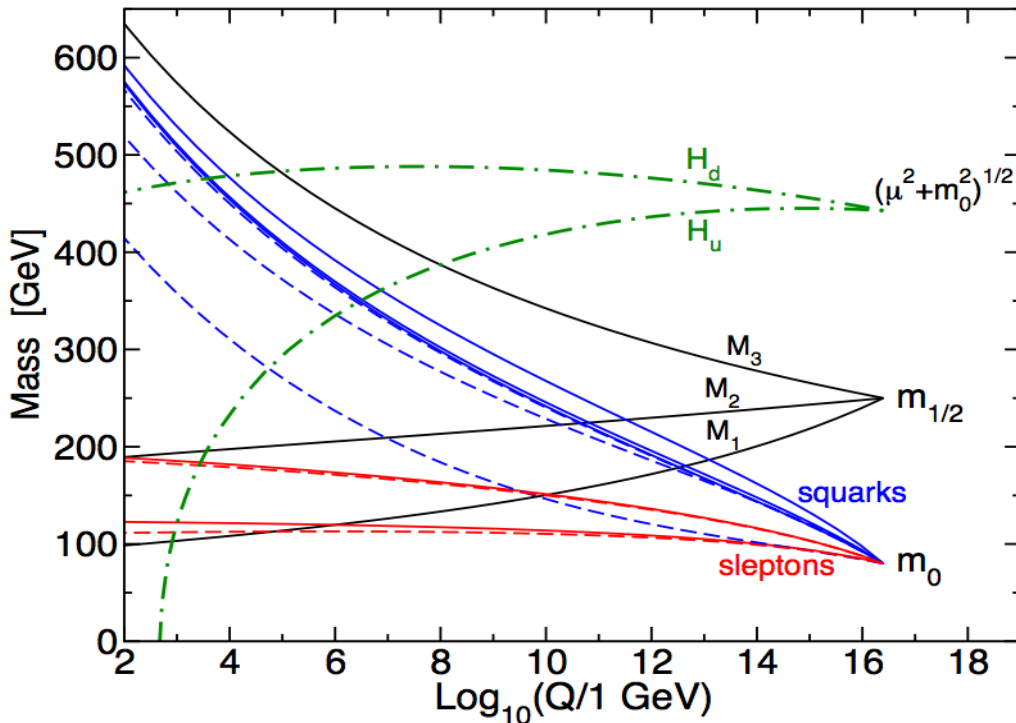
Figure 5.1: The renormalisation group evolution of the inverse gauge couplings in the Standard Model (dashed lines) and in the MSSM (solid lines). Two-loop effects are included in the renormalisation group equations, while the widths represent the unknown mass threshold for the sparticles and theoretical uncertainties [76].

Another implication of the MSSM is that the additional sparticle fields contribute to loop diagrams in such a way that the effective gauge couplings unite at some common value near the scale of $O(10^{16}\,\text{GeV})$. The effect is shown graphically in Figure 5.1 [76],

where the inverses of the three gauge couplings, including two-loop effects, are plotted against the energy scale in the two models. It can be seen in the figure that, unlike the Standard Model, the MSSM has the right particle content to ensure that the gauge couplings can unify. While the apparent unification of gauge couplings at this scale might just be accidental, it may also be taken as a strong hint in favour of SUSY being a more fundamental grand unified theory and is definitely a very encouraging evidence.

5.4   Phenomenology of the constrained MSSM

The MSSM as a supersymmetric model with soft symmetry breaking has many attractive features. It provides an elegant mechanism for stabilizing the gauge hierarchy with respect to the effects of radiative corrections, a natural weakly-interacting dark matter (DM) candidate, facilitates the gauge coupling unification and predicts the existence of a light Higgs boson.

Figure 5.2: Renormalisation group evolution of scalar and gaugino mass parameters in the constraned MSSM with typical mSUGRA boundary conditions imposed at the energy of 2.5×10^{16} GeV. The electroweak symmetry breaking is triggered as the parameter $\mu^2 + m_{H_u}^2$ becomes negative [76].

On the other hand, SUSY has to be "softly" broken in order to make contact with reality, which introduces even in the general MSSM a large number of new free parameters. In particular, there are in total 110 free parameters introduced by the most generic soft

SUSY breaking mechanism which completely diminish the predictive power of the MSSM. For this reason, in order to explore the variations of the MSSM, one often imposes artificial boundary conditions on the SUSY soft-breaking parameters at the GUT scale. There are several unification frameworks that reduce this vast parameter space to a much more tractable subspace. A large reduction can already be achieved by making modest assumptions about parameters which yield flavour-changing interactions. Strict experimental constraints can be used to eliminate several terms from the soft SUSY breaking component of the Lagrangian. These experimental measurements relate mixings of the neutral K, D, and B meson systems as well as the decay rate of $\mu \to e\gamma$. By imposing these constraints, one finds that the subset of parameters can be reduced to:

- three gaugino masses M_1, M_2, M_3, which relate to the bino, wino, and gluino respectively;

- five squark and slepton mass-squared parameters $m_{\tilde{Q}}^2$, $m_{\tilde{U}}^2$, $m_{\tilde{D}}^2$, $m_{\tilde{L}}^2$, $m_{\tilde{E}}^2$, which relate to the left-handed squarks, left-handed sleptons, right-handed up-type squarks, right-handed down-type squarks, and right-handed charged sleptons respectively;

- three trilinear couplings A_0^u, A_0^d, A_0^e which couple the left-handed and right-handed up-type squarks, the left-handed and right-handed down-type squarks, and the left-handed and right-handed charged sleptons to their respective Higgs fields. These parameters have dimensions of energy;

- four parameters from the Higgs potential $m_{H_u}^2$, $m_{H_d}^2$, $\tan\beta$, and $\mathrm{sign}(\mu)$ which represent the mass-squared terms of the up- and down-type Higgs field, the ratio of the two Higgs v.e.v., as well as the algebraic sign of the μ coefficient.

The scheme of the reduction of parameters presented above is commonly referred to as the phenomenological MSSM (pMSSM) and leaves in total 15 undetermined parameters. In addition to the assumptions made in this scheme, there are several other simplifications that can be made in order to reduce the number of parameters even further. Namely, the mass-related parameters and couplings listed above scale with the energy transfer, so it is natural to impose some boundary conditions on them for example at the Planck or the unification scale. One possible set of these boundary conditions imposes the relationships between the parameters at the GUT scale so that the gaugino soft masses unify to a common value $m_{1/2}$, the soft-breaking masses of all the sfermions and Higgs doublets unify to common value m_0, while tri-linear soft-breaking parameters have another common value A_0:
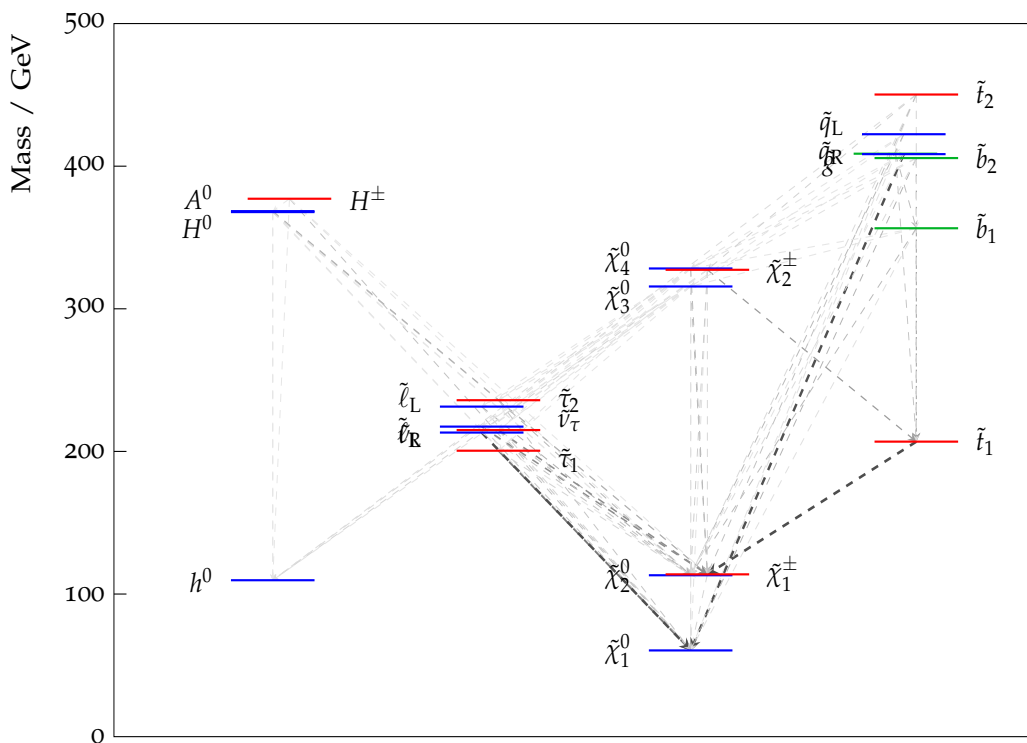
$$M_3 = M_2 = M_1 = m_{1/2} \qquad (5.20)$$

$$m_{\tilde{Q}}^2 = m_{\tilde{L}}^2 = m_{\tilde{u}}^2 = m_{\tilde{d}}^2 = m_{\tilde{e}}^2 = m_{H_u}^2 = m_{H_d}^2 = m_0 \qquad (5.21)$$

$$A_0^u = A_0^d = A_0^e = A_0 \qquad (5.22)$$

In this scheme, named constrained MSSM (cMSSM), the model is completely determined by these four continuous and one discrete parameters: $m_{1/2}$, m_0, A_0, $\tan\beta$, $\mathrm{sign}(\mu)$.

From these boundary conditions at the GUT scale, one can determine using the renormalization group equations of this model [73] the other fifteen parameters at the TeV scale which are of particular interest to experimentalists searching for supersymmetry at modern collider experiments. Additional assumptions may be imposed between the trilinear and bilinear soft-breaking parameters and the universal scalar mass, which effectively fix the value of $\tan\beta$ by the radiative electroweak symmetry breaking conditions at the EW scale [73]. In the same way, the gravitino mass $m_{3/2}$ is fixed to be equal to the common scalar mass $m_{3/2} = m_0$.

Figure 5.3: The mass spectrum and branching ratios for the decay modes of sparticles for values of cMSSM parameters: $m_0 = 200, m_{1/2} = 160, \tan(\beta) = 10, A_0 = -400, \mu > 0$ (the "LM_0" benchmark point). Mass spectrum and decay modes are calculated using SOFTSUSY 2.0.17, SDECAY 1.2 and HDECAY 3.302.

The framework which imposes this additional set of boundary conditions is known as the minimal supergravity model or the mSUGRA. Although several other boundary conditions exist, the mSUGRA scenario yields a rich, but tractable, parameter space which provides a good playground for physicists to study the phenomenological consequences of supersymmetry. One example of renormalisation group evolution of scalar and gaugino mass parameters in the constraned MSSM is shown in Figure 5.2.

In a supersymmetry scenario with mSUGRA-inspred boundary conditions, the mass parameters of the respective gauginos at TeV energy scales to a good approximation can

be described by the following relation [76]:

$$M_3 \; : \; M_2 \; : \; M_1 \approx 6 \; : \; 2 \; : \; 1 \qquad (5.23)$$

For this reason, the gluino is expected to be a few times heavier than the neutralinos and charginos. This result can be mostly attributed to stronger effects of the QCD coupling when compared to the electroweak couplings at the TeV scale. For the same reason, squarks are generally expected to be heavier than sleptons. Owing to the interactions induced by the weak coupling, left super-partners are expected to be heavier than right super-partners in the first and second generations.
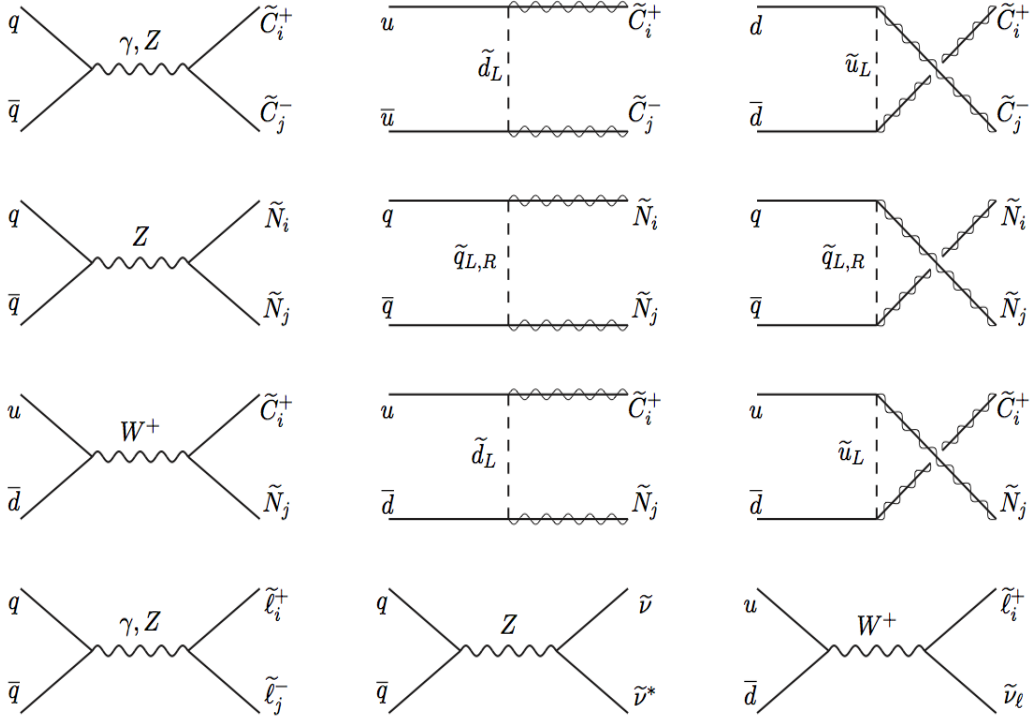
The left and right gauge eigenstates of the third generation undergo a non-trivial amount of mixing as described in detail [76]. In several scenarios, this mixing leads to one of the two mass eigenstates being lighter than those in the first and second generations, while leaving the other mass eigenstate significantly heavier. The lightest slepton is likely to be the $\tilde{\tau}_1$, while the lightest squark is expected to be either $\tilde{t}_1$ or $\tilde{b}_1$. The lightest of the 5 Higgs particles is expected to be the h_0 with a mass under roughly 130 GeV, and the other Higgs particles could be significantly heavier. One example of the mass spectrum and branching ratios for the decay modes of sparticles for typical cMSSM parameters is given in Figure 5.3. This mass spectrum and branching ratios for the decay modes of sparticles correspond to the values of parameters: $m_0 = 200, m_{1/2} = 160, \tan(\beta) = 10, A_0 = -400, \mu > 0$. This set of parameters is commonly referred to as the "LM_0" benchmark point.

5.4.1 Sparticle production in hadron collisions

The many years of effort to understand and discover the supersymmetry could come true at the LHC. As it has been discussed in the previous sections, in the case that the supersymmetry is the solution to the open questions in the Standard Model, there is a possibility that several super-partners might be discovered by the experiments operating at LHC. The following sections will discuss some of the general experimental signatures of supersymmetry in the hadron collider environment. These experimental signatures are the main motivation for the strategy adopted in the last chapter, which describes one of the first searches for supersymmetry performed with high-energy collision data at the LHC in the year 2010. Some of the motivating factors are inspired by various assumptions made in the construction of the mSUGRA model, while others are quite model independent.

The hard-interactions in the proton-proton collisions at the LHC are expected to primarily involve particles which carry colour charge and whose strong interactions are described by the quantum field theory QCD. This fact directly influences both the initial and the final states which should be considered at the LHC. In this section we will consider only the simplest scenario with two incoming particles and two outgoing particles.

All the sparticles in the final state can be produced in pairs from collisions of partons

Figure 5.4: Feynman diagrams for electroweak production of sparticles at hadron colliders from quark-antiquark annihilation.

which interact via electroweak interaction:

$$q\bar{q} \to \tilde{\chi}_i^+ \tilde{\chi}_j^-, \ \tilde{\chi}_i^0 \tilde{\chi}_j^0, \quad u\bar{d} \to \tilde{\chi}_i^+ \tilde{\chi}_j^0, \quad d\bar{u} \to \tilde{\chi}_i^- \tilde{\chi}_j^0 \tag{5.24}$$

$$q\bar{q} \to \tilde{l}_i^+ \tilde{l}_j^-, \ \tilde{\nu}_l \tilde{\nu}_l^*, \quad u\bar{d} \to \tilde{l}_L^+ \tilde{\nu}l, \quad d\bar{u} \to \tilde{l}_L^- \tilde{\nu}_l^* \tag{5.25}$$

as shown in Figure 5.4, or via strong interaction:

$$gg \to \tilde{g}\tilde{g}, \ \tilde{q}_i \tilde{q}_j \tag{5.26}$$
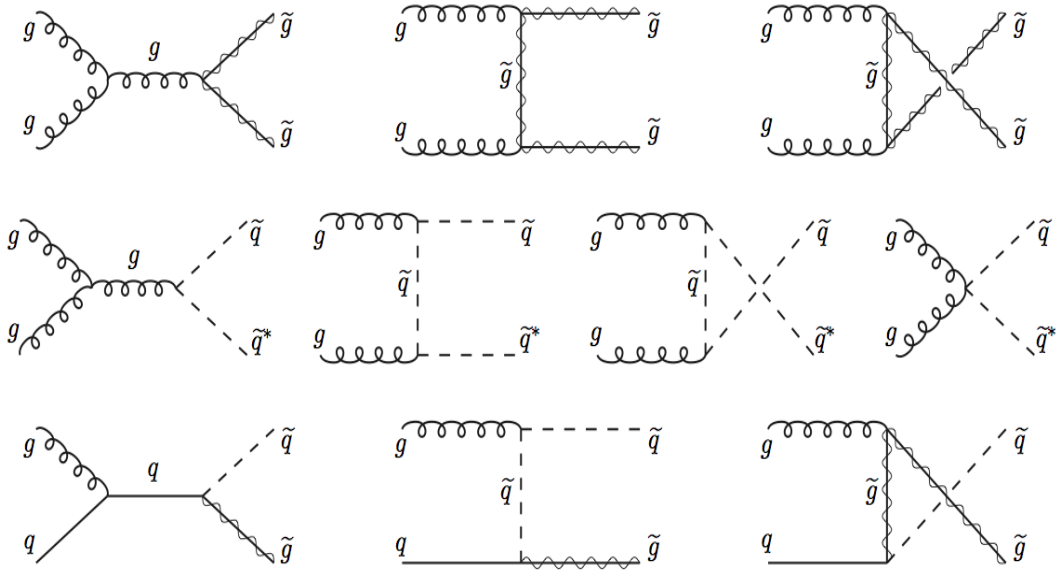
$$gq \to \tilde{g}\tilde{q}_i \tag{5.27}$$

$$q\bar{q} \to \tilde{g}\tilde{g}, \ \tilde{q}_i \tilde{q}_j \tag{5.28}$$

$$qq \to \tilde{q}_i \tilde{q}_j \tag{5.29}$$

as shown in Figure 5.5. The reactions in (5.25) also get contributions from electroweak vector bosons in the s-channel, as well as squark-exchange contributions in the t-channel that are negligible in most of the models. On the other hand, the processes in (5.29) also get contributions from the t-channel exchange of an appropriate squark or gluino, as well as gluon s-channel contributions.

In the first approximation one may think of the LHC as a gluon-gluon and gluon-quark collider, although the possible final states are always an inclusive combination

Figure 5.5: Feynman diagrams for gluino and squark production at hadron colliders from gluon-gluon and gluon-quark fusion.

of the results of parton collisions of all types. In practice, the production of gluinos and squarks at the LHC is usually dominated by gluon-gluon and gluon-quark fusion, unless the gluinos and squarks are heavier than 1 TeV [77]. One can also have associated production of a chargino or neutralino together with a squark or gluino, but most models predict that the corresponding cross-sections are much lower than for the ones in (5.25) and (5.29). On the other hand, slepton pair production may occur according to (5.25) and it also may be observable at the LHC. The cross-sections for sparticle production at hadron colliders have been incorporated in several computer programs including [78].
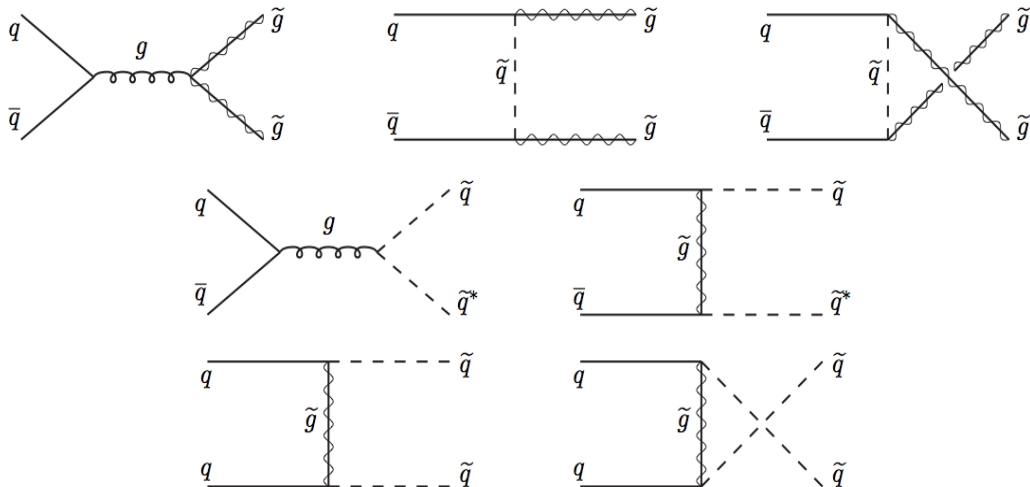
It is important to understand that not all of the diagrams presented above contribute equally to the production of final states with a given type of supersymmetric particles. Depending on the mass hierarchy between the gluino and the squarks, some diagrams might dominate over the others. If one assumes that the squark masses are roughly degenerate, then the following three scenarios should be considered:

- $m_{\tilde{g}} > m_{\tilde{q}}$: in this case diagrams which include the production of two squarks, either via annihilation of the initial states into a gluon or by the exchange of a virtual squark, will dominate. These include diagrams shown in Figure 5.6. The interaction produces two final-state squarks, but requires the exchange of a gluino which is taken to be heavy in this scenario. In this case, the processes involving the exchange of heavy particles are extremely suppressed;

- $m_{\tilde{g}} < m_{\tilde{q}}$: in this case diagrams which include the production of two gluinos, either via annihilation of the initial states into a gluon or by the exchange of a virtual gluino, will dominate. These include diagrams shown in Figure 5.6. The diagram yields two final-state gluinos but requires the exchange of a virtual squark, which is

assumed to be heavy in this scenario and is therefore suppressed;

- $m_{\tilde{g}} \sim m_{\tilde{q}}$: in this case all diagrams in Figure 5.6 will have non-trivial contributions. Particularly, contributions from diagrams with a squark and a gluino in the final state will be enhanced, as in Figures 5.6 and 5.5.

The discussion and conclusions expressed here are valid only if all the involved masses are within the range accessible by the collider. In the case that the squarks and gluinos are too heavy to be produced, then the greater strength of the strong QCD coupling will be irrelevant, and the incoming partons will be forced to directly produce lighter superpartners via the electroweak interaction. This will involve diagrams like the ones in Figure 5.4, which directly yield neutralinos and charginos. The role of these diagrams may be negligible or significant depending on the mass spectrum of the coloured superpartners.

Figure 5.6: Feynman diagrams for gluino and squark production at hadron colliders from strong quark-antiquark annihilation and quark-quark scattering.

Phenomenological consequences between strong and electroweak SUSY production are significantly different. The former involves heavy coloured particles, which must decay to Standard Model coloured particles which will in turn hadronize and become a jet of particles. Furthermore, the multiplicity of jets produced in the event will be largely dependent on whether or not gluinos are produced. Indeed, if a gluino is produced, it must decay to a quark and squark (i.e., $\tilde{g} \to q\tilde{q}$). On the other hand, the squark, which will likely be off-shell, will also decay to a quark and one of the lighter gauginos (i.e., $\tilde{q} \to q\tilde{G}$). In the case that squarks are lighter than gluinos, the production and subsequent cascade decay will begin with the squark and will only yield one jet before decaying to a gaugino.

The previous considerations largely follow from the conservation of R-parity in the MSSM which dictates that super-partners have to be produced in pairs. In general, it can be concluded that in the case of conserved R-parity, the following is expected to hold:

- processes where $\tilde{g}\tilde{g}$ pairs are produced will result in at least 4 hadronic jets;

- processes where $\tilde{g}\tilde{q}$ pairs are produced will result in at least 3 hadronic jets;

- processes where $\tilde{q}\tilde{q}$ pairs are produced will result in at least 2 hadronic jets.

In practice, the final state gluon radiation of the outgoing partons or initial state gluon radiation of the incoming partons might give rise to more jets in the event. For all these reasons, the searches for SUSY in the hadron collisions typically rely on the signature of multiple high-energy jets. In order to characterize the total amount of hadronic jet activity in a collision event independently of the jet multiplicity, it is common to construct a variable that sums the scalar transverse momenta of all of the jets. Typically, this variable is denoted as H_T, and can provide a useful distinction between events that feature coloured production and those that do not.

5.4.2   Sparticle decays

It has been discussed in the previous section that the decay patterns of sparticles are dictated by the Lagrangian terms of the MSSM, and in particular by the conservation of R-parity. In several variations of the MSSM the lightest neutralino $\tilde{\chi}_1^0$ is the LSP and all decay chains of sparticles end up with this neutralino in the final state. In this section we will consider briefly the possible decays of produced neutralinos, charginos, sleptons, squarks and gluinos.

The first class of important decays are the two-body decays of neutralinos and charginos. In the previous section we have briefly explained that each neutralino and chargino contains at least a small admixture of the electroweak gauginos and therefore inherits couplings of weak interaction strength to scalar-fermion pairs. If sleptons or squarks are sufficiently light, a neutralino or chargino can therefore decay into lepton-slepton or quark-squark pairs. In case sleptons are lighter than squarks, the final states with lepton-slepton pairs will be favoured. A neutralino or chargino may also decay into any lighter neutralino or chargino plus a Higgs scalar or an electroweak gauge boson, because they inherit the gaugino-higgsino-Higgs and gaugino-gaugino-vector boson couplings of their components. Thus, the possible two-body decay modes for neutralinos and charginos in the MSSM are:

$$\tilde{\chi}_i^0 \to Z\tilde{\chi}_j^0,\ W\tilde{\chi}_j^\pm,\ h^0\tilde{\chi}_j^0,\ l\tilde{l},\ \nu\tilde{\nu} \tag{5.30}$$

$$\tilde{\chi}_i^\pm \to W\tilde{\chi}_j^0,\ Z\tilde{\chi}_1^\pm,\ h^0\tilde{\chi}_1^\pm,\ l\tilde{\nu},\ \nu\tilde{l} \tag{5.31}$$

where ν, l and q denote neutrinos, charged leptons and quarks, respectively. In the case of the heavy neutralinos and chargino, one or more of the two-body decays in equations (5.30) and (5.31) are likely to be kinematically allowed.

The second class of important decays are the three-body decays of neutralinos and charginos. This type of decays is especially important in cases where all of the two-body decay modes are kinematically forbidden for given properties of charginos and neutralinos. In that case, charginos and neutralinos may undergo three-body decays

$$\tilde{\chi}_i^0 \to f f \tilde{\chi}_j^0,\ \tilde{\chi}_i^0 \to f f' \tilde{\chi}_j^\pm,\ \tilde{\chi}_i^\pm \to f f' \tilde{\chi}_j^0,\ \tilde{\chi}_2^\pm \to f f \tilde{\chi}_1^\pm \tag{5.32}$$

through the same, but now off-shell, gauge bosons, Higgs scalars and leptons that appeared in the two-body decays equations (5.30) and (5.31). The chargino and neutralino decay widths concerning the various final states can be found in [73].

The third class are two-body decays of slepton. Thanks to their gaugino mixture, sleptons can have two-body decays into a lepton and a chargino or neutralino. Therefore, the two-body decays

$$\tilde{l} \to l\tilde{\chi}_i^0, \ \tilde{l}^\pm \to \nu\tilde{\chi}_i^\pm, \ \tilde{\nu} \to l\tilde{\chi}_i^0, \ \tilde{\nu} \to \nu\tilde{\chi}_i^0 \tag{5.33}$$

can be of weak interaction strength. In particular, the direct decays

$$\tilde{l} \to l\tilde{\chi}_1^0, \ \tilde{\nu} \to l\tilde{\chi}_1^0 \tag{5.34}$$

are expected to be practically always kinematically allowed, in the case the lightest neutralino is the LSP. However, if the sleptons are sufficiently heavy, then the two-body decays

$$\tilde{l} \to l\tilde{\chi}_2^0, \ \tilde{l}^\pm \to \nu\tilde{\chi}_1^\pm, \ \tilde{\nu} \to l\tilde{\chi}_2^0, \ \tilde{\nu} \to \nu\tilde{\chi}_1^0 \tag{5.35}$$

can also be important. The right-handed sleptons do not couple to the $SU(2)_L$ gauginos, so they typically prefer the direct decay. In contrast, the left-handed sleptons may prefer to decay as in equation (5.35) rather than the direct decays to the LSP as in equation (5.34), if the former is kinematically allowed.

The final class of important decays are squark and gluino decays. In this case, whenever the decay of a squark to a pair quark-gluino is kinematically allowed, it will dominate, because the quark-squark-gluino vertex has QCD strength. Otherwise, the squarks will decay into a quark plus neutralino or chargino. The direct decay to the LSP is always kinematically favoured, and for right-handed squarks it can dominate. On the other side, squark decays to higgsino-like charginos and neutralinos are less important, except in the cases of stops and sbottoms, which have significant Yukawa couplings.
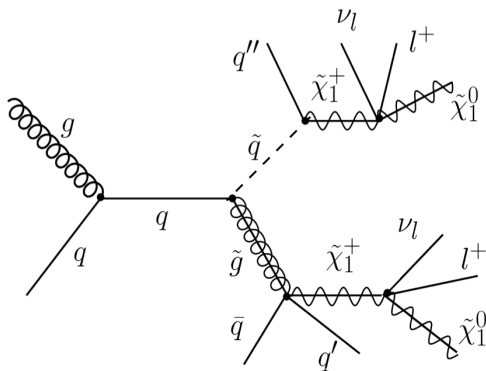
The decay of the gluino can only proceed through a squark, either on-shell or virtual. If two-body decays are allowed, they will dominate, again because the relevant gluino-quark-squark coupling has QCD strength. The simplest gluino decays can have two, one or no charged leptons in addition to two or more hadronic jets in the final state. An important feature is that when there is exactly one charged lepton, it can have charge of either sign with equal probability. This follows from the fact that the gluino does not couple electroweakly. Consequently, the production of lepton pairs with the same sign is as plausible as the production of lepton pairs with the opposite sign.

5.5 Same-sign lepton pairs in models beyond the SM

5.5.1 Same-sign lepton pairs in the MSSM

Some of the most important signatures in the analyses of physics processes at hadron colliders are the final states with one lepton, and especially with two or more leptons. First, it is a clear indication that an electroweak process has occurred in the interaction that have coloured particles in initial states. Second, leptons are typically less problematic to detect in the hadronic environment and their properties can be well measured.

A particularly interesting leptonic signature of the SUSY production is the event with a pair of leptons (di-leptons) in the final state, where the two leptons carry the same electromagnetic charge. An example of such an event is shown in Figure 5.7. This process involves the production of a gluino and left-handed squark, which each give rise to a cascade decay of Standard Model particles. Each of the three quarks ($\bar{q}$, q', q'') produced in the cascade will be detected as jets. The two leptons (l^+l^+) can be from the same or from different generation and will have the same electromagnetic charge. In average, these leptons will be detected in the experiment as objects that are well isolated from the other objects in the final state of the decay. The neutrinos ($\nu\nu$) as well as the LSPs ($\tilde{\chi}_1^0\tilde{\chi}_1^0$) will not interact with the detector and will contribute to a significant amount of missing energy and momentum imbalance in the event. While Figure 5.7 is a typical example of a SUSY event which yields a pair of same-sign di-leptons, there are many more scenarios which potentially may result in a event with a similar topology.

Figure 5.7: An example of strong production of supersymmetric particles and a decay chain featuring a pair of same-sign leptons in the final state.

In addition to these unique characteristics of the events with same-sign di-leptons, the production of same-sign di-leptons is greatly suppressed in the Standard Model. For all these reasons, the event signatures with a pair of same-sign leptons, several energetic jets, and significant amount of missing energy is one of the most promising ways of discovering the supersymmetry.

5.5.2 Same-sign lepton pairs in other extensions of the SM

In the previous section we have explained that the production of pairs of same-sign leptons is significantly suppressed in the Standard Model, but that it can be naturally accommodated and realised in the the context of (R-Parity conserving) models of supersymmetry such as the MSSM. In addition to this, the final states of hadronic interactions with pair of same-sign leptons can also be featured in a variety of alternative extensions of the Standard Model. These extensions include a wide range of theories with fundamentally different features with respect to the supersymmetric models. Some of the examples are:

- theories with universal extra-dimensions [79];

- theories that predict the existence of heavy neutrinos of Majorana type [80];

- theories with a pair production of hypothetical fermionic partners of the top quark [81];

- theories that predict same-sign top-pair resonances in warped extra dimensions [82].

Because the production of pairs of same-sign leptons is significantly suppressed in the Standard Model, the important consequence is that the same-sign leptons signature can be used to discriminate between the SM and the MSSM, but also between the SM and many other extensions of the SM.

5.6 Existing experimental constraints

The number of undetermined parameter in the MSSM is enormous and practically untractable. However, a strong theoretical motivation and compelling experimental evidence justify many of the simplifying assumptions that were used to formulate the cMSSM model, which is fully defined with the specification of 5 parameters ($m_{1/2}$, m_0, A_0, $\tan(\beta)$, $\text{sign}(\mu)$). In addition to this, reduction of the parameter space has been achieved by a variety of results obtained in several experiments over the past few decades. In this section, we will present a brief summary of these experimental constraints, with a strong focus on models which conserve R-Parity and feature gaugino and scalar mass unification at the GUT scale, such as cMSSM. A thorough review of the constraints on supersymmetry can be found in [83, 84] and references therein.

In the last chapter, we will demonstrate how these experimental constraints are extended with the results of the physics analysis performed on the events with same sign leptons in the data collected with the CMS experiment in the year 2010.

5.6.1 Cosmological observations

The latest analysis of the Cosmic Microwave Background (CMB) data from the Wilkinson Microwave Anisotropy Probe (WMAP) shows that the density of baryonic matter in the universe is $\Omega_B h^2 = 0.0227 \pm 0.0006$, while the total density of matter in the universe is $\Omega_m h^2 = 0.133 \pm 0.006$ [71], where h is the Hubble constant that characterizes the expansion

of the universe. The matter density excess, i.e. $\Omega_{DM}h^2 = (\Omega_m h^2 - \Omega_b h^2) = 0.110 \pm 0.006$ is generally attributed to a cold dark matter substance. And, therefore, constraints can be placed on the parameter space of the MSSM such that the relic abundance of the LSP accounts for the observed dark matter, i.e., $\Omega_{\tilde{\chi}}h^2 \approx \Omega_{DM}h^2$.

In general, the interplay of the mSUGRA parameters and $\Omega_{\tilde{\chi}}$ is quite complex and this task is achieved by some generalisations. The cross-section for two thermal LSPs to annihilate (e.g., $\tilde{\chi}_1^0 \tilde{\chi}_1^0 \to f\bar{f}$) depends on the couplings and masses of the exchanged and final-state particles, and is assumed to be inversely proportional to the LSP relic density $\Omega_{\tilde{\chi}}$ [85]. In addition, it is assumed that the annihilation typically results in a fermion-antifermion pair and that more final states are available in case of higher mass of the LSP. After taking these assumptions into account, the requirement to get $\Omega_{\tilde{\chi}}$ in the correct range of values indirectly leads to the restriction of the values of m_0 and $m_{1/2}$ parameters. A detailed review and analysis of the viable regions can be found in [84].

5.6.2 Indirect measurements at low-energy experiments

An evidence of the existence of superpartners of the Standard Model particles could also be observed indirectly through their contributions in the radiative corrections of various processes and measurable observables. One such observable is the anomalous magnetic moment of the muon $a_\mu = (g-2)_\mu$ which has been evaluated to a very high accuracy in the Standard Model [86]. In particular, this observable could be affected by the quantum corrections that would arise from the presence of sparticles and their specific interactions.

The E821 experiment at the Brookhaven National Laboratory, which is now formally completed, has studied the precession of muons as they circulate around a storage ring under a constant magnetic field and measured a_μ to a very high precision. The experimental average value [87, 88] of

$$a_\mu^{exp} = (11659208.0 \pm 5.4 \pm 3.3) \times 10^{-10} \tag{5.36}$$

where the first uncertainty is statistical and the second is systematic, deviates by about 3.6σ from the Standard Model prediction $a_\mu^{SM} = (11659180.2 \pm 4.9_{TOT}) \times 10^{-10}$ [86]. Although the future development of this field and more accurate muon a_μ measurements are expected, and the results are still not definite, this difference could be attributed to an additional contribution of the superpartners in the radiative corrections and, hence, could accommodate a variety of SUSY models. In particular, the deviation of a_μ from the SM prediction by more than 3σ can be easily accommodated within the MSSM by choosing appropriately the sign of the Higgs supermultiplet mixing parameter [84].

Another process where the existence of new particles could be observed indirectly, is the decay of neutral B mesons to pairs of oppositely charged leptons. This type of process is allowed in the Standard Model only via second-order weak interactions, and is thus heavily suppressed. However, the radiative corrections that would arise from the presence of sparticles and their specific interactions could result in a detectable enhancement in the branching ratios for the $B_s^0 \to \mu^+\mu^-$ and $B_s^0 \to e^+e^-$ (or likewise for B^0). Precise

measurements of these branching ratios were carried out at the CDF and D0 experiments at the Tevatron collider and also at various B-factory experiments [88]. While none of the experiments had the sensitivity to confirm the Standard Model prediction of $BR(B_s^0 \to \mu^+\mu^-) = (3.42 \pm 0.54) \times 10^{-9}$, strict lower limits on the branching ratios of

$$BR(B_s^0 \to \mu^+\mu^-) < 4.7 \times 10^{-8}, \tag{5.37}$$

were placed and a portion of the previously allowed SUSY parameter space was excluded [84].

5.6.3 Direct searches at high-energy collider experiments
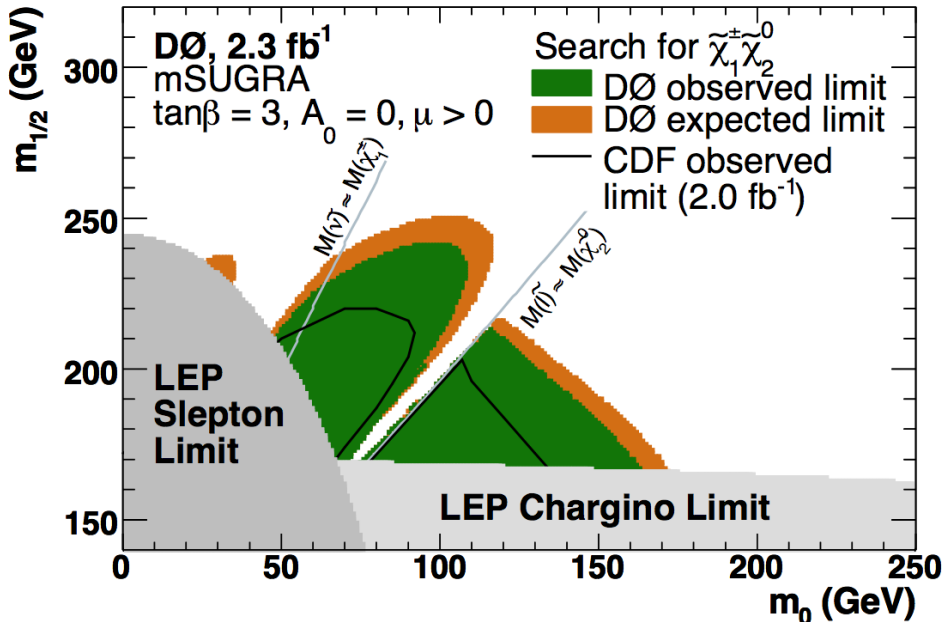
The most important direct searches for supersymmetric particles have been performed by the experiments at the LEP and Tevatron colliders. At LEP, where the center of mass energy has reached $209\,\mathrm{GeV}$, the dominant mechanism for sparticle production occurs via electroweak processes. In many supersymmetric models the LSP is predicted to be electrically neutral, which implies that direct searches are not really feasible. However, indirect limits have been placed on the mass of the LSP based on slepton, chargino, and Higgs searches.

At the Tevatron collider, where the center-of-mass energy was $1.96\,\mathrm{TeV}$, production of coloured particles is expected to dominate because the initial particles are coloured. In particular, searches involving associated chargino-neutralino production were performed. These searches exploited the same-sign di-lepton signature in order to reduce backgrounds and to set exclusion limits [89, 90].

Table 5.4: Lower limits on masses of the sparticles from the LEP experiments (ALEPH, OPAL, DELPHI, L3) and the Tevatron experiments (CDF, D0).

Particle	lower limit	comment
$\tilde{e}_{L,R}$	$107\,\mathrm{GeV}$	valid for all $m_{\tilde{e}_R} - m_{\tilde{\chi}_1^0}$
$\tilde{\mu}_{L,R}$	$94\,\mathrm{GeV}$	valid for $m_{\tilde{\mu}_R} - m_{\tilde{\chi}_1^0} > 10\,\mathrm{GeV}$, $1 \le \tan\beta \le 40$
$\tilde{\tau}_{L,R}$	$81.9\,\mathrm{GeV}$	valid for $m_{\tilde{\tau}_R} - m_{\tilde{\chi}_1^0} > 15\,\mathrm{GeV}$
$\tilde{\chi}_1^0$	$46\,\mathrm{GeV}$	valid for all $m_{\tilde{\chi}_2^0} - m_{\tilde{\chi}_1^0}$
$\tilde{\chi}_1^\pm$	$94\,\mathrm{GeV}$	valid for $m_{\tilde{\chi}_1^\pm} - m_{\tilde{\chi}_1^0} < 3\,\mathrm{GeV}$, $\tan\beta \le 40$
$\tilde{q}$	$379\,\mathrm{GeV}$	valid for any $m_{\tilde{g}}$
$\tilde{g}$	$308\,\mathrm{GeV}$	valid for any $m_{\tilde{q}}$

Table 5.4 summarizes the limits that were achieved by the ALEPH, OPAL, DELPHI and L3 experiments at LEP, as well as the CDF and D0 experiments at Tevatron. Many of the limits listed in this table rely on the assumption of sfermion and gaugino mass unification at the GUT scale. In many cases, the limits can be tightened if further assumptions are made about model parameters.

Figure 5.8: Exclusion limits from squarks and gluinos searches at the D0 experiment presented on the $m_0 - m_{1/2}$ plane for fixed values of other mSUGRA parameters: $\tan(\beta) = 3, A_0 = 0, \mu < 0$ [91].

In order to compare the sensitivities of various searches across different experiments, a convention has been established to present search limits as exclusion contours in the $(m_0, m_{1/2})$ plane of the cMSSM parameter space. In case of the searches at the Tevatron experiments, a choice of values of other cMSSM parameters was: $\tan(\beta) = 3, A_0 = 0, \mu < 0$. Figure 5.8 shows the excluded region (green shading) from a D0 search for squarks and gluinos [92] along with the limits set by the direct chargino and slepton searches from the LEP experiments (light grey and dark grey shading). The solid black line shows the excluded region set by the CDF search and the dashed orange shading reveals the expected exclusion limit.

The experiments operating at the LHC are expected to extend the exclusion limits well beyond those in Figure 5.8 in the worst case scenario, or to confirm the existence of supersymmetry in the best case scenario. For the latter case, the naturally low rate of Standard Model backgrounds to the same-sign dilepton signature may enable it to provide the most compelling evidence. This consequence will be discussed in more detail in the following chapters.

5.7 Conclusions

Supersymmetric extensions of the SM present a promising way of describing nature and solving a large number of open questions raised by experimental observations and theo-

retical considerations. In addition, these extensions easily incorporate various frameworks for the unification of the electroweak and the strong interactions. These models provide us with predictions and phenomenological implications at the very high energies that can be probed at the LHC. Another interesting outcome of these models is the fact that one can use measurements at the LHC, to explore phenomena related to the dark matter, unifying in this way also particle physics and cosmology.

There is a large set of signatures that could be explored at the LHC in search for physics beyond the SM. In particular, the events with pairs of same-sign isolated leptons from hadron collisions are very rare in the SM, but can appear very naturally in supersymmetric extensions of the SM, as well as in other scenarios for physics beyond the SM. As discussed in the section 5.5, this class of events can be exploited as a signature of supersymmetry, universal extra dimensions, pair production of fermionic partners of the top quark, heavy Majorana neutrinos and same-sign top-pair resonances as predicted in theories with warped extra dimensions.

In the following two chapters we will present the physics analysis oriented towards searches for physics beyond the SM in events with pairs of isolated same-sign electrons, missing transverse energy and hadronic jets. The choice of search regions will be driven by considerations presented in this chapter. First, cosmological evidence for the dark matter suggests that we should concentrate on final states with significant missing transverse energy. Second, new physics signals with two same-sign leptons are likely to be produced with large cross section only by strong interactions, so we expect to observe a significant hadronic activity in these events. Beyond these simple guiding principles, our searches will be as independent of detailed features of the new physics models as possible.

Chapter 6

Event reconstruction

> Science is the topography of ignorance.
> Oliver Wendell Holmes [1], 1862.

6.1   Track reconstruction

The track reconstruction algorithms rely on a good estimate of the proton-proton interaction region, referred to as the beamspot. The beamspot is reconstructed with a dedicated algorithm and is used as a precise estimate of the primary interaction point prior to primary vertex reconstruction, and as the sole primary interaction point in case that no primary vertex is found. After the beamspot is determined, the standard track reconstruction is performed.
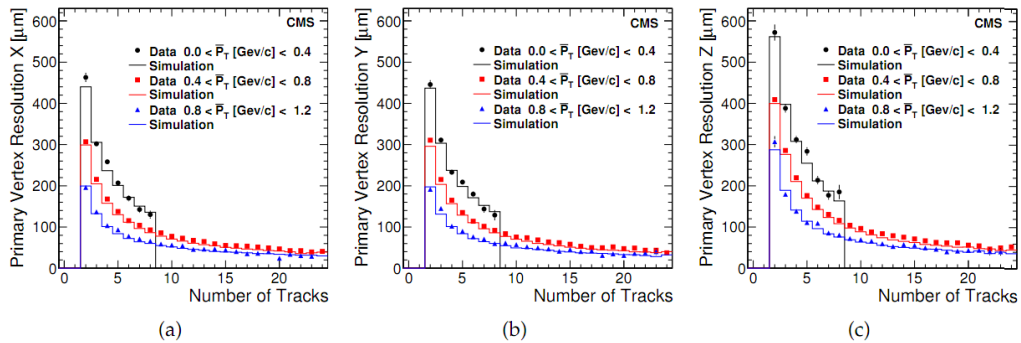
Starting from the location of the reconstructed beamspot, an initial step of track and vertex reconstruction is performed using only hits in the pixel detector. The pixel vertices found at this stage are used in the standard tracking. The standard track reconstruction at CMS is performed by the combinatorial track finder (CTF) [93]. Tracks are "seeded" either from triplets of hits in the tracker or from pairs of hits with an additional constraint from the beamspot, yielding an initial estimate of the trajectory. The track is then propagated outward in a search for compatible hits. In case hits are found, they are added to the trajectory and the track parameters and uncertainties are updated. This search continues until either the boundary of the tracker is reached or no more compatible hits can be found. An additional search for hits is performed starting from the outermost hits and propagating inward. In the final step, the whole collection of hits is fitted to obtain the best estimate of the track parameters.

The current implementation of the CTF performs six iterations. Between each iteration, hits that can be unambiguously assigned to tracks in the previous iteration are removed from the collection of tracker hits to create a smaller collection that can be used in the subsequent iteration. At the end of each iteration, the reconstructed tracks are filtered to remove tracks that are likely fakes and to provide a means of quantifying the

---

[1]Oliver Wendell Holmes, Sr., Border lines of knowledge (1862), p 211., Boston, Harvard University

quality of the remaining tracks. The filtering uses information on the number of hits, the normalised χ^2 of the track, and the compatibility of the track originating from a pixel vertex. The first two iterations use pixel triplets and pixel pairs as seeds to find prompt tracks with $p_T > 0.9$ GeV/c. The next iteration uses pixel triplet seeds to reconstruct low-momentum prompt tracks. The following iteration uses combinations of pixel and strip layers as seeds, and is primarily intended to find displaced tracks. The final two iterations use seeds of strip pairs to reconstruct tracks without pixel hits.

Figure 6.1: Primary vertex resolution distributions in (a) x, (b) y, and (c) z versus number of tracks. The three sets of results in each plot show different average p_T ranges. Within each p_T range, data and simulation are compared [21].

6.1.1   Primary Vertex Reconstruction

The reconstruction of the primary interaction vertex in the event starts from the track collection. The tracks are clustered on the basis of the z coordinate of the track at the point of closest approach to the beamline. The clusters are fitted with an adaptive vertex fitter, where tracks in the vertex are assigned a weight between 0 and 1 based on their proximity to the common vertex. The primary vertex resolution strongly depends on the number of tracks used in fitting the vertex and on their p_T. To measure the resolution, the tracks in an event with only one vertex are randomly split into two different sets and used to independently fit the primary vertex. The distribution of the difference in the fitted vertex positions can then be used to extract the resolution by fitting a Gaussian to it. As an example of the performance of the method, Figure 6.1 shows the resolutions of the x, y and z of the PV for different ranges of average track p_T. While the resolution differs considerably depending on p_T and multiplicity, the simulation accurately reproduces the data results. More details can be found in [21].

6.2   Electron reconstruction

Any electron that is absorbed by the ECAL material induces an electromagnetic shower and deposits its energy in several crystals of the ECAL. Due to the presence of material

in front of the calorimeter, a bremsstrahlung can occur before the electron reaches the calorimeter resulting in an additional electromagnetic shower geometrically spread in ϕ. Consequently, the total energy of an electron is expected to be deposited in the ECAL in a cluster of clusters of crystals (commonly named supercluster), which is spread in ϕ. For this reason, the total energy of an incident electron is inferred from the energy contained in the appropriately reconstructed supercluster [11]. The threshold on the energy of clusters considered in this reconstruction is approximately 1 GeV in transverse energy.

Due to radiative interactions of electrons in the tracker material, the expected energy loss for an electron has a long non-Gaussian tail. For this reason a dedicated Gaussian-sum filter (GSF) algorithm for electron track reconstruction in the CMS tracker has been developed [94]. The GSF tracking algorithm has been designed to follow the change of curvature of the electron track and allows for an unbiased estimate of the track momentum at both track ends. The same procedure also allows for a direct measurement of the fraction of energy lost due to the bremsstrahlung.

The electron reconstruction procedure employs two complementary algorithms: the "tracker driven" seeding algorithm and the "ECAL driven" seeding algorithm. The "tracker driven" seeding algorithm is more suitable for low p_T electrons and for electrons inside of jets of particles, while the ECAL driven algorithm is optimised for isolated electrons in a higher p_T range. The ECAL-driven seeding is performed by the reconstruction of superclusters in the ECAL and takes advantage of the fact that the supercluster energy weighted position is on the helix corresponding to the initial electron trajectory. Back-propagating the measured supercluster energy and position through the magnetic field, a prediction on the innermost tracker hits is inferred and used to match the pairs or triplets of hits in the inner tracker layers, which are used to build the electron track with the GSF algorithm. In case of the "tracker driven" seeding algorithm, the reconstruction is based on a multivariate analysis described in [95] and references therein.

The electron charge is measured in the CMS in three different ways. Two of these measurements are based on the curvature of the track reconstructed with two separate tracking algorithms: the standard CMS track reconstruction algorithm and the GSF algorithm. The third measurement is based on the relative position of the reconstructed electron supercluster and the projection to the calorimeter of a helix line segment built out of hits in the pixel detector. In order to reduce the effect of charge mismeasurement, the electron selection often requires that at least two or all three measurements give the same result. The physics analysis presented in this thesis will require that all three measurements agree.
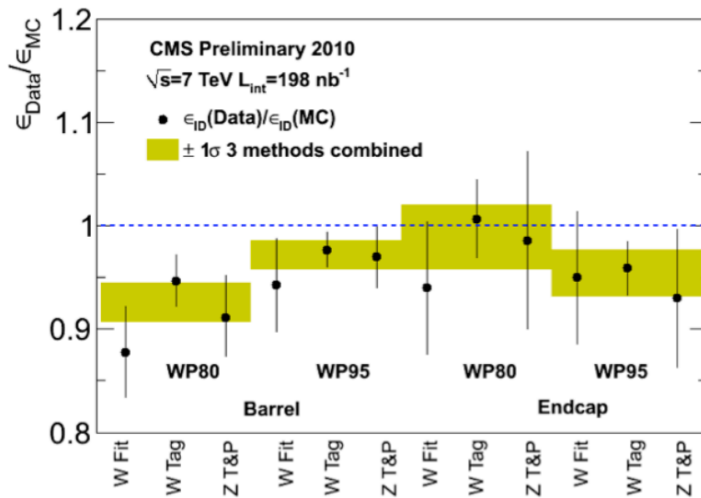
6.2.1 Electron selection and identification

Electron selection variables may be categorised in 3 groups: identification variables, isolation variables and conversion rejection variables.

The electron identification variables that have been found to have the highest discriminative power are: the energy-momentum match between the supercluster and the matching track, the variables measuring spatial matching between the GSF track and the

supercluster, the appropriately computed width of the supercluster in the η-direction, and the hadronic leakage variable[?]. It has been shown that the supercluster width in η is to a very good approximation unaffected by the spreading of the induced showering in the tracker material due to the magnetic field.

The isolation variables are defined as the sums over transverse energy or transverse momentum, evaluated in predetermined conical regions of $\Delta R = \sqrt{(\Delta\phi)^2 + (\Delta\eta)^2}$ around the electron. These sums $I_{Tracker}$, I_{ECAL} and I_{HCAL} are computed separately for three sub-detectors: the tracker, the ECAL and the HCAL. In addition to these variables, a relative isolation $RelIso = (I_{Tracker} + I_{ECAL} + I_{HCAL})/p_T$ is often used in the analyses. The isolation variables are expected to be sensitive to the amount of activity of charged and neutral particles in the vicinity of the reconstructed electron. Since it is expected for electrons to experience the bremsstrahlung energy loss, a special care is taken to remove from the isolation sums the contributions from bremsstrahlung photons and possible resulting conversion electrons.

Figure 6.2: Ratio of the measured electron selection efficiency over the expected efficiency from simulation for the reference selections with 198 nb^{-1} data. The values are shown for both the tag-and-probe method using $Z \rightarrow ee$ events and for the tag-and-probe and ML fit methods based on W events, as well as separately for the ECAL barrel and ECAL endcaps. Combined values of the efficiency and associated errors are indicated with yellow bands [96].
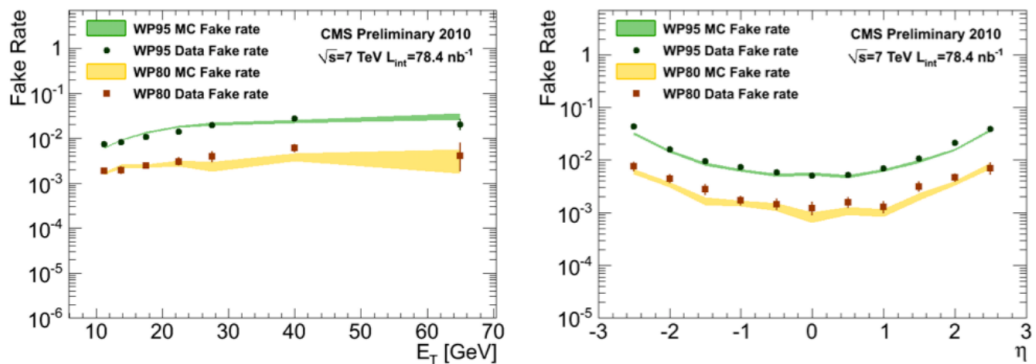
Three additional sets of variables are used to reject electrons which originate from photon conversions. First, these electrons have in average a greater distance from the beam position. Thus, the electron transverse impact parameter can be used to discriminate real electrons from the conversion electrons. Second, the electron from a conversion is expected to have one or more missing hits in the innermost tracker layers. Finally, electrons from conversions can be identified by finding the partner conversion track. This is done by looking for an oppositely charged track whose polar angle is close to the one

of the electron track and whose distance at the point where the two tracks are parallel is small.

In order to standardise the electron selection, a series of reference selections based on the simple cuts on the variables discussed above have been established. These reference selections have been determined using simulated samples as selections for which the selection of prompt electrons of $E_T > 20\,\mathrm{GeV}$ have an average efficiency of 95%, 90%, 85%, 80% and 70%. During the year 2010, electron selection in most of the physics analyses has been performed according to one of these reference selections. In the physics analysis presented in this thesis, we will consider only the 90% and the 80% working points, and we will refer to them hereafter as WP90 and WP80.

6.2.2 Electron selection efficiency and purity

Several methods have been developed for the measurement of the efficiency of the chosen electron selection. The baseline method for the electron selection efficiency measurement is the "tag-and-probe" method which relies on easily reconstructible $Z \to ee$ decays. The other two alternative methods are based on $W \to e\nu_e$ events and employ either a tag-and-probe type of method or an unbinned maximum likelihood (ML) of the W transverse mass. All these methods are described in details in reference [96].

Figure 6.3: Electron fake rate per reconstructed electron candidate as a function of (a) E_T and (b) η for the WP95 and WP80 electron selections in data and simulation [96].

The results of the electron selection efficiency study performed with $198\mathrm{nb}^{-1}$ of data are summarised in Figure 6.2. The figure represents the ratio of the measured efficiency to the efficiency expected from simulation for the three methods described above and for the two standardised selections corresponding to the 95% and the 80% working points. Results are shown separately for electron candidates in the ECAL barrel and in the ECAL endcaps. A good agreement is found between the three methods and the measured efficiencies are found to agree well with the expectation from simulation. The combined efficiency values and their errors are also indicated.

Beyond the simple data-versus-simulation agreement between the rate of reconstructed electron candidates and the distributions of the variables used for electron identification, the determination of fake rates for a given electron identification is a crucial performance measurement. The fake rate is defined as the fraction of reconstructed electron candidates that pass the background selection and a given electron identification over the total number of electron candidates passing the background selection.

Figure 6.3 shows the fake rate as a function of the reconstructed p_T and η for the simple selection and the working points WP95 and WP80. The fake rate measured in data is found to be in a reasonable agreement with simulation in both p_T and η.

6.3 Muon reconstruction

The reconstruction of muons in CMS is performed using the information both from the tracker system and from up to four stations of muon detectors. In addition to this information, muon energy deposits in the ECAL, HCAL and HO are also used for muon identification purposes.

At the beginning of the standard muon reconstruction for proton-proton collisions, tracks are reconstructed independently in the tracking system (tracker track) and in the muon system (standalone-muon track). For this reason, CMS employs two reconstruction approaches: the Global Muon reconstruction and the Tracker Muon reconstruction. In case of the Global Muon reconstruction, a tracker track is matched to a standalone-muon track and a global-muon track is fitted combining hits from both of these tracks. The global-muon has the advantage over the tracker-only fit and can improve the momentum resolution at transverse momenta of $p_T > 200\,\mathrm{GeV/c}$.

In case of the Tracker Muon reconstruction, all tracker tracks with $p_T > 0.5\,\mathrm{GeV/c}$ and $p > 2.5\,\mathrm{GeV/c}$ are considered as muon candidates and are extrapolated to the muon system, taking into account the expected energy loss and the uncertainty due to multiple scattering. If at least one muon segment matches this extrapolated track, the corresponding track qualifies as a tracker-muon track. At low momentum of about $p < 5\,\mathrm{GeV/c}$, this approach is more efficient than the global muon reconstruction, because it requires only one muon segment to be matched in the muon system.

The combination of these algorithms provides a robust and efficient muon reconstruction in CMS. In addition, supplementary information on muon identification is stored for each candidate. Each physics analysis can achieve the desired balance between identification efficiency and purity by applying a selection based on these muon identification variables.

There are several standard selections provided in CMS. One of the very often used selections is the so called "tight muon selection". In case of this selection, the rate of muons from light-hadron decays are expected to contribute less than 10%, while the hadronic contribution is suppressed to about 1% level, all at the price of 1%-3% percent loss in the efficiency for selection of true muons such as those originating from Z and W decays. This muon selection is also the selection that will be used in the physics

analysis presented in this thesis. All the details on the muon reconstruction, selection and identification algorithms, as well as on their performance can be found in [97].

6.4   Jet reconstruction

Jets of particles are the experimental signatures of quarks and gluons produced in high energy interactions such as the hard scattering of partons in proton-proton collisions. The production cross section of jets at the LHC collisions is very large and, hence, the jets are expected to be in a focus in many studies of new kinematic regimes, confronting predictions of perturbative **Q**uantum **C**hromo **D**ynamics (QCD) and probing physics processes within and beyond the standard model. For this reason, a good reconstruction of jets and a detailed understanding of their energy calibration and resolution is of utmost importance.

In CMS, the jets are reconstructed and measured from the detector raw input data using dedicated clustering and reconstruction algorithms [98]. There are three different approaches to reconstruct jets in the experiment:

- the calorimeter-based jet reconstruction, which attempts to reconstruct jets from the energy deposits in the electromagnetic and hadronic calorimeter cells (CALO jets) [99];

- the Jet-PlusTrack reconstruction, which improves the measurement of calorimeter jets by exploiting the information on tracks associated to each jet (JPT jets) [100];

- the Particle Flow method, which first combines the information from all relevant sub-detectors and attempts to reconstruct each individual particle in the event, and then performs jets clustering and reconstruction from the resulting list of particles (PF jets) [101].

In all three approaches jets are by default clustered using the "anti-k_T" algorithm with the cone-size parameter $R = 0.5$ [102]. In case of the PF jets, the jet momentum and spatial resolutions are expected to be improved with respect to calorimeter jets as the use of the tracking detectors and of the excellent granularity of the ECAL allows to resolve and precisely measure charged hadrons and photons inside jets, which constitute about 90% of the jet energy.

6.4.1   Jet selection and identification

The CMS experiment has developed jet identification criteria for reconstructed jets which are found to retain the vast majority of real jets in the simulation while rejecting most of the fake jets arising from calorimeter and readout electronics noise. These have been studied and established in non-collision data samples such as cosmic trigger data or data from triggers on empty bunches during the LHC operation.

In order to pass jet identification, the calorimeter jets are required to have a fraction of electromagnetic energy $EMF > 0.01$ if within the ECAL region of $|\eta| < 2.6$, while

the number of calorimeter cells containing 90% of jet energy must be greater than 1. At the same time the fraction of jet energy in the hottest HPD unit of the HCAL readout within the jet must be less than 98%. The JPT jets are treated as calorimeter jets with respect to the identification criteria. The detailed explanations and motivation for all these criteria are given in [103].

On the other hand, the PFlow jets are required to have a fraction of charged hadrons $CHF > 0.0$ if within the tracking region of $|\eta| < 2.4$, a fraction of neutral hadron $NHF <$ 1.0, charged electromagnetic (electron) fraction $CEF < 1.0$ and neutral electromagnetic (photon) fraction $NEF < 1.0$. These requirements have been established in order to remove fake jets arising from spurious energy depositions in a single sub-detector and their detailed explanation can be found in [101] and references therein.

In the following section we will discuss the performance of the jet calibration procedures in the CMS using all three types of jets. In the physics analysis presented in the last two chapters of this thesis we will use exclusively the PF jets which satisfy the identification criteria described above.

6.4.2   Jet energy calibration

Reconstructed jets typically have an energy that is different from the energy of the corresponding jet of particles originating from the final state parton. The main cause for this energy mismatch is a non-uniform and a non-linear response of the CMS calorimeters. In a similar way, electronics noise and proton-proton interactions occurring in the same bunch crossing can lead to additional unwanted energy.

For this reason, on top of the jet clustering and reconstruction procedure, CMS employs a dedicated jet energy calibration with the purpose of relating, in average, the energy of a jet measured with the detector (so called raw jet) to the energy of the original particle jet. The correction is applied sequentially, in the form of multiplicative factors, on each component of the jet momentum four-vector p_μ^{raw}:
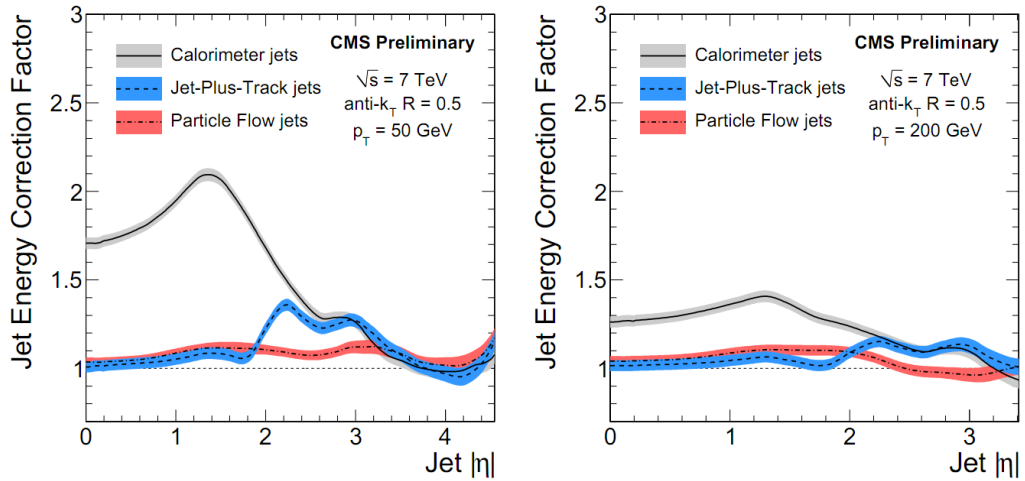
$$p_\mu^{corrected} = C(p_T, \eta) \ p_\mu \qquad (6.1)$$

The first step in the chain of the factorized corrections is the "offset" correction. Its purpose is to estimate and subtract the energy not associated with the high-pT scattering. The excess energy includes contributions from electronics noise and pile-up. In the second step the reconstructed jets are calibrated with correction factors based on the information from the simulation ("MC truth"). This correction removes the bulk of the jet response non-uniformity in η and the non-linearity in p_T. At the end, small residual corrections are applied to these jets. The corrections are based on the measurements of the relative jet response in η and the absolute jet energy scale in p_T, and, in practice, are applied in the form of:

$$C(p_T^{raw}, \eta) = C_{offset}(p_T^{raw}) \ C_{truth}(p_T^{off}, \eta) \ C_{residual}(p_T^{truth}, \eta) \qquad (6.2)$$

where p_T^{off} is the transverse momentum of the jet after applying the offset correction and p_T^{truth} is the transverse momentum of the jet after all previous corrections.

The relative jet energy response determination is performed exploiting the transverse momentum conservation and the balance of the p_T in QCD events with two "back-to-back" jets. The method requires that one jet is reconstructed in the central region of the calorimeter, $|\eta| < 1.3$, and the other jet at an arbitrary η. The central region is chosen as reference because of the uniformity of the detector and since it has the highest reach in the jet transverse momentum.

Figure 6.4: The total jet energy correction factor and its uncertainty (band) as a function of jet η for two jet p_T values. The results are presented for all three jet reconstruction algorithms used in the CMS, using $\mathcal{L}_{int} = 3\,\mathrm{pb}^{-1}$ of integrated luminosity.

The absolute jet energy response is measured in the reference region $|\eta| < 1.3$ using $\gamma + $ jets events, with two different methods which exploit the momentum balance in the transverse plane between the photon and the recoiling jet. In these two methods, the photon is chosen as a reference object because it can be measured in the ECAL with sufficiently high accuracy. In addition to the $\gamma + $ jets events, the absolute jet energy response can also be determined from the $Z^0 + $ jets events. The accurate measurements with this method will be possible after more than $40\,\mathrm{pb}^{-1}$ of integrated luminosity is collected [104].

The total jet energy calibration is performed with both simulation and data using the formula (6.2). The total jet energy correction factor and its uncertainty obtained in this way are shown in Figure 6.4 as a function of η for two fixed values of the jet p_T. The results are presented for all three jet reconstruction approaches used in CMS using a data sample corresponding to an integrated luminosity of $3\,\mathrm{pb}^{-1}$. The figure shows that CALO jets require a much larger correction factor compared to the track-based algorithms. In case of jets with a momentum of 50 GeV this factor reaches the value of about 2.2 in the region of transition between detector barrels and endcaps. On the other side, in the region beyond

the tracker coverage, where PF and JPT have no adavantge over the CALO approach, all three jet types are in a mutual agreement within the systematic uncertainties. The detailed studies have shown that these jet calibration procedures give rise to about $3-6\%$ of uncertainty on the overall jet energy scale in a wide region of jets p_T from 30 (20, 15) GeV up to 2 TeV in case of CALO (JPT, PF) jets. All the details on the jet calibration procedures and associated uncertainties can be found in [104].

6.5 Missing transverse energy

A missing transverse energy is one of the most important observables used to discriminate the decay processes which contain neutral weakly interacting particles from those processes which do not contain these particles. This particle can be a neutrino, but it can also be one of the particles predicted by various models which try to describe physics beyond the standard model.

The missing transverse energy E_T^{miss} is computed as the magnitude of the missing transverse momentum $\vec{p}_T^{\,\mathrm{miss}}$, which is reconstructed as the negative vectorial sum of the transverse momenta of all final-state particles which are reconstructed in the detector. CMS has developed three distinct algorithms to reconstruct the missing transverse energy:
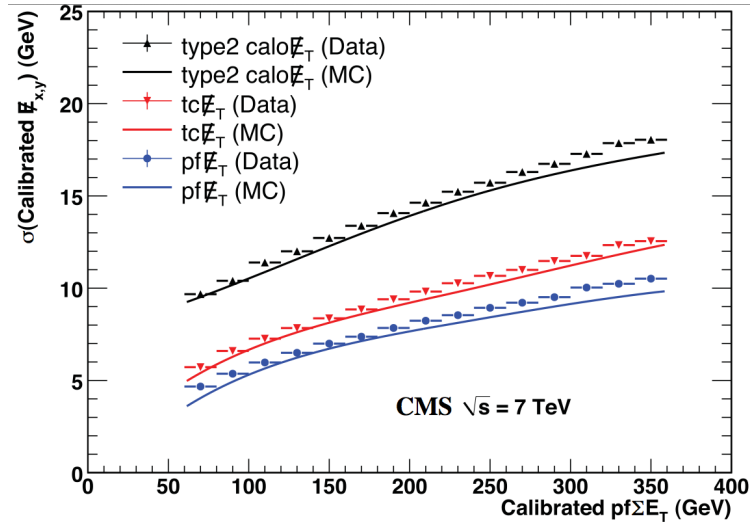
- the Calo E_T^{miss}, based on energies deposited in the CMS calorimeters;

- the TC E_T^{miss}, calculated by replacing the calorimeter energies matched to charged hadrons with the momenta of corresponding hadron tracks;

- the PF E_T^{miss}, calculated using a complete particle-flow technique [101].

These three algorithms closely correspond to the three approaches of jet reconstruction used in CMS and described in the previous section. In case of the Calo E_T^{miss} and PF E_T^{miss}, a dedicated correction scheme has been developed to account for the effects arising from the non-compensating nature of the calorimeter by applying jet energy scale corrections for calorimeter towers within jets. In case of Calo E_T^{miss} another set of energy scale corrections is used for calorimeter towers outside of jets.

The E_T^{miss} aggregates the information collected from all the detector systems in CMS and represents one of the most complex observables used in the CMS event reconstruction. In particular, the reconstruction of E_T^{miss} is very sensitive to mis-measurements of particle momenta, malfunctions of various detector components, existence of poorly instrumented regions of the detector and many others. Thus, any of these factors may result in an artificial E_T^{miss} being reconstructed in the detector.

In order to understand and to fully control most of these effects, the performance of these E_T^{miss} reconstruction techniques has been thoroughly studied using minimum bias events and QCD jet events collected by the experiment. These events are expected to provide a good testbed to study the performance of the E_T^{miss} measurement, as well as to examine various instrumental effects. Comparisons of the E_T^{miss} distributions between data and simulation in these two event topologies have shown reasonable agreement, indicating a good understating of the detector and its effects [105].

The resolution of the E_T^{miss} has also been studied in events with a purely hadronic final state, where the observed E_T^{miss} is expected to arise from resolution effects only. It has been shown that both the PF E_T^{miss} and TC E_T^{miss} provide improvements in the E_T^{miss} resolution compared to the Calo E_T^{miss}. At the same time, the PF E_T^{miss} yields the best resolution in the E_T^{miss} reconstruction [105]. Figure 13 illustrates the results of this study.

Figure 6.5: The calibrated E_T^{miss} resolution compared between data and simulation in events containing at least two jets with $p_T > 25$ GeV. The E_T^{miss} resolution is characterised by the σ of a Gaussian fit to the distribution of the x and y components of $\vec{p}_T^{miss}$. The results are presented for all three E_T^{miss} reconstruction algorithms described in the text, using $\mathcal{L}_{int} = 3 \, \text{pb}^{-1}$ of integrated luminosity [105].

Thanks to the encouraging results on the performance of the PF E_T^{miss} algorithm, we have decided to use the E_T^{miss} observable reconstructed with this algorithm in the physics analysis presented in this thesis. This decision is also consistent with the decision to use the PF jets algorithm for the jet reconstruction and identification in the same analysis.

Chapter 7

Experimental method for leptonic background prediction

<div align="right">

If your experiment needs statistics,
you ought to have done a better experiment.
E. Rutherford[1]

</div>

7.1 Final states with two leptons

The leptonic final states in hadronic collisions present an excellent and promising playground for the testing of the SM predictions and for searches for physics phenomena beyond the SM. At the end of the previous chapter we have discussed a possibility to exploit the potential of final states with pairs of leptons in testing the predictions of the MSSM at the LHC.

An important step in the analysis of any process in which one or more leptons in the final state are produced in the hard parton-parton scattering is the estimation of the rate of the processes which intrinsically do not have this type of leptons. These are typically either processes with leptons which originate from decays of heavy mesons created during the hadronization of QCD jets, or processes in which lighter mesons get incorrectly reconstructed as leptons. This type of processes is commonly referred to as the "reducible background" processes. One example is the SUSY production of a pair of same sign leptons. In this case, the production of both $t\bar{t}$ pairs and W + jets represent a reducible background for our process.

In the further discussion, we will name "fake lepton" any jet mis-reconstructed as a lepton and any lepton originating from a heavy meson decay. In a similar way, any electron originating from a photon conversion will be named "fake electron". On the other hand, the leptons which were produced directly in the hard interactions will be named "prompt" leptons. These will also include any lepton produced in the decay of a SM gauge boson

---
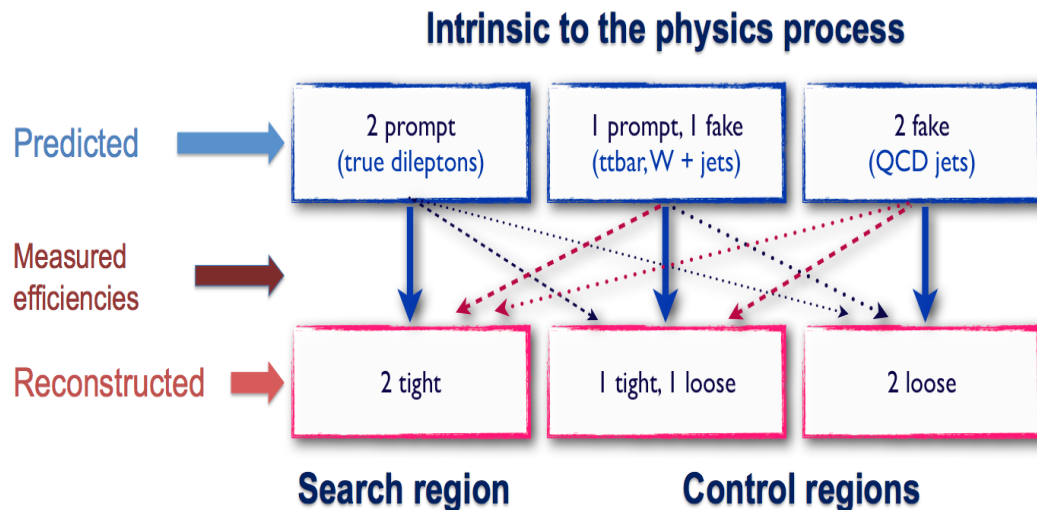
[1]E.Rutherford, as quoted in N.T.J. Bailey, The Mathematical Approach to Biology and Medicine, Wiley, New York 1967.

or SUSY gaugino. The reason is that their isolation and identification properties are practically indistinguishable from the ones of leptons from the hard interactions.

Over the decades of experimental research at the Tevatron, several strategies and methods have been developed to estimate the rate of processes which contain fake leptons. One of these methods, commonly called as the "fakeable objects" method, has been applied in several experimental searches with final states that include one or two leptons. The method considers both the leptons which satisfy the selection criteria used for the physics analysis, and the leptons which do not satisfy these criteria, but do satisfy some less strict selection criteria. These criteria are usually imposed on the isolation and identification observables used for the lepton selection. The principal assumptions of the method is that the probability for fake leptons which pass the less strict selection criteria to also pass the analysis selection criteria mildly depends on the nature of the process, but only on the lepton kinematic properties. The method also assumes that it is possible to correctly measure this probability in a conveniently chosen data sample and that it can be applied to extract the rate of background processes with fake leptons in the data sample where the physics analysis is performed. This probability, or the efficiency, is commonly called "fake ratio" f and it is assumed that it can be completely determined from the appropriately chosen sample of events as a function of the lepton kinematics.

Figure 7.1: A schematical representation of the method for the prediction of background from fake and non-isolated leptons. The method is based on the "tight-to-loose" selection efficiencies for the "prompt" and the "fake" leptons that are measured from the data.

In this thesis, we extended the method in three important aspects. First, the method is extended to take into account the non-zero probability for a prompt lepton to fail the selection criteria used in the analysis. As a result, these leptons are not considered in the analysis in the same way as the fake ones, and the background rates are, thus, not overestimated.

The extension is accomplished by introducing the probability for a prompt lepton which passes the less strict selection criteria to also pass the selection used in the analysis. This probability, or the efficiency, is named the "prompt ratio" p. This ratio is measured by a "tag and probe method" [106] in a sample of Z^0 + jets events.

Second, the method is completely generalised to be applicable to an arbitrary multiplicity of leptons, including the case with mixed number of e and μ leptons (with different f and p ratios) in the same event. The method also provides the formulae for the estimation of statistical and systematic uncertainties of the method in a generalised way.

Third, the method is extended to allow separate handling of different classes of background processes. In particular, dedicated formulae are derived that apply different fake ratios for different classes of background processes and enable a more accurate estimate of signal and background contributions.

All these extensions make the method quite general and applicable to a wide range of physics analyses. The work has been done together with other colleagues from ETH Zürich and has been reported in [107]. In this chapter we will present the details of the method and discuss some of its most important features. In the chapter 8, we will apply the method in the physics analysis dedicated to search for physics beyond SM in final states with pairs of same-sigm electrons.

Hereafter, the selection criteria used in the analysis will be called "tight selection" or "signal region", while the leptons that pass this selection will be called "tight" leptons. In a similar way, the looser selection criteria will be called "loose selection", and the leptons that pass this selection will be called "loose" leptons.

The basic principles of the method can be easily understood by looking at the example of final states with two leptons and the schematic diagram presented in Figure 7.1. All the final states that satisfy the looser selection criteria can be separated in three groups: a group with two tight leptons, a group with one tight and one loose lepton, and a group with two loose leptons (represented as red boxes in the diagram). Contributions to these final states can arise from three classes of physics processes: a class with two prompt leptons, a class with only one prompt lepton and a class with no prompt leptons (represented as blue boxes in the diagram). If we assume a non-zero probability for a prompt lepton to fail the "tight selection" criteria and a non-zero probability for a fake lepton to pass the "tight selection" criteria, then any of the three classes of processes can contribute to any group of final states. Therefore, if we measure the number of events in each of the three groups of final states, and if we separately measure the selection efficiencies for prompt and fake leptons, we will be able to infer the number of events in each of the classes of our physics processes. In the rest of this section we will present the full algebra for the estimation of the number of events with prompt leptons.

In order to estimate the number of events with one or two fake leptons within the tight selection, we define several variables and observables:

- N_l - the number of events where both reconstructed leptons pass the loose selection;

- N_{t2} - the number of events where both loose leptons, also pass the tight selection;

- N_{t1} - the number of events where one of the loose leptons passes the tight selection

and the other one fails;

- N_{t0} - the number of events where both loose leptons fail the tight criteria;

- N_{pp} - the number of events with two prompt leptons, both passing the loose criteria;

- N_{fp} - the number of events with one prompt and one fake lepton, both passing the loose criteria;

- N_{ff} - the number of events where two fake leptons, both passing the loose criteria.

The observables N_{t2}, N_{t1} and N_{t0} are measured from the data, and are directly related to the true number of events containing two prompt, one prompt and one fake, or two fake leptons (as described above). Following all the previous considerations we can directly write the following relations:

$$N_l = N_{pp} + N_{fp} + N_{ff} = N_{t2} + N_{t1} + N_{t0} \qquad (7.1)$$

$$N_{t2} = p^2 N_{pp} + pf N_{fp} + f^2 N_{ff} \qquad (7.2)$$

$$N_{t1} = 2p(1-p)N_{pp} + [f(1-p) + p(1-f)]N_{fp} + 2f(1-f)N_{ff} \qquad (7.3)$$

$$N_{t0} = (1-p)^2 N_{pp} + (1-p)(1-f)N_{fp} + (1-f)^2 N_{ff} \qquad (7.4)$$

These equations assume that the prompt and the fake ratios for different leptons are mutually independent. The factor p and $(1-p)$ are averaged over the whole kinematic region of the distribution of the considered prompt leptons and, similarly, f and $(1-f)$ are averaged over the whole kinematic region of the distributions of the fake leptons. After inverting this set of equations, one can easily obtain the expression for the number of events with exactly two prompt leptons in terms of measured quantities N_{t2}, N_{t1} and N_{t0}:

$$N_{pp} = \frac{1}{(p-f)^2}[N_{t2} - f(1-f)N_{t1} + f^2 N_{t0}] \qquad (7.5)$$

with the number of the signal events which remain in the sample selected with the tight cuts being given by $N_{signal} = N_{pp}^{pass} = p^2 N_{pp}$. Similarly, one can derive the expressions for the number of events with exactly one prompt and one fake lepton, as well as for the number of events with two fake leptons:

$$N_{fp} = \frac{1}{(p-f)^2}[-2fp N_{t0} + [f(1-p) + p(1-f)]N_{t1} - 2(1-p)(1-f)N_{t2}] \qquad (7.6)$$

$$N_{ff} = \frac{1}{(p-f)^2}[p^2 N_{t0} - p(1-p)N_{t1} + (1-p)^2 N_{t2}] \qquad (7.7)$$

Then, the number of events from these two classes of background processes which remains in the sample selected with the tight selection criteria are $pf N_{fp}$ and $f^2 N_{ff}$, respectively. In practical application, the first one would correspond to the $t\bar{t}$ background, where the prompt lepton comes from a top quark decay and the fake lepton from the leptonic b decay of the other top quark. It might also include a contribution from W

+ jets. The second expression then would provide a handle on the remaining QCD background contribution.

The previous expressions can easily be derived for the case when fake ratios are different in different classes of background processes. At the same time, it can also be put in a form which exhibits the recursive relationship between the N_{ff}, N_{fp} and N_{pp}. The main advantage of this form is that it easily allows for an comprehensive application of different fake ratios for different classes of background processes.

Let us define the ratio f_{ff} as the lepton "fake" ratio for the background processes with two fake leptons and the ratio f_{fp} as the lepton "fake" ratio for the background processes with one fake and one prompt lepton. It can be verified that the recursive expressions for the expressions (7.5) - (7.7) given above take the following form:

$$N_{pp} = \frac{1}{p^2}[N_{t2} - pf_{fp}N_{fp} - f_{ff}^2 N_{ff}] \tag{7.8}$$

$$N_{fp} = \frac{1}{p(p - f_{fp})}[pN_{t1} - 2p(1 - p)N_{t2} - 2(p - f_{ff})f_{ff}N_{ff}] \tag{7.9}$$

$$N_{ff} = \frac{1}{(p - f_{ff})^2}[p^2 N_{t0} - p(1 - p)N_{t1} + (1 - p)^2 N_{t2}] \tag{7.10}$$

The importance of these expressions is that they acknowledge that, due to different kinematical properties of different background processes, the fake ratios may depend on the type of background. Therefore, instead of trying to determine a universal fake ratio as a function of the event properties, which has proven to be difficult in practice, these expressions open the possibility to determine individual fake ratios directly from the contributing backgrounds and apply them to compute the number of signal and background events in the selected sample.

7.2 Final states with arbitrary lepton multiplicities

In the previous section, we have derived the algebraic expressions for the number of events with two, one or no prompt leptons which contribute to the final states with exactly two tight leptons. These expressions can be generalised to the number of events with an arbitrary number n_p of prompt and an arbitrary number n_f of fake leptons, used for the case of $n = n_p + n_f$ leptons in the final state.

Let us first obtain the general recursive equations for the case when the probability for the prompt lepton to fail the tight selection is negligible ($p = 1$). In this case, the number of events N_{n_f,n_p}^{pass} with exactly n_p prompt leptons passing the tight selection is:

$$N_{n_f,n_p}^{pass} = (1 - f)^{n_f} N_{n_f,n_p} \tag{7.11}$$

where the factor $(1 - f)^{n_f}$ describes the probability that the other n_f fake leptons do not get reconstructed as tight leptons.

This number can be inferred from the number of observed events N_{t,n_p} with n_p tight

leptons, if we subtract from it the total number of events in which n_p tight leptons have been reconstructed from the classes of process N_{n_f+i,n_p-i}, where $i = 1,..,n_p$. The contribution from each individual class is given by:

$$C_i^{n_f+i}(1-f)^{n_f}f^i N_{n_f+i,n_p-i} \tag{7.12}$$

where C_i^n is the combinatorial factor $C_i^n = \frac{n!}{(n-i)!i!}$. Finally, we obtain the set of recursive formulae for the number of events N_{n_f,n_p} of that class of physics process as:

$$N_{n_f,n_p} = \left(\frac{1}{1-f_{n_p}}\right)^{n_f}\left[N_{t,n_p} - \sum_{i=1}^{n_p} C_i^{n_f+i}(1-f)^{n_f}f^i N_{n_f+i,n_p-i}\right] \tag{7.13}$$

where the expressions go over the whole set of partitions (n_p, n_f) that fulfil the conditions $n = n_p + n_f$.

In a similar way, one can obtain the expressions for the general case when the probability for the prompt lepton to fail the tight selection is not negligible ($p < 1$). The set of these recursive relations, in case the fake ratio f_{n_p} corresponds to the class of backgrounds with eaxctly $n_p = n - n_f$ prompt leptons, is given by:

$$N_{n_f,n_p} = \frac{1}{p^{n_p}}\left(\frac{p}{p-f_{n_p-i}}\right)^{n_f}\left[N_{t,n_p} - \sum_{i=1}^{n_p} C_i^{n_f+i}(\frac{p-f_{n_p-i}}{p})^{n_f}(f_{n_p-i})^i p^{n_p-i}N_{n_f+i,n_p-i} - \right.$$
$$\left. - \sum_{i=1}^{n_f}(-1)^{i+1}C_i^{n_p+i}(\frac{1-p}{p})^i N_{t,n_p+i}\right] \tag{7.14}$$

where the expressions again go over the whole set of partitions (n_p, n_f) that fulfil the conditions $n = n_p + n_f$.

The expression (7.14), in the special case of a pair of leptons, yields the set of equations (7.5), (7.6) and (7.7) derived in the previous section. More details on this set of equations and their properties are given in the Appendix. This appendix also lists these equations in case of multi-lepton final states with both muons and electrons.

7.3   Estimation of uncertainties

The equations presented in the previous sections can be directly used to estimate the number of events from background processes which are expected in the signal region. In addition to these, it is important to be able to compute the expected statistical and systematic uncertainties associated with this estimation method.

The expressions for the numbers of events with exactly n_p prompt leptons from the class N_{n_f,n_p}^{pass} passing the tight selection, is a linear function of the number of observed events $N_{t,n-i}$ with $n-i$ leptons which pass the tight selection ($i = 0,..,n$) with two fixed parameters n_f, n_p satisfying $n = n_f + n_p$ and the measured parameters f and p.

Therefore, it can be in general expressed as:

$$N_{n_f,n_p}^{pass} = \sum_{i=0}^{n} \omega_i(f,p,n_f,n_p) N_{t,n-i} \tag{7.15}$$

where $\omega_i(f,p,n_f,n_p)$ are the corresponding coefficients in the linear expression for N_{n_f,n_p}. Since $N_{t,n-i}$ are statistically uncorrelated and assumed to be Poisson distributed, the statistical uncertainty on N_{n_f,n_p}^{pass} can be in general expressed as

$$\Delta N_{n_f,n_p}^{pass}\bigg|_{stat} = \sqrt{\sum_{i=0}^{n}\left(\frac{\partial N_{n_f,n_p}^{pass}}{\partial N_{t,n-i}}\Delta N_{t,n-i}\right)^2} = \sqrt{\sum_{i=0}^{n}\omega_i^2 N_{t,n-i}} \tag{7.16}$$

The systematic uncertainties of the method originate from the uncertainties on the p and f ratios used in the expressions. If we assume that p and f are measured in different physics processes and that, hence, their uncertainties are uncorrelated, the systematic uncertainty on the number of events passing the tight selection N_{n_f,n_p}^{pass} can be obtained as:

$$\Delta N_{n_f,n_p}^{pass}\bigg|_{syst} = \sqrt{\left(\frac{\partial N_{n_f,n_p}^{pass}}{\partial p}\Delta p\right)^2 + \left(\frac{\partial N_{n_f,n_p}^{pass}}{\partial f}\Delta f\right)^2} \tag{7.17}$$

According to relation (7.1), the total number of leptons is fixed. For this reason, the different N_{n_f,n_p}^{pass} for different values of n_p and n_f will be mutually correlated and their systematic uncertainties are expected to be correlated as well.

Using the previous considerations, one can easily compute the uncertainties on the predicted number of events with two prompt leptons, given by (7.5), which pass the tight selection. In this particular case, the contributions from Δf and Δp can be expressed as:

$$B_{pp,p} = \left|\frac{p}{N_{pp}^{pass}}\frac{\partial N_{pp}^{pass}}{\partial p}\right| = \frac{2f}{p-f} \tag{7.18}$$

$$B_{pp,f} = \left|\frac{f}{N_{pp}^{pass}}\frac{\partial N_{pp}^{pass}}{\partial f}\right| = \frac{2f}{p-f} + f\left[O\left(\frac{N_{t1}}{N_{pp}}\right) + O\left(\frac{N_{t0}}{N_{pp}}\right)\right] \tag{7.19}$$

and the systematic uncertainty (7.17) can be expressed in a simpler form:

$$\Delta N_{pp}^{pass}\bigg|_{syst} = \sqrt{\left(B_{pp,p}\frac{\Delta p}{p}\right)^2 + \left(B_{pp,f}\frac{\Delta f}{f}\right)^2}\,N_{pp}^{pass} \tag{7.20}$$

Similar expressions can be obtained for the systematic uncertainty on the predictions of N_{fp} and N_{ff}. It is interesting to notice that all the systematic uncertainties on the predicted numbers of events increase practically linearly with the corresponding number of events, unlike the statistical uncertainties. For this reason, only the relative statistical

uncertainty can be improved by increasing the sample of selected events. On the other hand, the relative systematic uncertainty can be improved only if relative uncertainties on the prompt ratio p and fake ratio f can be reduced. The latter can only partially be achieved by reducing the statistical uncertainty on the measurement of these ratios. In fact, it can significantly be reduced only if the systematic uncertainties related to the determination of these ratios are reduced. However, this might not be trivial in the general case, as there are many effects that are difficult to account for. Examples are the approximate p_T and η dependence, or a dependence on the number of jets, which may differ considerably in the reaction where they are measured from the channel where they are applied. Since all these effects potentially induce a large uncertainty on the f and p ratios, these need to be thoroughly tested.

7.4   Conclusions

In this chapter we have presented an extension of a method that has been used previously at Tevatron and applied in several experimental searches with final states that include one or two well reconstructed leptons. The extended method takes into account the non-zero probability for a prompt lepton to fail the selection criteria used in the analysis. It is generalised to be applicable to an arbitrary multiplicity of leptons, including the case with mixed number of e and μ leptons. The method also provides the formulae for the estimation of statistical and systematic uncertainties of the method in a generalised way. In addition, the method is extended to allow separate handling of different classes of background processes.

The application of the method to the physics analysis will be presented in the following chapter, as an integral part of the experimental search for physics beyond the Standard Model in events with two same-sign electrons.

Chapter 8

Search for physics beyond the SM

> No phenomenon is a true phenomenon
> until it is an observed phenomenon.
> John A. Wheeler

8.1   Introduction

The CMS experiment offers unprecedented possibilities in exploring the physics phenomena at energy scales of up to a few TeV and, in particular, in searches for physics beyond the SM. In chapter 5 we have reviewed the main reasons why supersymmetric models represent a very attractive extension of the SM. We have explained that the final states with a pair of same-sign leptons, accompanied by energetic jets and significant missing transverse energy, represent a particularly interesting topology to search for new physics in events produced at hadron collisions. We have also explained that pairs of same-sign leptons can be naturally produced in a large number of other physics scenarios, while the rate of the Standard Model processes with the same final state is very low.

In this chapter, we present the full physics analysis performed to search for physics beyond the SM in events with a pair of same-sign electrons, several energetic jets and significant missing transverse energy. The analysis has been performed using a data sample that corresponds to an integrated luminosity of $36\,\mathrm{pb}^{-1}$ collected by the CMS experiment at the LHC in the year 2010. The analysis is based on the method developed in chapter 7 to estimate the rate of the dominant reducible background processes relying only on the measurements in data. It has been performed within the CMS collaboration, in parallel with two other analyses that were based on complementary methods for background prediction. The analyses produced consistent results and have been published in [108].

In the following sections we will present the analysis strategy and main rationale behind it, the methods used to estimate the rates of all the background processes and the results obtained in the measurements from data. At the end of the chapter, we will formulate the results in a form that can be used for a model-independent comparison of measured and expected event rates and we will derive the limits on SUSY parameters in the context of the cMSSM.

8.2 Analysis strategy

There are several important properties of the SUSY models that determine the experimental characteristics of the production of same-sign di-lepton final states and that have driven our analysis strategy.

First, a large range of SUSY models predict a weakly interacting LSP in the final state of cascade decays. For this reason, a significant amount of missing transverse energy is expected to be a part of the experimental signature. The mass of the LSP sets indirectly an unknown mass scale m_C.

Second, the main production mechanism in most of these models is through the production of gluinos and squarks. The direct experimental effect is that one can expect several jets in the final state, as well as a significant production cross section. The masses of gluinos and squarks represent the second mass scale m_A that together with m_C establishes important characteristics of the final state signature.

Third, a few models expect charginos to have mass at another mass scale m_B between the masses of squarks and the LSP ,with $m_A > m_B > m_C$. In addition, charginos couple electroweakly to quarks and squarks. This fact and the given mass hierarchy directly enable cascade decays which include a single charged lepton and, consequently, allow for the production of a pair of same-sign leptons in the final state (e.g., $\tilde{q} \rightarrow \tilde{\chi}^{\pm} q \rightarrow l^{\pm} \nu \tilde{\chi}_1^0 q$).

In addition to these considerations, in case the gluino mass is at a scale significantly above the scale of quark masses, the dominant production mechanism would have been via the production of a squark-antisquark pair. This would consequently lead to production of same-sign di-leptons in final states with three or more leptons.

The three mass scales described above are inherent to the same-sign di-lepton signature and define the experimental energy scales for possible hadronic activity, lepton momenta, as well as for missing transverse energy in the final state. Indeed, energetic jets always appear in the first step of the two-step decays ($\tilde{q} \rightarrow \tilde{\chi}^{\pm} q$ or $\tilde{g} \rightarrow \tilde{\chi}^{\pm} q\bar{q}$) and determine the number of jets per decay to be a least one or two. The scale of the mass difference $m_A - m_B$ defines the scale of total amount of energy available to the production of these jets. Furthermore, given the current limits on the masses of charginos, squarks and gluinos, it can be expected for the charginos produced in the first cascade not to have extremely large boost. For this reason, the p_T of leptons produced in the chargino decay can be a reasonable estimate of the mass difference $m_B - m_C$. Finally, the scale of the missing transverse energy will have indirect dependence on the scale of the mass difference $m_B - m_C$. In the case that this mass difference is not negligible, the scale of the missing transverse energy is expected to be large.

In order to take into account all these expected experimental consequences and in order to probe distinct regions of the parameter space, it has been decided to define two sets of selection criteria for two signal regions and to apply the analysis in both of these separately.

The first selection requires two electrons with large transverse momentum and imposes a moderate requirement on the hadronic activity and the transverse missing energy in the event. It has been used in the data collected with appropriate di-electron triggers and

has been named "high-p_T selection".

The second selection requires two electrons with moderately high transverse momentum, but requires the presence of significant hadronic activity in the event. This selection has been used in the data collected with a purely hadronic trigger and has been named "low-p_T selection".

The thresholds on the hadronic activity and the transverse missing energy in the event, used to define the search regions, are chosen not only to accommodate trigger thresholds and to probe distinct regions of the parameter space, but also to both limit and diversify our exposure to the background processes from the SM.

Table 8.1: Specification of background sources and the estimation methods used for the same-sign (SS) dielectron searches.

Background	Type	Class	Estimation method
WZ, ZZ, $W^{\pm}W^{\pm}$	prompt-prompt, SS	irreducible	simulation
$t\bar{t}$, DY, $W^{\pm}W^{\mp}$	prompt-prompt, OS	reducible	charge-flip (data)
$t\bar{t}$, $W + jets$	prompt-fake, SS	reducible	T/L ratios (data)
QCD, hadronic $t\bar{t}$	fake-fake, SS	reducible	T/L ratios (data)

The background processes expected in both selections can be separated in four distinct classes. The first class consists of SM processes in which two gauge bosons are produced and lead to a pair of same sign electrons. These processes include production of the following gauge boson pairs: WZ, ZZ, $W^{\pm}W^{\pm}$ and represent an irreducible background.

The second class consists of SM processes in which a pair of top quarks ($t\bar{t}$), or neutral gauge boson and jets (DY) or a pair of oppositely charged W bosons ($W^{\pm}W^{\mp}$) are produced. These are the processes which directly lead to final states with an opposite-charged pair of prompt electrons and contribute to the signal selection region due to a non-negligible probability for the incorrect reconstruction of the electron charge.

The third and the fourth classes are SM processes in which exactly one or zero prompt electrons are produced. These two classes of processes are the dominant backgrounds in our analysis. Together with the second class, they represent the reducible backgrounds and will be estimated using only the measurements with data. The rate of events from the classes of irreducible backgrounds is very small and will be estimated using the simulation. Table 8.1 summarises in brief the classification of the main background sources and the estimation methods used for the same-sign (SS) dielectron searches.

8.3 Datasets and simulation

In order to study the performance of the analysis, a large set of Monte Carlo simulation samples with all the relevant processes have been produced and used. The samples have been first generated with either the Pythia or MadGraph event generators and processed

with a dedicated simulation of the CMS detector based on GEANT4. The signal has been modelled with a reference point from the cMSSM parameter space LM_0 which features low-mass squarks and gluinos. As a result of these low masses, the production cross-section is relatively high ($\sim 57\,$pb) and allows for the possibility of discovery with the first $35\,\text{pb}^{-1}$ of data, in case the supersymmetry exists. The mass spectrum and branching ratios used in the simulation are presented in Figure 5.3 of chapter 5. It is assumed that the processes determined by the reference point LM_0 should provide a model of the generic signal topology.

Table 8.2: List of the simulated Standard Model backgrounds and the signal sample used in the analysis.
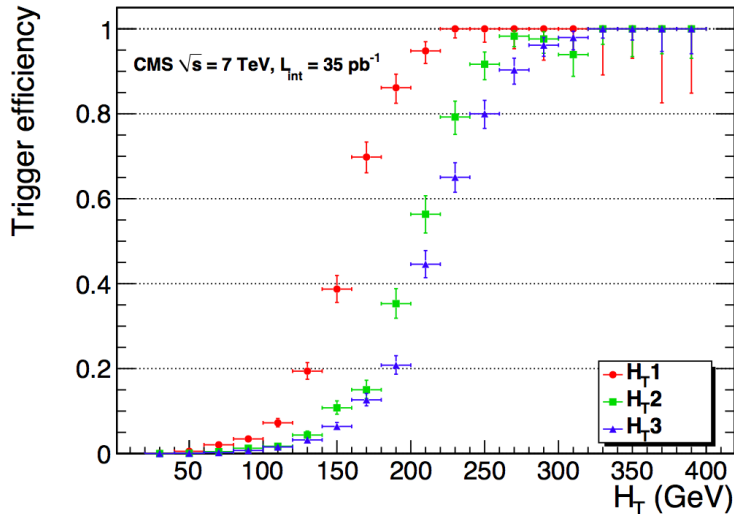
Type	description	generator	σ_{LO} [pb]	k-factor	$\mathcal{L}_{eq}$ [pb^{-1}]
QCD	$H_T \in [100, 250]\,$GeV	MadGraph	7.0×10^6	–	1.5
	$H_T \in [250, 500]\,$GeV	MadGraph	1.71×10^5	–	28.7
	$H_T \in [500, 1000]\,$GeV	MadGraph	5.2×10^3	–	805
	$H_T \in [1000, \infty]\,$GeV	MadGraph	8.3×10^1	–	2×10^3
EWK	$\gamma + \text{jets}$	MadGraph	173	–	6.28×10^3
	$W^{\pm} + \text{jets}$	MadGraph	2.42×10^4	1.2	322
	$Z^0(\gamma^*) + \text{jets}$	MadGraph	2.44×10^3	1.25	356
TOP	$t\bar{t}$	MadGraph	95	1.65	9.35×10^3
	single-t (s-channel)	MadGraph	4.21	–	9.79×10^4
	single-t (t-channel)	MadGraph	64.6	–	8.18×10^3
	single-t (tW-channel)	MadGraph	10.6	–	4.40×10^4
VV	$Z^0 Z^0$	Pythia	4.3	1.37	2.0×10^{10}
	$W^{\pm} Z^0$	Pythia	10.5	1.74	6.3×10^3
	$W^{\pm} W^{\mp}$	Pythia	28	1.53	2.9×10^3
	$W^+ W^+$	Pythia	0.188	–	5.3×10^4
	$W^- W^-$	Pythia	0.064	–	2.9×10^5
	$2 \times (qq' \to W^{\pm})$	Pythia	0.203	–	2.2×10^5
SUSY	benchmark LM_0	Pythia	38.9	1.48	3.6×10^3

All of the relevant background processes, as well as the signal reference point LM_0, are shown in Table 8.2 together with the corresponding cross sections. The cross-sections of processes generated with the cross-section computed only at leading order, are rescaled with appropriate k-factors, as shown in the table. All events from these samples have been reconstructed with the version 3.8.6 of the CMS SoftWare (CMSSW).

8.4 Event selection

In section 8.3, we have described that the rate of events of signal, background and data have been estimated within two sets of selection criteria which employ two different strategies: the high-p_T selection and the low-p_T selection.

In the case of the high-p_T selection, the events have been collected using single and di-electron triggers. The high-p_T selection requires two energetic electrons with transverse momenta above 20 and 10 GeV respectively, in order to ensure that the electron triggers are fully efficient in the selected phase space. The exact implementation of these triggers evolved throughout the 2010 data-collecting period as the LHC instantaneous luminosity was gradually increasing. Trigger efficiencies have been measured from a pure electron sample collected using $Z \to e^+e^-$ decays from the data. The averaged efficiency to trigger on events with two leptons with $|\eta| < 2.4$ and $p_T > 10$ GeV, one of which also has $p_T > 20$ GeV, has proven to be very high. The trigger efficiency for an LM_0 signal event passing the baseline selection has been estimated in simulation to be $(99 \pm 1)\%$.

Figure 8.1: The efficiency of the H_T trigger as a function of the reconstructed H_T for three periods of data taking: $H_T 1$ ($7\,\mathrm{pb}^{-1}$), $H_T 2$ ($10\,\mathrm{pb}^{-1}$) and $H_T 3$ ($18\,\mathrm{pb}^{-1}$).

The low-p_T selection effectively samples a region of parameter space where electrons have lower values of transverse momentum ($p_T > 10$ GeV), and events had to be collected using triggers with requirement on the total hadronic activity in the event. The hadronic activity of a reconstructed event is computed as the scalar sum of the transverse momenta of all the jets reconstructed in that event and denoted as $H_T = \sum_{i \in jets} p_{T,i}$. Figure 8.1 shows the measured efficiency for the H_T triggers used during the three different periods of data taking. During the period of data taking, the trigger thresholds have been updated several times in order to sustain the high rates resulting from the increasing instantaneous luminosities. Yet, approximately one half of the data has been collected in 2010 with the trigger that had the highest threshold. The measurements show that the efficiency of the trigger has been $(94 \pm 5)\%$ for the value of the selection criteria $H_T = 300$ GeV [108]. For this reason, the low-p_T selection has required the total hadronic activity in the event to be above $300\,\mathrm{GeV}$.

The high-p_T selection requires the hadronic activity and the transverse missing energy to be larger than $60\,\mathrm{GeV}$ and $80\,\mathrm{GeV}$, respectively. On the other hand, the low-p_T selection

requires the hadronic activity and the transverse missing energy to larger than $300\,\mathrm{GeV}$ and $30\,\mathrm{GeV}$, respectively.
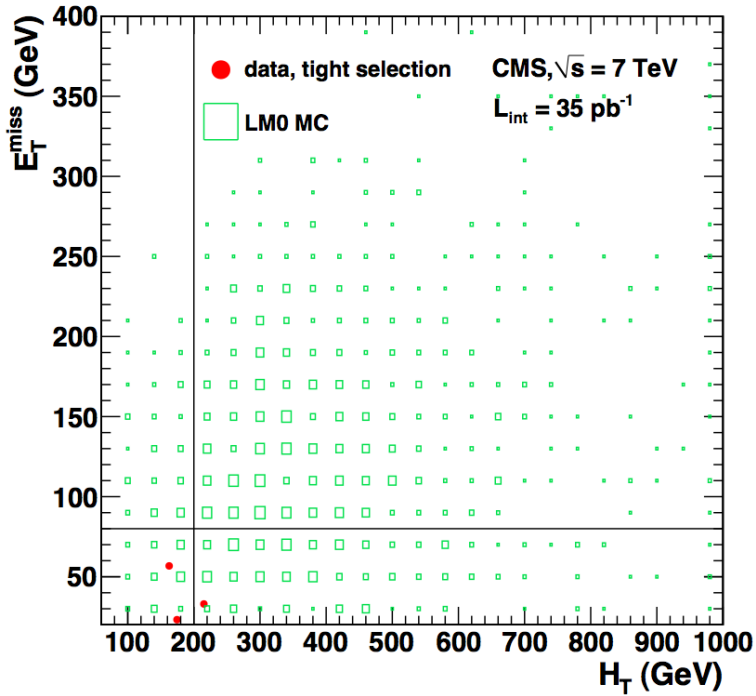
The two selections are equivalent in terms of all the other selection criteria. They require the event to have at least two jets reconstructed with the PF algorithm and passing the standard jet identification requirements. The selections also require the event to have at least two reconstructed electrons with the same charge, where both electrons pass the tight $WP80$ identification criteria and tight relative isolation criteria. The charge of the electrons is measured by three algorithms and only if the algorithms provide the same result, the electrons are selected. In addition, the invariant mass of the two selected electrons is required to be larger than $12\,\mathrm{GeV}$.

Table 8.3: Event selection criteria used in the analysis for both the high-p_T and the low-p_T selection. The detailed description of the cuts is given in the text.

Criteria name	high-p_T selection	low-p_T selection
Preselection	$N_{el}^{loose} \geq 2$	$N_{el}^{loose} \geq 2$
	$p_T^1 \geq 20\,\mathrm{GeV}, p_T^2 \geq 10\,\mathrm{GeV}$	$p_T^1, p_T^2 \geq 10\,\mathrm{GeV}$
	$M_{e_1,e_2} \geq 12\,\mathrm{GeV}$	$M_{e_1,e_2} \geq 12\,\mathrm{GeV}$
	$\Delta R(e_i, \text{any } \mu) > 0.1$	$\Delta R(e_i, \text{any } \mu) > 0.1$
	$N_{jets} \geq 2$	$N_{jets} \geq 2$
	$H_T \geq 60\,\mathrm{GeV}$	$H_T \geq 200\,\mathrm{GeV}$
	$E_{\mathrm{T}}^{\mathrm{miss}} \geq 80\,\mathrm{GeV}$	$E_{\mathrm{T}}^{\mathrm{miss}} \geq 30\,\mathrm{GeV}$
Baseline	lepton charge consistency	lepton charge consistency
	$sign(e_1) = sign(e_2)$	$sign(e_1) = sign(e_2)$
Tight(e_1)	$WP80, RelIso(e_1) < 0.1$	$WP80, RelIso(e_1) < 0.15$
Tight(e_2)	$WP80, RelIso(e_2) < 0.1$	$WP80, RelIso(e_2) < 0.15$

Table 8.3 lists all the described selection criteria for both the high-p_T and low-p_T selection. The criteria are listed in the order they are imposed in the analysis and grouped in four steps: "Preselection", "Baseline", "Tight(e_1)" and "Tight(e_2)" . e_1 and e_1 denote the electrons of the selected pair of same-sign electrons with higher and lower transverse momentum, respectively. The high-p_T selection has slightly tighter isolation requirement with respect to the low-p_T selection (specified in the table). The choice has been motivated by the study performed with the simulation that predicted a high rate of fake electrons in case of the high-p_T selection.

In case of "Preselection" and "Baseline" groups of criteria, the reconstructed electrons are required to pass only the loose $WP90$ identification criteria. In case of "Tight(e_1)" step of selection, the electron e_1 is required to pass the tight $WP90$ identification criteria and tight isolation criteria. In case of "Tight(e_2)" step of selection, also the electron e_2 is required to pass the tight $WP90$ identification criteria and tight isolation criteria. The "Baseline" and "Tight(e_1)" groups of criteria define two loose selections that define the control regions which will be used to predict the dominant part of the reducible backgrounds (described in details in section 8.6).

Figure 8.2: Scatter plot of H_T versus missing E_T. Overlay of the three observed events with the expected signal distribution for LM_0. Horizontal and vertical black lines mark the cuts on the missing E_T and the H_T used in the analysis for the high-p_T and low-p_T selection respectively.

Figure 8.2 shows the H_T versus E_T^{miss} scatter plot of the events observed in data and events simulated for the LM_0. The events are shown for the two selections, without H_T and E_T^{miss} criteria applied. The final high-p_T and low-p_T selections are then indicated by the horizontal and vertical lines, respectively. Figure 8.2 shows three events in the whole region, one of which barely satisfies the requirement $H_T > 200$ GeV, but fails the requirement $E_T^{\text{miss}} > 80$ GeV. In contrast, most of the signal from typical supersymmetry models is supposed to satisfy both of these requirements, as is illustrated by the expected distribution of the LM_0 signal events overlaid in the figure.

Table 8.4: Di-electron event yields after each cut for both simulated backgrounds and data, for luminosity of $35\,\text{pb}^{-1}$. Results are shown for the high-p_T selection.

Cut name	QCD	EWK	TOP	VV	**TOT**	LM0	**DATA**
Preselection	44.38	9.47	7.10	0.04	60.99	4.02	66
Baseline	6.32	6.29	5.31	0.04	17.96	3.30	35
Tight(e_1)	0.11	3.90	3.40	0.03	7.44	2.28	12
Tight(e_2)	0.00	0.11	0.14	0.02	0.27	1.31	0

Table 8.5: Di-electron event yields after each cut for both simulated backgrounds and data, for luminosity of $35\,\mathrm{pb}^{-1}$. Results are shown for the low-p_T selection.

Cut name	QCD	EWK	TOP	VV	**TOT**	LM0	**DATA**
Preselection	1.78	0.64	1.67	0.02	4.11	2.86	11
Baseline	1.66	0.22	1.23	0.01	3.12	2.48	6
Tight(e_1)	0.06	0.22	0.64	0.01	0.93	1.66	4
Tight(e_2)	0.00	0.00	0.03	0.01	0.04	0.99	1

The selection criteria specified in Table 8.3 have been applied both in the simulation and in the data. The event yields for the di-electron channel after each of the described selection steps are shown in the Table 8.4 and Table 8.5 for the high-p_T and low-p_T selection respectively. The event yields in the simulation are shown separately for each type of the SM background, as it has been defined in Table 8.2. The results for the other di-lepton channels can be found in [108, 109].

8.5 Estimation of irreducible backgrounds

Standard model sources of same-sign dilepton events with both leptons coming from a W or Z decay represent irreducible backgrounds for our analysis and include $qq \to WZ$ and ZZ, double W-strahlung $qq \to q'q'W^{\pm}W^{\pm}$, double parton scattering $2 \times (qq' \to W^{\pm})$, ttW, and WWW processes. These processes have not been measured in proton-proton collisions in the era prior to the LHC and we have only approximate theoretical predictions for the production cross section for these processes. Since the theoretical predictions estimate that the rate of these background processes should be very low in our selection regions, we have decided to evaluate these backgrounds using only simulation results. The systematic uncertainty on the theoretical predictions for the production cross section has been estimated to be lower than 30% [108].

Table 8.6: Di-electron event yields and systematic errors for di-boson production (WZ, ZZ, WW) in single parton scattering processes and double parton scattering $2 \times (qq' \to W^{\pm})$ processes for the luminosity $35\,\mathrm{pb}^{-1}$. The results are shown for both high-p_T and low-p_T selection. Theoretical systematic error on the production cross section is estimated to be 30% and is not included in the table.

Production process	high-p_T selection	low-p_T selection
di-boson production	0.024 ± 0.002	0.010 ± 0.001
double parton scattering	0.001 ± 0.001	0.000 ± 0.002
Total yield ($35\,\mathrm{pb}^{-1}$)	0.025 ± 0.009	0.010 ± 0.006

The results of the simulation are summarised in Table 8.6 and represent the event yields and systematic errors for di-boson production in single parton scattering processes and double parton scattering $2 \times (qq' \to W^{\pm})$ processes for the luminosity $35\,\mathrm{pb}^{-1}$. The results are shown for both the high-p_T and low-p_T selection.

8.6 Data-driven estimation of reducible backgrounds

In the previous section we have seen that the contribution of irreducible backgrounds is negligible at the integrated luminosity of about 35 pb^{-1}. For this reason, the main focus of the analysis is on the estimation of the rates of reducible backgrounds. The main component of the reducible backgrounds are the processes where at least one of the two leptons is not a prompt lepton. In order to estimate the rates for these backgrounds, we use the extended method of fake and prompt ratios which has been introduced in chapter 7. The exact application of the method, as well as its results and associated uncertainties will be presented in the next section.

Another component of reducible backgrounds are the processes with two opposite-sign electrons in the final state, where the charge of one of the two electrons has been wrongly measured. Since the isolation and identification properties of these electrons are the same as the corresponding properties of prompt electrons, we had considered this source of reducible backgrounds separately. We have estimated this background by measuring the probability of charge-misidentification in $Z \to e^+e^-$ events reconstructed in the data. The method and its results will be presented in section 8.6.2.
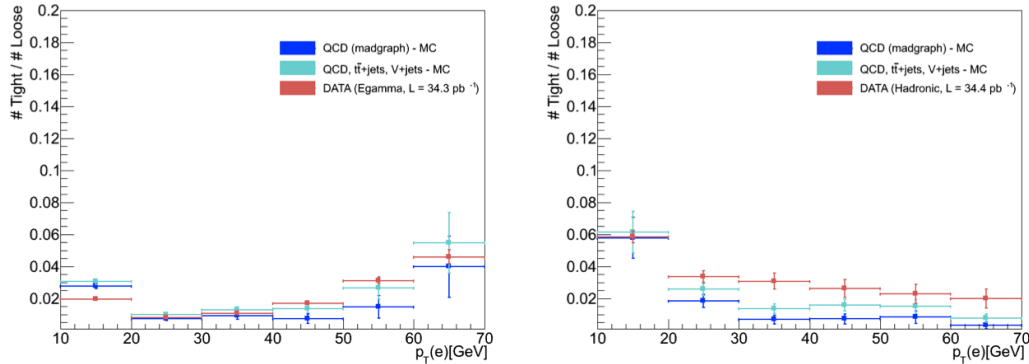
8.6.1 Background from fake and non-isolated electrons

8.6.1.1 Measurement of fake and prompt ratios

The main sources of non-prompt electrons in the analysis are jets which deposit most of the energy in the ECAL and are matched to a high p_T track (usually jets originating from light-flavour quarks), or real non-isolated electrons coming from decays of heavy-flavour mesons. The fake electrons originating from jets typically have a quite different profile of electromagnetic shower with respect to the prompt electrons, while the fake electrons coming from heavy-flavour meson decays can be distinguished from the prompt electrons by their isolation.

In order to obtain a reasonably good control on the rate of backgrounds which contain either of these fake electrons, we have defined the "loose" electron by relaxing both the requirements imposed on its isolation and the electron identification requirement. In the two selections used in the analysis we have defined "loose" electrons as those which pass the looser $WP90$ identification requirement. In addition, we have required their relative isolation to be lower than 1.0 or lower than 0.6 if the electron has been reconstructed in the barrel region or the endcap region of the ECAL. These are exactly the requirements defined as the "loose" electron selection requirements described in Table 8.3. The prompt

ratio p and the fake ratio f are than defined for all the electrons exactly as described in the chapter 7.

Figure 8.3: A fake ratio for electrons in the case of the high-p_T (left) and low-p_T (right) selection.

In oder to reliably measure the electron fake ratio in the data, we had to select a sample of events that is completely dominated by events from processes whose final states do not include prompt electrons. In addition, we wanted to select a sample of events that has similar hadronic activity as the events in our signal region. This requirement would ensure that the mechanisms which lead to the fake electrons are similar in both selections. The selection requirements used to select this sample of events were:
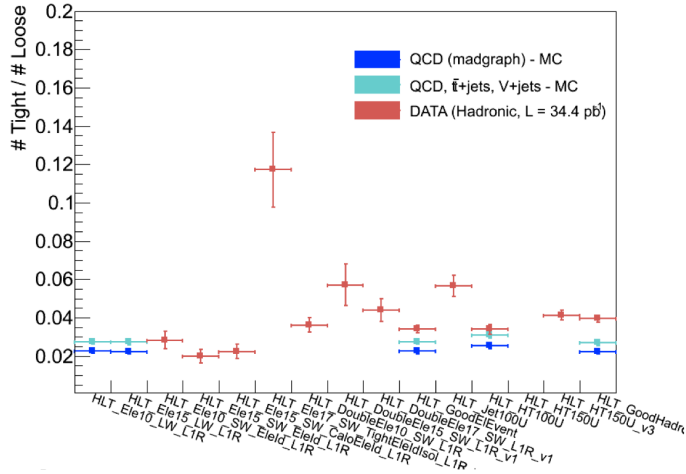
- exactly one electron that passes "loose" selection requirements;
- missing transverse energy $E_T^{\mathrm{miss}} < 50\,\mathrm{GeV}$;
- the transverse mass of the electron $M_T^e = \sqrt{(E_e + E_T^{\mathrm{miss}})^2 - (\vec{p}_e + \vec{p}_T^{\mathrm{miss}})^2} < 20\,\mathrm{GeV}$;
- at least two reconstructed jets with $p_T > 30\,\mathrm{GeV}$;
- the same HT cut as in the signal selection region ($H_T > 30\,\mathrm{GeV}$ in case of the high-p_T selection and $H_T > 300\,\mathrm{GeV}$ in case of the low-p_T selection).

The purpose of the first requirement in the list was to veto the contribution from $(Z \rightarrow e^+e^-)$+jets processes, while the purpose of the second and third requirement was to strongly suppress the contribution from $(W^\pm \rightarrow e^\pm\nu)$+jets processes. The last two requirements are imposed in order to select the sample of events that have desired hadronic activity.

The fake ratios for electrons have been measured in the data and in simulation for different momenta of the selected electrons. The measured p_T distribution of the fake ratio f is shown in Figure 8.3 for the high-p_T and low-p_T selections. It can be observed that the fake ratio decreases with the increase of the electron p_T. In case of the high-p_T selection, we can observe that for the electrons with $p_T > 50\,\mathrm{GeV}$ the fake ratio starts to increase. This effect is in part caused by the fact that the criteria used to suppress the $(W^\pm \rightarrow e^\pm\nu)$+jets processes are not efficient in this region of electron p_T. We can also
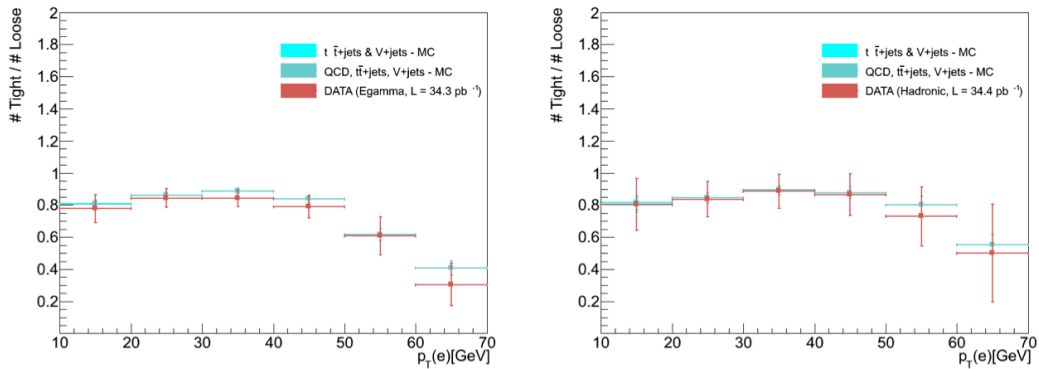
observe a reasonably good agreement between the fake ratios measured in data and in simulation for this selection. In case of the low-p_T selection, this agreement is somewhat poorer, and we can expect to observe a higher number of fake electrons in data with respect to the simulation.

Figure 8.4: The trigger bias for electrons in case of high-p_T selection.

In case of the low-p_T selection, the electron fake ratios have been measured requiring the same hadronic triggers that are used for the signal selection. Similarly, in case of the high p_T selection, the electron fake ratios have been measured requiring the same electron triggers as those used in the signal selection region. The main reason for this approach comes from the fact that several electron HLT triggers are defined with tight requirements on the electron identification and electron isolation that directly bias the effective rate of fake electrons. Figure 8.4 compares the mean values of electron fake ratios measured requiring different electron triggers and undoubtedly illustrates this effect.

Figure 8.5: The prompt ratio for electrons in the case of the high-p_T (left) and low-p_T (right) selection.

In order to reliably measure the electron prompt ratio in data, we had to select a sample of events that are dominated by $(Z \rightarrow e^+e^-)$+jets processes. We also wanted to
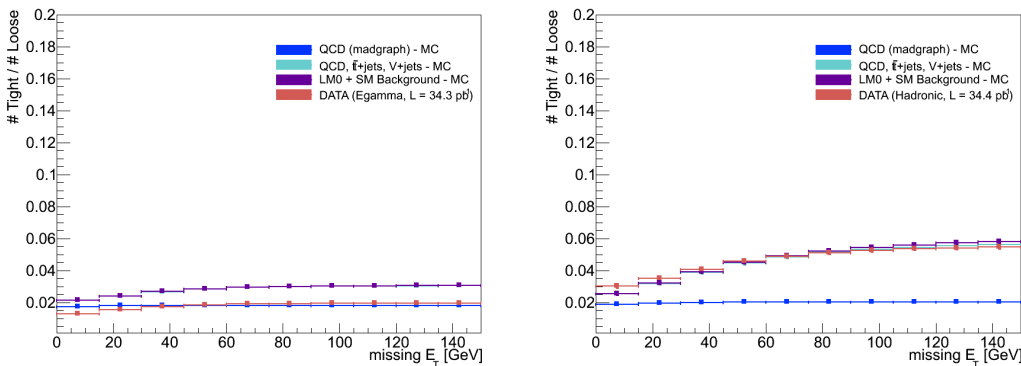
select a sample of events that has similar hadronic activity as the events in our signal region. The selection requirements used to select this sample of events were:

- exactly two "loose" electrons with opposite charge and the invariant mass consistent with the mass of the Z boson $|M_{inv}(e_1, e_2) - M_Z| < 15$ GeV;

- the missing transverse energy $E_T^{miss} < 20$ GeV;

- at least two reconstructed jets with $p_T > 30$ GeV;

Table 8.7: Fake and prompt ratios for electrons compared between data and simulation, for both high-p_T and low-p_T event selections, corresponding to an integrated luminosity of $35\,\text{pb}^{-1}$.

T/L ratio	high-p_T selection	low-p_T selection
fake ratio (simulation)	0.0224 ± 0.0002	0.0309 ± 0.0017
fake ratio (data)	$0.0185 \pm 0.0002 \pm 0.0027$	$0.0398 \pm 0.0018 \pm 0.0065$
prompt ratio (simulation)	0.8925 ± 0.0098	0.8740 ± 0.0145
prompt ratio (data)	$0.8482 \pm 0.0100 \pm 0.0031$	$0.8721 \pm 0.0168 \pm 0.0053$
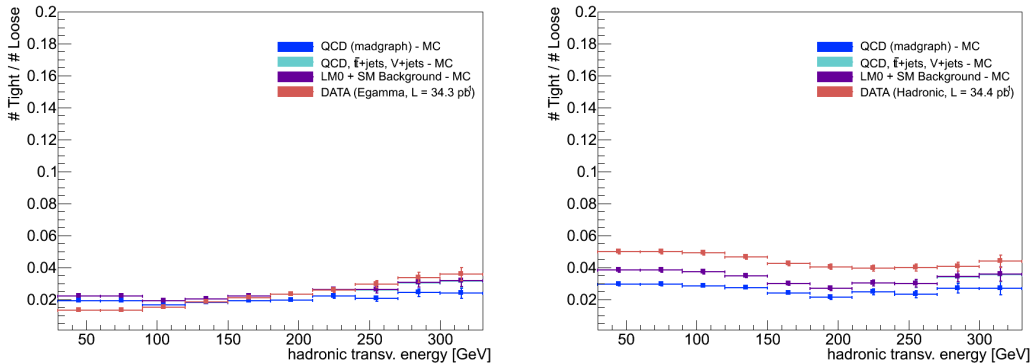
The purpose of the first requirement was to enrich the sample with events from $(Z \to e^+e^-)$+jets processes, while the purpose of the second requirement was to suppress the contribution from $(W^\pm \to e^\pm\nu)$+jets processes. The requirement is imposed in order to select a sample of events that have the desired hadronic activity. The prompt ratio is then measured in the selected sample for the harder of the two electrons.

Figure 8.6: The stability of the measured fake ratio f versus the maximal allowed E_T^{miss} in case of high-p_T (left) and low-p_T selection (right).

The prompt ratios for electrons have been measured in the data and in simulation for different momenta of the selected electrons. The measured p_T distribution of the prompt ratio p is shown in Figure 8.5 for the high-p_T and low-p_T selections.

The results for the average fake and prompt ratios for electrons measured in the data and in simulation for the high-p_T and low-p_T selections are summarised in Table 8.7. In case of measurements in data the quoted uncertainty is statistical only. In case of measurements based on simulation, the first uncertainty is statistical while the second one is the systematic uncertainty. This systematic uncertainty has been inferred from the discrepancy between the measured ratios and "true" ratios in the simulation, in the signal selection region. The origin of this discrepancy is twofold. A first part of the discrepancy is coming form the fact that even within the same type of background processes, the sources of fake electrons have slightly different properties in the sample where we measure the fake ratios with respect to the signal selection region. The other part arises from the fact that the relative compositions of the irreducible backgrounds differ in the sample where we measure the fake ratios with respect to the signal selection region. The total uncertainty on the measured fake ratios will be the major source of the uncertainty of the prediction method.

Figure 8.7: The stability of the measured fake ratio f versus the H_T cut in case of high-p_T (left) and low-p_T selection (right).

We have also studied the stability of the fake ratios with respect to the different requirements used to select the sample where we measure the fake ratios. We have tested the fake ratios against the different requirements on the missing transverse energy E_T^{miss} and, separately, on the amount of hadronic activity H_T. The results of these two tests are shown in Figure 8.6 and 8.7, respectively. Figure 8.6 represents an excellent illustration and motivation for the strict requirement on the missing transverse energy. The contribution of electroweak processes, especially $(W^\pm \to e^\pm \nu)$+jets processes, is visible in the case of the high-p_T selection where the fake ratio is measured with the $H_T > 300\,\mathrm{GeV}$ requirement.

8.6.1.2 Results and associated uncertainties

The expected yields of events from the data at 35 pb^{-1} do not favour a fully differential prediction of the rate of reducible backgrounds with fake leptons. For this reason, the pre-

diction results have been obtained using the averaged prompt and fake ratios, integrated over the whole lepton acceptance.

Table 8.8: The di-electron event yields for tight-tight (N_{t2}), tight-loose (N_{t1}) and loose-loose (N_{t0}) pairs of electrons, as well as predictions of prompt-prompt (N_{pp}), prompt-fake (N_{pf}) and fake-fake (N_{ff}) contributions in the signal region for high-p_T and low-p_T event selections, corresponding to integrated luminosity of $35\,\mathrm{pb}^{-1}$.

di-electron events	high-p_T selection	low-p_T selection
loose-loose yield (N_{t0})	23	2
tight-loose yield (N_{t1})	12	3
tight-tight yield (N_{t2})	0	1
estimated fakes in N_{t2}	$0.16 \pm 0.05 \pm 0.01$	$0.11 \pm 0.07 \pm 0.06$

The resulting predictions obtained from data for both high-p_T and low-p_T event selections are summarised in Table 8.8. The first three rows in the Table represent the number of dielectron events observed in data, with zero, with one or with two "tight" electrons. These numbers correspond to the numbers N_0, N_1 and N_2 used in the method for background prediction introduced in chapter 7. The forth row represent the prediction of the method for the rate of events from the backgrounds with fake electrons. The uncertainty of the predictions is dominated by the statistical uncertainty. This is especially pronounced in the case of the low-p_T selection where one event has been observed in data.

8.6.2   Background from electron charge mis-identification

Di-lepton events from standard model processes, such as the fully leptonic decays of $t\bar{t}$, Z+jet and $W^{\pm}W^{\pm}$, can be a background for same-sign di-lepton studies in cases when the charge of one of the electrons is incorrectly identified.

The rate of events from this type of background processes can be estimated using the measurements in data. First, we can measure in data the probability of electron charge misidentification using the events from $(Z \rightarrow e^+e^-)$+jets processes. Afterwards, we can measure the total number of events with a pair of opposite-sign electrons in the signal region. From this number we can directly estimate the rate of this type of background events.
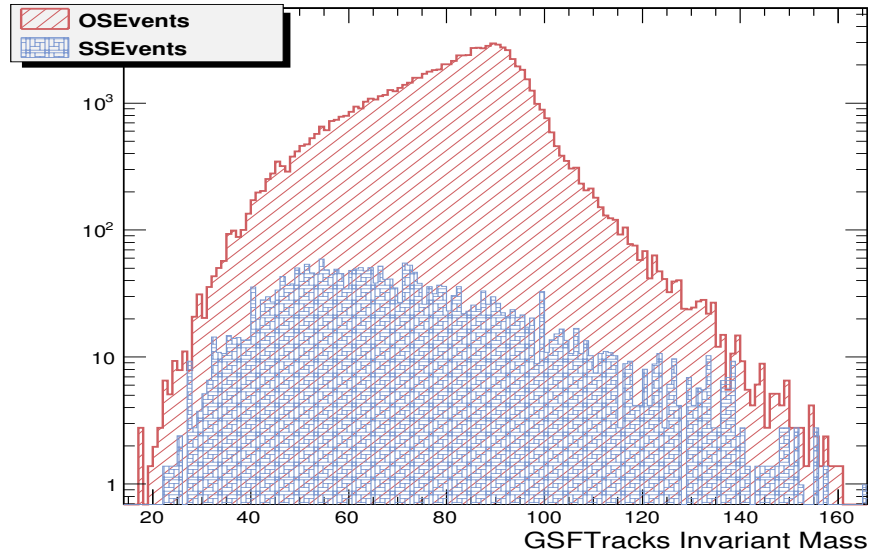
In the analysis, the sample of events dominated with events from $(Z \rightarrow e^+e^-)$+jets processes has been selected using the same selection requirements that have been used to select the sample where we have measured prompt ratios for the electrons. In addition, we require both of the electrons to pass the "tight" selection.

In order to reliably measure a probability of electron charge misidentification in data, we had to select a sample of events that are dominated by $(Z \rightarrow e^+e^-)$+jets processes. In addition, we wanted our selection to be independent of the tracker information, the

subsystem by which the charge can be misidentified. The selection requirements used to select this sample of events were:

- exactly two "tight" electrons regardless of the sign of charge;

- the modified invariant mass calculated only using the information about the energy and position of the electron supercluster has to be consistent with the mass of the Z boson $|M_{inv}^{sc}(e_1, e_2) - M_Z| < 30$ GeV;

- the missing transverse energy $E_T^{miss} < 20$ GeV;

The importance of being independent of the tracker information is illustrated in Figure 8.8. This Figure shows the distribution of invariant mass of the GSF tracks of the electrons, for same-sign and opposite-sign events originating from simulated $(Z \to e^+e^-)$+jets processes. As it shows, the peak of the invariant mass of the same-sign events (blue) is much broader than the peak of invariant mass of opposite-sign events (red). Thus, the standard invariant mass would bring a poor performance in the method.
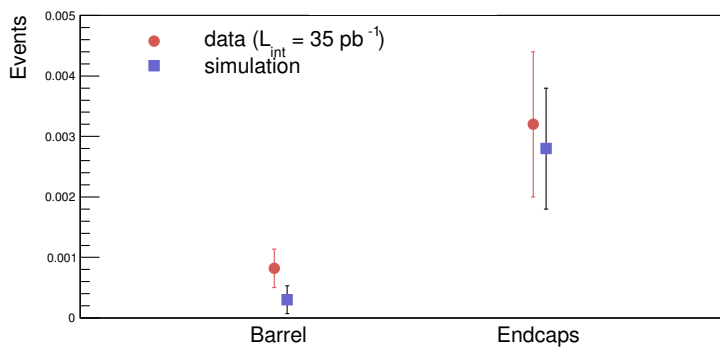
Figure 8.8: The invariant mass of the GSF tracks of electrons, for same sign and opposite sign events in MC [109].

After the sample has been selected, we have separated it into a sample with only same-sign electrons and a sample with opposite-sign electrons. Now, if we assume that the events with pairs of same-sign electrons originate from the $(Z \to e^+e^-)$+jets processes in which charge of one electron has been misidentified, the probability of the misidentification $p_{c.m.m}$ can be estimated as:

$$p_{c.m.m} = \frac{N_{SS}}{2(N_{SS} + N_{OS})} \tag{8.1}$$

where N_{ss} is the number of events with same-sign electrons and N_{os} is the number of events with opposite-sign electrons in the selected sample.

The described procedure has been applied in data and in simulation, and the probability of electron charge misidentification has been estimated. Figure 8.9 shows the estimated values of this probability separately for the barrel and endcap region of the ECAL. It can be observed that the agreement between the data and the simulation is reasonably good. The average probability of electron charge misidentification, integrated over the whole electron η acceptance region, has been estimated to be 0.0014 ± 0.0003 where the uncertainty is driven by the low statistical accuracy.

Figure 8.9: Probability of charge flip, in barrel and endcap after applying all of the cuts.

The contribution of processes with intrinsic two opposite-sign prompt electrons to the opposite- sign and same-sign tight dielectron samples can be estimated as:

$$N_{t2}^{OS} = [(1 - p_{c.m.m})^2 + p_{c.m.m}^2]N_{pp}^{OS} \qquad (8.2)$$

$$N_{t2}^{SS} = [2(1 - p_{c.m.m})p_{c.m.m}]N_{pp}^{OS} \qquad (8.3)$$

where $p_{c.m.m}$ is the measured probability of electron charge mis-identification, N_{t2}^{OS} is the number of observed opposite-sign pairs of tight electrons, N_{t2}^{SS} is the number of observed same-sign pairs of tight electrons and N_{pp}^{OS} is the number of intrinsic two opposite-sign prompt electron pairs which pass all the tight selection requirements except the charge identification.

Therefore, the contribution of these types of background processes to the same-sign electron signal region can be estimated by measuring the yield in the sample of events with a pair of opposite-charge tight electrons as:

$$N_{t2}^{SS} = \frac{2(1 - p_{c.m.m})p_{c.m.m}}{(1 - p_{c.m.m})^2 + p_{c.m.m}^2}N_{t2}^{OS} \approx 2p_{c.m.m}N_{t2}^{OS} \qquad (8.4)$$

We have estimated the number of background events due to charge misidentification by scaling the opposite-sign yields by the above probability function. Table 8.9 shows the integrated numbers for the probability of electron charge mis-identification, yield

Table 8.9: Measured probability of a charge flip for electrons, event yields for the analysis with a pair of opposite-sign electrons and the data-driven prediction of the rate of events where the charge of one of these is mis-reconstructed. The results are shown for the luminosity $35\,\mathrm{pb}^{-1}$, for both high-p_T and low-p_T selection.

Process	high-p_T selection	low-p_T selection
charge mis-id probability	0.0014 ± 0.0003	0.0014 ± 0.0003
Yield of opposite-sign electrons	5	17
Expected rate of same-sign electrons	0.007 ± 0.002	0.024 ± 0.007

for the opposite-charge tight di-electron selection and prediction for the contribution of these channels to the same-sign electron search channels, all measured in data. We have estimated the background due to electron charge misidentification to be 0.007 ± 0.002 and 0.024 ± 0.02 for the high-p_T selection and for the low-p_T selection, respectively. Based on the studies with simulation, we have assigned a 50% systematic uncertainty on the estimated backgrounds due to electron charge mismeasurement.

8.7   Results and discussion

In the two previous sections we have described the analysis methods for the estimation of the rates of all the SM background processes in high-p_T and low-p_T signal selection regions. The dominant reducible background rates have been estimated using measurements in data, while the irreducible backgrounds have been estimated from simulation.
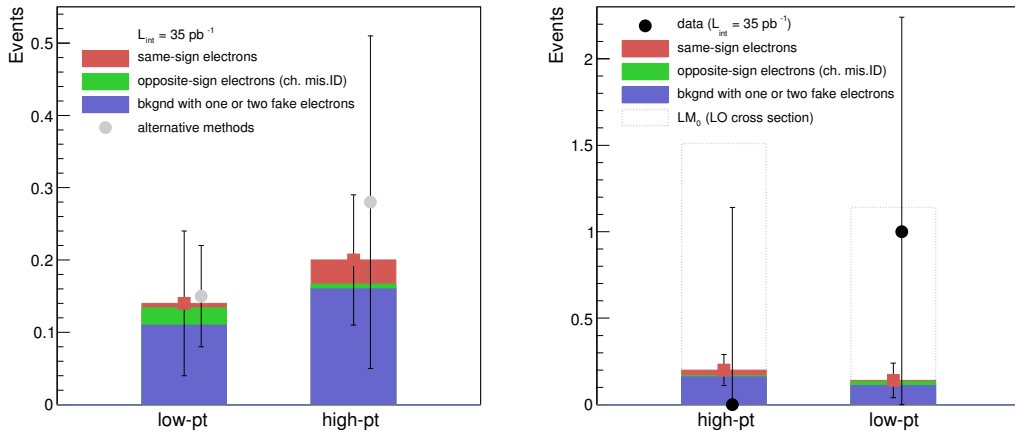
The plot on the left side of Figure 8.10 summarises all the results. It shows the composition of the background and the expected number of background events estimated by the methods described above. The reducible background from events with one or two fake electrons clearly dominates, and approximately amounts to 80% of the total expected background. In the case of the high-p_T signal selection, the SM processes with intrinsic same-sign electrons constitute about 12% of the background. On the other side, in the case of the low-p_T signal selection, the SM processes with intrinsic opposite-sign electrons constitute about 17% of the background.

Uncertainties on the background predictions include statistical and systematic uncertainties added in quadrature. Estimates based on the measurements in data have a statistical uncertainty of 25% and 57% for high-p_T and low-p_T signal selection respectively, while the systematic uncertainty is about 40% for both of these selections.

Figure 8.10 (left) also shows the results for the expected number of background events obtained by two alternative methods used in CMS [108]. The methods are complementary to the methods presented in this thesis. Each of the two alternative methods was dedicated to the prediction of backgrounds in only the high-p_T or only the low-p_T signal selection. We can observe a very good level of agreement between all the methods.

We have observed no events in case of the high-p_T selection and one event in case

of the low-p_T selection. Figure 8.10 (right) compares the observed number of events in data with the expected number of background events estimated by the methods of this analysis. The figure also includes as a reference the number of signal events predicted by simulation for the LM_0 SUSY scenario.

Figure 8.10: A visual summary of the composition of the background and the expected number of background events estimated by the method described in the text and by the alternative methods used in CMS (left). The observed and the expected number of background events estimated by the method described in the text, including the number of signal LM_0 events predicted by simulation (right). Results are shown for both the high-p_T and low-p_T selection regions.

8.7.1 Interpretation of the results

The interpretation of the experimental results from searches for supersymmetric particles or other physics phenomena depends to a certain level on the realisation of a particular physics model.

In order to draw a meaningful conclusion about the simulated SUSY model LM_0, we need to know the uncertainty related to the total efficiency of the selection of this particular signal in the search region. This uncertainty includes the uncertainties in the efficiencies of electron identification (3%), electron isolation (5%), as well as uncertainties in the efficiencies of electron triggers (1%) and hadronic triggers (5%) used in the analysis [108]. The uncertainties in the acceptance due to the modelling of initial- and final-state radiation and knowledge of the parton density functions were also included and were estimated to be 2% [108]. For the latter, the CTEQ6.6 [110] parton density functions and their uncertainties have been used. The systematic uncertainty on the measurement of luminosity delivered by the LHC has been estimated to be 4% [23]. The overall uncertainty also includes an uncertainty on the efficiency of signal selection due to the uncertainty in

the hadronic energy scale, which has been estimated to be 5% at CMS [99, 111]. These uncertainties together give rise to a total uncertainty on the signal efficiency of 12% and 15% for the high-p_T and low-p_T selection, respectively.

As there has been no evidence of an event yield in excess of the background prediction, we have set the 95% CL upper limits on the number of signal events using a Bayesian method with a flat prior on the signal strength and log-normal priors for the background and efficiency uncertainties discussed above [88]. The resulting upper limits are 3.2 events and 4.4 events in case of the high-p_T and low-p_T signal regions, respectively. The results are presented in the Table 8.10.

Table 8.10: Observed events in data and estimated background yields for both high-p_T and low-p_T selection. Estimated background include the sum of the data-driven estimates of the fake electron contributions and the residual contributions predicted by the simulation. The observed upper limits (CL@95%) on the yields and on the ($\sigma \times BR \times A$) for events from physics beyond SM are shown in bold.

Event yield	high-p_T selection	low-p_T selection
Estimated background	$0.20 \pm 0.05 \pm 0.08$	$0.14 \pm 0.08 \pm 0.06$
Estimated background (other methods)	0.28 ± 0.23	0.15 ± 0.07
Observed in data	0	1
Upper limit on signal yield	**3.2**	**4.4**
Upper limit on ($\sigma \times BR \times A$)$_{\text{signal}}$	**0.26 pb^{-1}**	**0.35 pb^{-1}**

The production cross-section σ_{signal} and the branching ratios BR_{signal} for particular signal processes depend on the model of interest. The "theoretical" efficiency of the selection criteria used in the analysis, commonly named as the experimental acceptance A_{signal}, depends also on the model of interest. On the other hand, the overall efficiency of the selection criteria depends on the particular properties and performance of the experiment as $A_{\text{signal}} \times \epsilon_{signal}^{exp}$. For this reason, it is instructive to decouple the dependence on the experiment performance, and to also compute the limits on the ($\sigma \times BR \times A$)$_{\text{signal}}$, which should be applicable to a wide range of models.
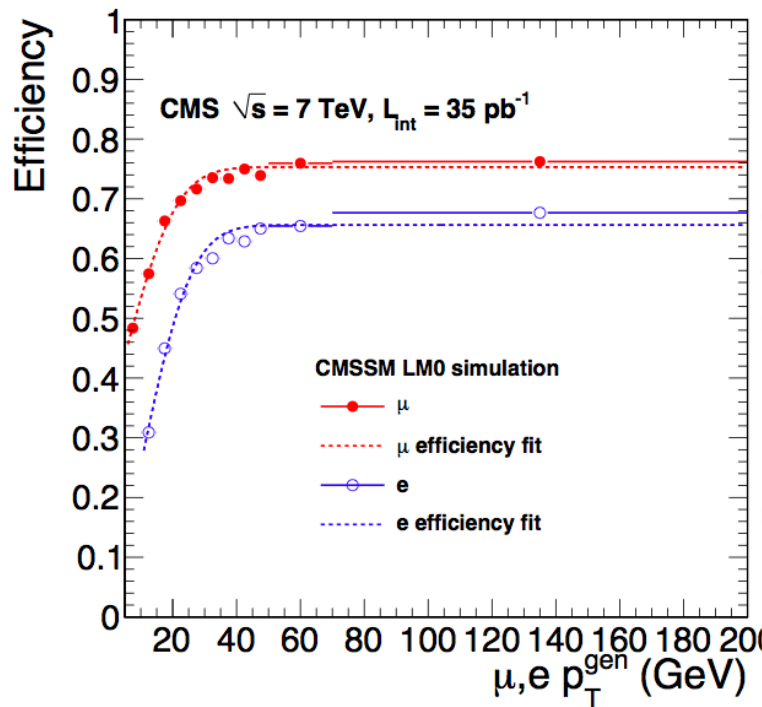
In case of the simulated LM_0 model, we have obtained the upper limits of 0.26 pb^{-1} and 0.35 pb^{-1} on the ($\sigma \times BR \times A$)$_{\text{signal}}$, for the high-$p_T$ and low-p_T selection regions respectively. These results are included in Table 8.10.

8.7.2 Model independent exclusion limits

In order to convey information in a form that can be used to test a wide range of physics models, it is necessary to provide parameterisations that can allow one to calculate the experimental acceptance for any signal model with arbitrary distributions of the observables used in the analysis. In this section we present additional information that can be used to confront models of new physics in an approximate way by generator level simula-

tion studies that compare the expected number of events in $35\,\mathrm{pb}^{-1}$ with our upper limits shown in Table 8.10.

The key information are kinematic selection variables and their properties for each of the two signal regions. At the generator level, the H_T variable can be approximated by defining it as the scalar sum of the p_T of all final-state quarks and gluons with $p_T > 30\,\mathrm{GeV}$ produced in the hard-scattering process. In a similar way, the E_T^{miss} can be computed as the magnitude of the vector sum of the transverse momentum over all non-interacting particles, such as neutrinos and LSP. It has been found that the ratio of the mean detector responses for H_T and E_T^{miss}, as defined above, to their true values are 0.94 ± 0.05, and 0.95 ± 0.05, respectively, where the uncertainties are dominated by the jet energy scale uncertainty. The resolution on E_T^{miss} depends on the total hadronic activity in the event and has been measured in data to vary from about 7 to 25 GeV for events with H_T in the range of 60 to 350 GeV. On the other side, the H_T resolution decreases from about 26% at 200 GeV to 19% for 300 GeV. The H_T resolution has been measured in simulation using the LM_0 reference model. The details on these results can be found in [108] and references therein.

Figure 8.11: Selection efficiencies for electrons and muons as a function of p_T in the LM_0 as a reference model. The results of the fits described in the text are shown by the dotted lines [108].

Providing information on lepton reconstruction, isolation and selection efficiencies is another important step, due to the fact that these largely depend on the lepton p_T, lepton η and detector properties. Figure 8.11 shows the efficiency versus p_T in the LM_0

reference model for electrons and muons. The efficiencies have been fitted with the curves of the functional form: $\epsilon(p_T) = \epsilon_{max} + C_1 \times [\text{erf}((p_T - p_T^{cut})/C_2) - 1]$, where p_T^{cut} is the corresponding selection criteria on the p_T. For the parameters $(\epsilon_{max}, C_1, C_2)$ the values of (66%, 40%, 18) and (75%, 32%, 18) have been obtained for e and μ used in the analysis, respectively.

Unfortunately, some of the event topologies (e.g. events with significantly boosted top quarks) can influence the isolation efficiency significantly and are difficult to model at generator level[108]. For this reason, the results of this particular analysis can not easily be interpreted in new physics models with such characteristics. Instead, a detailed detector simulation has to be performed in these cases.
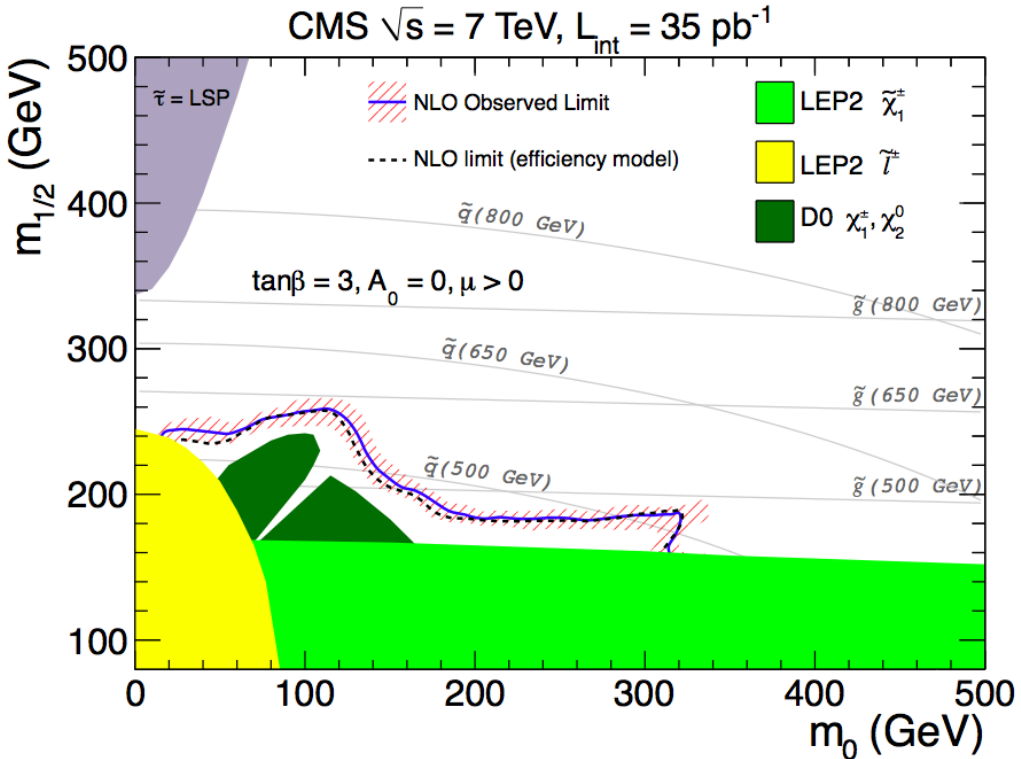
8.7.3 Exclusion limits in the cMSSM parameter space

The experimental results from SUSY searches are often presented within the parameter space of a specific SUSY model. This approach has the advantage that specific SUSY models can be confronted with constraints coming from the other direct or indirect experimental searches, such as limits from flavour physics and electroweak precision measurements.

Figure 8.12 shows the results in the plane of m_0 and $m_{1/2}$ parameters of the cMSSM, with other parameters fixed to: $\tan\beta = 3$, $A_0 = 0$ GeV and $\mu > 0$. These results are based on the three complementary analyses performed by the CMS collaboration and published in [108] (including this analysis). The particle spectrum of the model has been calculated using SoftSUSY [112], along with sparticle decay using SDECAY [113]. The signal events have been generated with PYTHIA 6 [114] using CTEQ6M [115].

In Figure 8.12, the continuous blue line represents the exclusion contour based on the observed limits. The width of the red shaded band around the blue line indicates uncertainties in the NLO cross section calculation. These include variations of the PDF and simultaneous variation by a factor of two of the renormalization and factorization scales. Both effects have been added in quadrature. In order to validate the simple efficiency model described above, we also show the results based on this model in the figure (black dotted line). The level of precision based on such a simple efficiency model is remarkably good. It can also be seen that the theoretical uncertainties on the observed limits are larger than the imperfections in the simple parameterised-efficiency model described above.

The particular cMSSM model has been chosen because it provides a common reference point for comparison with previously published Tevatron results [90, 91]. In Figure 8.12, the Tevatron results are shown as dark green exclusion region. The light green and yellow exclusion regions are based on the results from direct searches for sleptons and charginos at LEP. It can be clearly observed that the exclusion regions for this particular cMSSM model have been extended with respect to the previous searches, although the analysed data sample only corresponds to $35\,\text{pb}^{-1}$ of integrated luminosity. The key reason is that the cross section for the production of squark-squark and, especially, gluino-gluino pairs is much larger at the LHC than at the Tevatron, as we have discussed in chapter 5.

Figure 8.12: Exclusion contour in the $(m_0, m_{1/2})$ plane for the cMSSM model according to the search result in $35\,\mathrm{pb}^{-1}$ of data collected in year 2010. Comparing the width of the red shaded band (theoretical uncertainty) with the difference between the solid blue and dashed black curves shows that the imperfections in the simple efficiency model described in the text are small compared to the theoretical uncertainties. The results are based on the three complementary analyses performed by the CMS collaboration and published in [108] (including this analysis).
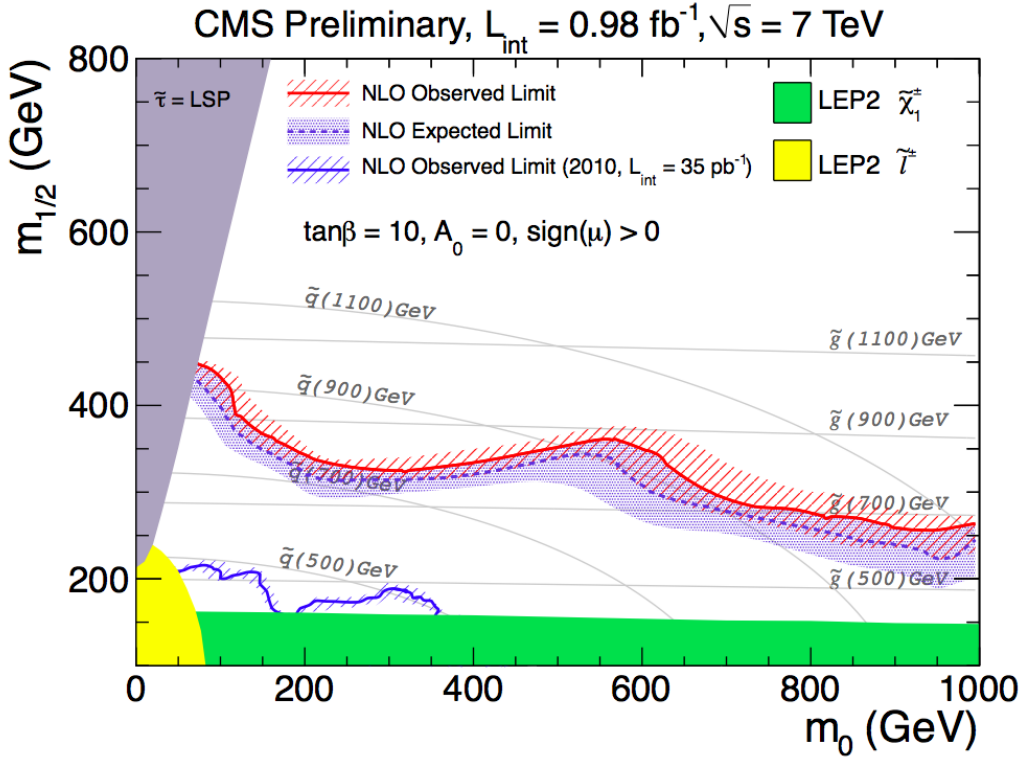
8.7.4 Strategy for the future searches

It is expected that the LHC will deliver the integrated luminosity of about $5\,\mathrm{fb}^{-1}$ until the end of the operation in 2011, and up to $30\,\mathrm{fb}^{-1}$ until the end of the operation in 2012 [20]. This corresponds to a potential increase of 2-3 orders of magnitude in the integrated luminosity available to the experiments, thus offering huge benefits to a large number of physics analyses.

The search for physics beyond the SM in events with a pair of same-sign electrons and the analysis methods presented in this thesis could clearly profit from this increase. In particular, the larger data sample could help decrease the statistical uncertainty which is currently as large as the systematic uncertainty of the method.

In order to take the advantage of the larger data sample expected in 2011 and 2012, the analysis will have to be able to cope with two problems. First, an increase in the instantaneous luminosity of the LHC will necessarily lead to an increase of the number

of pile-up events per bunch crossing, as it has been discussed in chapter 1. The average number of pile-up events per bunch crossing is expected to rise from about 2-3 in 2010, to about 25-30 during 2012. In order to cope with this effect, special methods will have to be applied.

Figure 8.13: Exclusion contour in the $(m_0, m_{1/2})$ plane for the cMSSM model according to the search with $1\,\mathrm{fb}^{-1}$ of data collected in year 2011. The plot illustrates the overall improvements because of a better statistical accuracy and refinement of the data analysis methods [116].

During the year 2011, the CMS collaboration has developed common methods to tackle this problem in the case of collisions with a the time gap between two consecutive bunch crossings of $50\,\mathrm{ns}$. The methods have proven to be successful and have shown good performance [117]. But, they might have to be adjusted in order to cope with the pile-up from collisions with a time gap between bunch crossings of $25\,\mathrm{ns}$, as it is expected in 2012. The search for physics beyond the SM presented in this thesis has been performed again in 2011, reinforced with the methods that make the analysis practically insensitive to the pile-up effects. The results obtained with the data sample of about $1\,\mathrm{fb}^{-1}$ are illustrated in Figure 8.13 [116]. The figure shows the exclusion contours in the $(m_0, m_{1/2})$ plane for the cMSSM model for both the analysis performed with a data sample of $35\,\mathrm{pb}^{-1}$ in 2010 and the analysis performed a with data sample of $0.98\,\mathrm{fb}^{-1}$ in 2011. It illustrates without doubt the overall improvement in the observed limits arising directly from a better statistical accuracy. The analysis results have also been presented at the EPS Conference

on High Energy Physics held in Grenoble, France in 2011 [118].

The second problem that this analysis will have to cope with are the systematic uncertainties of its method. It is expected that these uncertainties will limit the overall performance of the analysis in its current form with a data sample of about $5\,\text{fb}^{-1}$ and larger. The main source of these systematic uncertainties are the uncertainties in the estimation of the background from processes with one or two fake leptons. In chapter 7, we have discussed that the main part of these uncertainties arise from the fact that the same fake ratios are used for two different classes of background processes. The method developed and explained in the same chapter offers a way to separately handle different classes of backgrounds and to reduce a part of the systematic uncertainties. We expect that with the data samples larger than $5\,\text{fb}^{-1}$ it will be possible to employ this method and to improve the overall performance of the search for physics beyond the SM in events with a pair of same-sign electrons.

Conclusions

Good tests kill flawed theories; we remain alive to guess again.
Sir Karl Raimund Popper[1]

Over the course of two decades the community of scientists and engineers from institutes and universities from all over the world had been developing and constructing the LHC and its experiments. The LHC has finally started its operation in the year 2010 and today it successfully provides its experiments with enormous amounts of data offering an unprecedented potential for the search for physics phenomena beyond the SM.

In order to fully exploit this potential, complex experiments with a large number of sophisticated subsystems had to be designed and constructed. An example of such a sophistication is the Detector Control and Safety System for the Electromagnetic calorimeter of the CMS experiment. In the first part of this thesis we have presented our work on the development of the system, testing of its prototypes, implementation of the distinctive solutions and the commissioning and operation of the system within the CMS experiment. Some of the noteworthy solutions include the development of the redundant hardware system for the sensor readout and the development of the dedicated ESS communication protocol.

The CMS experiment is a state of the art tool needed to study the physics of particle interactions at energies of a few TeV and to test if there is any evidence of new physics phenomena. In the second part of this thesis, we have presented the motivation for this type of tests and studies and why SUSY represents one of the interesting extensions of the SM. We have also presented the full physics analysis performed in the year 2010 with the goal to search for physics beyond the SM in events with a pair of same-sign electrons. The analysis was part of a wider analysis effort undertaken by the CMS collaboration. We have observed no excess over the expected number of events in the signal region and the combined results of the CMS analyses have enabled to set new limits on the theoretical models for physics beyond the SM. In the case of the constrained MSSM, we have extended the limits imposed by the previous indirect and direct SUSY searches. We have also developed, together with other colleagues from ETH, an extended experimental method for the prediction of rates of background processes with one or more fake leptons that provides a scheme for handling different types of backgrounds independently. We are enthusiastic to see what kind of new results this method and this analysis will bring in the years to come.

---

[1]K. R. Popper (1994), unsourced

Acknowledgments

I would like to express special thank to several colleagues and friends that have made this work inspiring and unforgettable experience.

First, I would like to deeply thank my supervisor Günther Dissertori for valuable scientific guidance and constant support he has provided me over many years of research. I am especially grateful for he has provided me with an exceptional opportunity to work in CERN for a few years on one of the most complex projects mankind has undertaken. This has given me a chance to satisfy my curiosity both in fundamental physics research and in engineering aspects of large scale experiments.

I owe enormous gratitude to Petar Adžić for many years of tireless support in various aspects of my professional life. I am also grateful to him for the opportunity to work in CERN.

Next, I would like to thank my colleagues Frederic Ronga and Filip Moortgat for numerous discussions and for being ready to help me with suggestions and advices at any moment. Special thanks also goes to Luc Pape and Daniel Treille for their immense knowledge and countless wise ideas concerning phenomenology of particle physics. Important thank goes to all the colleagues I have directly collaborated with on scientific publications, in particular: Benjamin Stieger, Hamed Bakhshian and Alicia Calderon Talon.

I also wish to acknowledge the members of the ECAL teams for contributing to my work in various ways. I would especially like to mention Werner Lustermann who taught me a lot of useful ways to approach problems in applied physics.

Further I would like to credit all the members of the CMS Belgrade group, especially my friends and colleagues Nebojsa Smiljković and Dragoslav Jovanović.

I would also like to thank all the former and present co-workers and friends in the HEP group of the IPP at CERN: Fabian, Kostas, Pascal, Ann-Karin, Thomas, Wieland, Carmelo for many fruitful discussions and entertaining time we spent together .

The most of all, I would like to express my gratitude to my family whose encouragement helped me to stand through the frequent periods of long work hours and for supporting me throughout all of my studies.

List of Figures

List of Tables

143

Acronyms

AC	**A**ccess **C**ontrol
ADC	**A**nalog **D**igital **C**onverter
ALICE	**A** **L**arge **I**on **C**ollider **E**xperiment
APD	**A**valanche **P**hoto **D**iode
API	**A**pplication **P**rogram **I**nterface
ATLAS	**A** **T**oroidal **L**hc **A**pparatu**S**
CALO	**Calo**rimeter
CAN	**C**ontroller **A**rea **N**etwork
CDF	**C**ollider **D**etector at **F**ermilab
CERN	**C**onseil **E**uropéen pour la **R**echerche **N**ucléaire
CMS	**C**ompact **M**uon **S**olenoid
CSC	**C**athode **S**trip **C**hambers
DØ	A multi purpose detector at Tevatron
DB	**D**ata**b**ase
DBS	**D**ata**b**ase **S**ystem
DCS	**D**etector **C**ontrol **S**ystem
DCU	**D**etector **C**ontrol **U**nit
DIM	**D**istributed **I**nformation **M**anagement
DIP	**D**ata **I**nterchange **P**rotocol
DP	**D**ata **P**oint

DT	**D**rift **T**ube
DU	**D**evice **U**nit
ECAL	**E**lectromagnetic **C**alorimeter
EB	**ECAL B**arrel
EE	**ECAL E**ndcap
ELMB	**E**mbedded **L**ocal **M**onitor **B**oard
ESS	**ECAL S**afety **S**ystem
FIFO	**F**irst **I**n **F**irst **O**ut
FSM	**F**inite **S**tate **M**achine
HB	**H**adronic Calorimeter **B**arrel
HCAL	**H**adronic **C**alorimeter
HE	**H**adronic Calorimeter **E**nd-Cap
HF	**H**adronic Calorimeter **F**orward
HIGLU	A program for the calculation of the total Higgs production cross section at hadron colliders via gluon fusion including QCD corrections by Michael Spira.
HLT	**H**igh **L**evel **T**rigger
HM	**H**umidity **M**easurement
HO	**H**adronic Calorimeter **O**uter Barrel
HPD	**H**ybrid **P**hoto **D**iode
HV	**H**igh **V**oltage
IDE	**I**ntegrated **D**evelopment **E**nvironment
IR	**I**nsertion **R**egion
IP	**I**nteraction **P**oint
IT	**I**nformation **T**echnology
JCOP	**J**oint **C**ontrols **P**roject
JES	**J**et **E**nergy **S**cale

JetMET	Group inside the CMS collaboration, which takes care of the jet reconstruction and the MET
LEP	**L**arge **E**lectron-**P**ositron Collider
LHC	**L**arge **H**adron **C**ollider
LHCb	**L**arge **H**adron **C**ollider-**b**eauty
LHCf	**L**arge **H**adron **C**ollider-**f**orward
LINAC2	**Lin**ear **Ac**celerator **2**
LO	**L**eading **O**rder
NLO	**N**ext to **L**eading **O**rder
LV	**L**ow **V**oltage
LSP	**L**ightest **S**upersymmetric **P**article
MC	**M**onte **C**arlo
MCFM	**M**onte **C**arlo for **FeM**tobarn processes. The program is designed to calculate cross-sections for various femtobarn-level processes at hadron-hadron colliders. For most processes, matrix elements are included at next-to-leading order and incorporate full spin correlations.
MET	**M**issing **T**ransverse **E**nergy
MoEDAL	**Mo**nopole and **E**xotics **D**etector **A**t the **L**HC
NTC	**N**egative **T**emperature **C**oefficient
ODBC	**O**pen **D**ata**b**ase **C**onnectivity
PC	**P**ersonal **C**omputer
PMT	**Ph**oot **M**ultiplier **T**ube
PLC	**P**rogramable **L**ogic **C**ontroller
PTHM	**P**recision **T**emperature and **H**umidity **M**easurement
PTM	**P**recision **T**emperature **M**easurement
PS	**P**roton **S**ynchrotron
PSB	**P**roton **S**ynchrotron **B**ooster
PVSS	**P**rocess **V**isualization and **S**teering **S**ystem

PYTHIA	A leading order event generator for a large number of physics processes.
QCD	**Q**uantum **C**hromo **D**ynamics
QED	**Q**uantum **E**lectro **D**ynamics
QFT	**Q**uantum **F**ield **T**heory
RF	**R**adio **F**requency
RFQ	**R**adio **F**requency **Q**uadrupole
RPC	**R**esistive **P**late **C**hamber
SCADA	**S**upervisory **C**ontrol **a**nd **D**ata **A**cquisition
SISCone	**S**eedless **I**nfrared **S**afe **Cone**
SM	**S**tandard **M**odel
SPS	**S**uper **P**roton **S**ynchrotron
SUSY	**S**uper**S**ymmetry
SVN	Apache **S**ub**versio**n
TCP/IP	**T**ransmission **C**ontrol **P**rotocol / **I**nternet **P**rotocol
TDR	**T**echnical **D**esign **R**eport
TEC	**T**racker **E**nd**C**ap
Tevatron	e$^+$ e$^-$ collider at Fermilab, Chicago
TIB	**T**racker **I**nner **B**arrel
TOB	**T**racker **O**uter **B**arrel
TOTEM	**TOT**al **E**lastic and diffractive cross section **M**easurement
VPT	**V**acuum **P**hoto **T**riode
UI	**U**ser **I**nterface

Bibliography

[1] L. R. Evans and P. Bryant, "LHC Machine," *J. Instrum.*, vol. 3, p. S08001. 164 p, 2008. This report is an abridged version of the LHC Design Report (CERN-2004-003).

[2] *Approval of the Large Hadron Collider and the Long-Term Scientific Programme of CERN*. 213th Meeting of Committee of Council, CERN, Feb 1994.

[3] *Large hadron collider: the experimental programme*. No. 621.384 LHC, CERN Library, 1993.

[4] O. S. Bruning, P. Collier, P. Lebrun, S. Myers, R. Ostojic, J. Poole, and P. Proudlock, *LHC Design Report - v.1 : the LHC Main Ring*. Geneva: CERN, 2004.

[5] O. S. Bruning, P. Collier, P. Lebrun, S. Myers, R. Ostojic, J. Poole, and P. Proudlock, *LHC Design Report - v.2 : the LHC Infrastructure and General Services*. Geneva: CERN, 2004.

[6] M. Benedikt, P. Collier, V. Mertens, J. Poole, and K. Schindl, *LHC Design Report - v.3 : the LHC Injector Chain*. Geneva: CERN, 2004.

[7] F. Bonaudi, "LEP - a status report," *Nuclear Physics B - Proceedings Supplements*, vol. 1, no. 2, pp. 199 – 206, 1988.

[8] The LEP Study Group, "LEP Design Report (2 volumes)," tech. rep., CERN, Geneva, 1984. Copies shelved as reports in LEP, PS and SPS libraries (CERN/LEP 84-01).

[9] T. Collaboration, "First measurement of the total proton-proton cross section at the LHC energy of 7 TeV," CERN-PH-EP-2011-158, Oct 2011.

[10] The ATLAS Collaboration, G. Aad et al, "The ATLAS Experiment at the CERN Large Hadron Collider," *J. Instrum.*, vol. 3, p. S08003. 437 p, 2008. Also published by CERN Geneva in 2010.

[11] The CMS Collaboration, S. Chatrchyan et al., "The CMS experiment at the CERN LHC," *J. Instrum.*, vol. 3, p. S08004, 2008. Also published by CERN Geneva in 2010.

[12] The LHCb Collaboration, A. Augusto Alves Jr et al, "The LHCb Detector at the LHC," *J. Instrum.*, vol. 3, p. S08005, 2008. Also published by CERN Geneva in 2010.

[13] The ALICE Collaboration, K. Aamodt et al, "The ALICE experiment at the CERN LHC," *J. Instrum.*, vol. 3, p. S08002. 259 p, 2008. Also published by CERN Geneva in 2010.

[14] The TOTEM Collaboration, G. Anelli et al, "The TOTEM Experiment at the CERN Large Hadron Collider," *J. Instrum.*, vol. 3, p. S08007, 2008.

[15] The LHCf Collaboration, O. Adriani et al, "The LHCf detector at the CERN Large Hadron Collider," *J. Instrum.*, vol. 3, p. S08006, 2008.

[16] The MoEDAL Collaboration, Pinfold at al, "Technical Design Report of the MoEDAL Experiment," Tech. Rep. CERN-LHCC-2009-006. MoEDAL-TDR-001, CERN, Geneva, Jun 2009.

[17] M. Bajko at al, "Report of the Task Force on the Incident of 19th September 2008 at the LHC," Tech. Rep. CERN-LHC-PROJECT-Report-1168, CERN, Geneva, Mar 2009.

[18] *Chamonix 2010 Workshop on LHC Performance*, no. CERN-ATS-2010-026, (Geneva), CERN, Jan 2010.

[19] *Chamonix 2011 Workshop on LHC Performance*, no. CERN-ATS-2011-005, (Geneva), CERN, Jan 2011.

[20] S. Myers, "The LHC Accelerator: Performance and Plans." to be published in proceedings of 22nd Rencontres de Blois on "Particle Physics and Cosmology", 2011.

[21] V. Khachatryan *et al.*, "CMS Tracking Performance Results from early LHC Operation," *Eur.Phys.J.*, vol. C70, pp. 1165–1192, 2010.

[22] S. Van der Meer, "Calibration of the effective beam height in the ISR," Tech. Rep. CERN-ISR-PO-68-31. ISR-PO-68-31, CERN, Geneva, 1968.

[23] CMS Collaboration, "Measurement of CMS Luminosity," *CMS-PAS-EWK-10-004*, 2010.

[24] CMS Collaboration, "Performance and Operation of the CMS Electromagnetic Calorimeter," *JINST*, vol. 5, p. T03010, 2010.

[25] A. Annenkov, M. Korzhik, and P. Lecoq, "Lead tungstate scintillation material," *Nucl.Instrum.Meth.*, vol. A490, pp. 30–50, 2002.

[26] P. Lecomte, D. Luckey, F. Nessi-Tedaldi, F. Pauss, and D. Renker, "Comparison between high-energy proton and charged pion induced damage in Lead Tungstate calorimeter crystals," 2007.

[27] CMS Collaboration, "Electromagnetic calorimeter commissioning and first results with 7 tev data," Tech. Rep. CERN-CMS-NOTE-2010-012, CERN, Geneva, Jul 2010.

[28] *The CMS electromagnetic calorimeter project: Technical Design Report.* Technical Design Report CMS, Geneva: CERN, 1997.

[29] M. Anfrevilleb, D. Bailleuxa, J. P. Bardb, A. Bornheima, C. Bouchand, E. Bougamont, M. Boyer, R. Chipaux, V. Daponte-Puill, M. Dejardin, J.-L. Faure, P. Gras, P. Jarry, C. Jeanney, A. Joudon, J.-P. Pansart, Y. Penichot, J. Rander, J. Rolquin, J.-M. Reymond, J. Tartas, P. Venault, P. Verrecchia, L. Zhang, K. Zhu, and R.-Y. Zhu, "Laser monitoring system for the cms lead tungstate crystal calorimeter," Tech. Rep. CMS-NOTE-2007-028. CERN-CMS-NOTE-2007-028, CERN, Geneva, Nov 2007.

[30] P. Adzic *et al.*, "Results of the first performance tests of the CMS electromagnetic calorimeter," *Eur.Phys.J.*, vol. C44S1, pp. 1–10, 2006.

[31] P. Milenovic at al., "Implementation and performance of the detector control system for the electromagnetic calorimeter of the CMS experiment," in *Proceedings of the International Conference on Accelerator and Large Experiments Control Systems*, (Knoxville, U.S.A.), October 2007.

[32] NTC thermistors 100K61A from Betatherm company,
Link: http://www.betatherm.com/, 2007.

[33] B. Hallgren et al., "The Embedded Local Monitor Board (ELMB) in the LHC Front-end I/O Control System," in *Proceedings of the 7th Workshop on Electronics for LHC Experiments*, (Stockholm, Sweden), September 2001.

[34] ETM professional control GmbH: PVSS (Prozess Visualisierungs und Steuerungs System) SCADA tool,
Link: http://www.etm.at, 2011.

[35] M. Beharrell et al., Technology Integration in the LHC experiments' Joint COntrols Project, CHEP'01, Beijing, September 2001.
Link: http://cern.ch/itco/Projects-Services/JCOP/.

[36] B. Franek and C. Gaspar, "SMI++ object oriented framework used for automation and error recovery in the LHC experiments," *J.Phys.Conf.Ser.*, vol. 219, p. 022031, 2010.

[37] O. Holme, D. Raphael, G. Dissertori, W. Lustermann, and S. Zelepoukine, "The evolution of the control system for the electromagnetic calorimeter of the compact muon solenoid experiment at the large hadron collider," Tech. Rep. CMS-CR-2011-195. CERN-CMS-CR-2011-195, CERN, Geneva, Sep 2011.

[38] EPCOS AG, NTC thermistor 470, R/T characteristic 8501, ordering code B57211V2471J060,
Link: http://www.epcos.com/.

[39] Siemens Industrial Automation: SIMATIC S7 PLC Family.
Link: http://www.automation.siemens.com/simatic/.

[40] P. Milenovic, J. Puzovic, D. Jovanovic, D. Maletic, G. Dissertori, *et al.*, "Performance of the CMS ECAL safety system for Super Modules SM0 and SM1," *Nucl.Instrum.Meth.*, vol. A554, pp. 427–436, 2005.

[41] RLE's patented Water Leak Detection Cable (SC), RLE's patented Water Leak Detection Cable (SC),
Link: http://rletech.com/product/conductive-fluid-sensing-cable/, 2007.

[42] Maxim Low Voltage CMOS Analog Multiplexer MAX 4582.
Data sheet: http://maxim.icfull.com/datasheet/MAX4581-MAX4583-PDF.html.

[43] Microchip PIC16F87x 28-40-pin 8-bit CMOS FLASH Microcontrollers,
Data Sheet: http://ww1.microchip.com/downloads/en/DeviceDoc/39564b.pdf.

[44] The Working Group on Programmable Logic Controllers (D. Blanc ST/CV, J. Brahy LHC/IAS, W. Heinze PS/CO, J.-M. Maugain EP/EOS, O. Van Der Vossen SL/CO, S. Waeffler EP/EOS, R. Rausch SL/CO), Recommendations for the use of PLC's at CERN, March 1997. Link: http://ab-div-co-is.web.cern.ch/ab-div-co-is/IndCtrl/PLC/RecommendationaPLCs.html.

[45] S. W. Smith, *The Scientist and Engineer's Guide to Digital Signal Processing.* California Technical Publishing, San Diego, California, second ed., 1999.

[46] K. M. Reichard, *Digital Filter Design, The Graduate Program in Acoustics.* The Pennsylvania State University, 2003.

[47] Z. Sméka, *Optimum Digital Filter Structure Design Based On Response To Initial Conditions.* ElectronicsLetter.com, December 2000.

[48] R. Rausch, "Qualification Of Electronics For The LHC Radiation Environment, EPAC.02, Paris, June 2002."
M. A. Rodrigez Ruiz, LHC/ACR/IN CERN, private communication.

[49] F. Piuz, F. Faccio, W. Snoeys, M. Campbell, J. Casas-cubillos, and P. Gomes, "Studying radiation tolerant ics for lhc." Jun 1997.

[50] E. Borchi and M. Bruzzi, "Radiation damage in silicon detectors," *Riv.Nuovo Cim.*, vol. 17N11, pp. 1–63, 1994.

[51] G. Hall, "Radiation resistance of semiconductor detectors and associated electronics," p. 14 p, Nov 1990.

[52] P. Adzic, A. Brett, F. Cavallari, D. Di Calafiori, E. Di Marco, *et al.*, "Detector control system for the electromagnetic calorimeter in the CMS experiment: Summary of the first operational experience," pp. 423–427, Proceedings of Topical Workshop On Electronics For Particle Physics TWEPP 2008, 15-19 Sep 2008, Naxos, Greece.

[53] W. Hollik, "Quantum field theory and the Standard Model," no. arXiv:1012.3883, 2010. Lectures given at the 2009 European School of High-Energy Physics, Bautzen, Germany, 14-27 Jun 2009.

[54] S. Weinberg, "A Model of Leptons," *Phys.Rev.Lett.*, vol. 19, pp. 1264–1266, 1967.

[55] P. W. Higgs, "Broken Symmetries and the Masses of Gauge Bosons," *Phys.Rev.Lett.*, vol. 13, pp. 508–509, 1964.

[56] P. W. Higgs, "Broken symmetries, massless particles and gauge fields," *Phys.Lett.*, vol. 12, pp. 132–133, 1964.

[57] P. W. Anderson, "Plasmons, gauge invariance, and mass," *Phys. Rev.*, vol. 130, pp. 439–442, 1963.

[58] F. Englert and R. Brout, "Broken symmetry and the masses of gauge vector mesons," *Phys. Rev. Lett.*, vol. 13, pp. 321–323, 1964.

[59] M. Kobayashi and T. Maskawa, "CP Violation in the Renormalizable Theory of Weak Interaction," *Prog.Theor.Phys.*, vol. 49, pp. 652–657, 1973.

[60] N. Cabibbo, "Unitary Symmetry and Leptonic Decays," *Phys.Rev.Lett.*, vol. 10, pp. 531–533, 1963.

[61] M. E. Peskin and D. V. Schroeder, *An Introduction to quantum field theory.* Addison-Wesley, 1995.

[62] M. Ahn *et al.*, "Measurement of Neutrino Oscillation by the K2K Experiment," *Phys.Rev.*, vol. D74, p. 072003, 2006.

[63] P. Adamson *et al.*, "Measurement of the neutrino mass splitting and flavor mixing by MINOS," *Phys.Rev.Lett.*, vol. 106, p. 181801, 2011.

[64] L. Reina, "Tasi 2004 lecture notes: Higgs boson physics. higgs boson physics," Tech. Rep. hep-ph/0512377. FSU-HEP-2005-12-30, Florida State Univ. Dept. Phys., Tallahassee, FL, Dec 2005.

[65] S. Weinberg, "Implication of dynamical symmetry breaking: an addendum," *Phys. Rev. D*, vol. 19, no. 4, pp. 1277–1280, 1979.

[66] S. Weinberg, "Implications of dynamical symmetry breaking," *Phys. Rev. D*, vol. 13, no. 4, pp. 974–996, 1976.

[67] C. T. Hill and E. H. Simmons, "Strong dynamics and electroweak symmetry breaking," *Phys. Rep.*, vol. 381, pp. 235–402. 280 p, Mar 2002.

[68] H. M. Georgi and S. L. Glashow, "Unity of all elementary-particle forces," *Phys. Rev. Lett.*, vol. 32, no. 8, pp. 438–441, 1974.

[69] S. K. Dimopoulos, S. Raby, and F. Wilczek, "Supersymmetry and the scale of unification," Tech. Rep. NSF-ITP-81-31, Calif. Univ. Santa Barbara. Inst. Theor. Phys., Santa Barbara, CA, Apr 1981.

[70] J. Buckley, E. Baltz, G. Bertone, K. Byrum, B. Dingus, *et al.*, "Section on Prospects for Dark Matter Detection of the White Paper on the Status and Future of Ground-Based TeV Gamma-Ray Astronomy," 2008. Report from the Dark Matter Science Working group of the APS commissioned White paper on ground-based TeV gamma ray astronomy.

[71] E. Komatsu *et al.*, "Seven-Year Wilkinson Microwave Anisotropy Probe (WMAP) Observations: Cosmological Interpretation," *Astrophys. J. Suppl.*, vol. 192, p. 18, 2011.

[72] W. J. Percival, R. C. Nichol, D. J. Eisenstein, J. A. Frieman, M. Fukugita, *et al.*, "The shape of the SDSS DR5 galaxy power spectrum," *Astrophys.J.*, vol. 657, pp. 645–663, 2007.

[73] S. P. Martin, "A Supersymmetry primer," 1997.

[74] I. J. R. Aitchison, *Supersymmetry in particle physics: an elementary introduction.* Cambridge: Cambridge University Press, 2007.

[75] S. Weinberg, *The quantum theory of fields.* Cambridge: Cambridge University Press, 2000.

[76] G. L. Kane, *Perspectives on supersymmetry II.* Advanced series on directions in high energy physics, Singapore: World Scientific, 2010.

[77] G. Bayatian *et al.*, "CMS technical design report, volume II: Physics performance," *J.Phys.G*, vol. G34, pp. 995–1579, 2007.

[78] W. Beenakker, R. Hopker, and M. Spira, "PROSPINO: A Program for the production of supersymmetric particles in next-to-leading order QCD," 1996.

[79] H.-C. Cheng, K. T. Matchev, and M. Schmaltz, "Bosonic supersymmetry? Getting fooled at the CERN LHC," *Phys.Rev.*, vol. D66, p. 056006, 2002.

[80] J. Almeida, F.M.L., Y. D. A. Coutinho, J. A. Martins Simoes, P. Queiroz Filho, and C. Porto, "Same sign dileptons as a signature for heavy Majorana neutrinos in hadron hadron collisions," *Phys.Lett.*, vol. B400, pp. 331–334, 1997.

[81] R. Contino and G. Servant, "Discovering the top partners at the LHC using same-sign dilepton final states," *JHEP*, vol. 0806, p. 026, 2008.

[82] Y. Bai and Z. Han, "Top-antitop and Top-top Resonances in the Dilepton Channel at the CERN LHC," *JHEP*, vol. 0904, p. 056, 2009.

[83] Y. Mambrini and B. Zaldivar, "When LEP and Tevatron combined with WMAP and XENON100 shed light on the nature of Dark Matter," 2011.

[84] O. L. Buchmuller, R. Cavanaugh, A. de Roeck, J. R. Ellis, H. Flacher, S. Heinemeyer, G. Isidori, K. A. Olive, P. Paradisi, F. J. Ronga, and G. Weiglein, "Predictions for Supersymmetric Particle Masses using Indirect Experimental and Cosmological Constraints," *J. High Energy Phys.*, vol. 09, Sep 2008.

[85] G. L. Kane, C. F. Kolda, L. Roszkowski, and J. D. Wells, "Study of constrained minimal supersymmetry," *Phys.Rev.*, vol. D49, pp. 6173–6210, 1994.

[86] M. Davier, A. Hoecker, B. Malaescu, and Z. Zhang, "Reevaluation of the Hadronic Contributions to the Muon g-2 and to alpha(MZ)," *Eur.Phys.J.*, vol. C71, p. 1515, 2011.

[87] G. Bennett *et al.*, "Final Report of the Muon E821 Anomalous Magnetic Moment Measurement at BNL," *Phys.Rev.*, vol. D73, p. 072003, 2006. Summary of E821 Collaboration measurements of the muon anomalous magnetic moment, each reported earlier in Letters or Brief Reports. Revised version submitted to Phys.Rev.D.

[88] K. Nakamura *et al.*, "Review of particle physics," *J.Phys.G*, vol. G37, p. 075021, 2010.

[89] A. Abulencia *et al.*, "Inclusive search for new physics with like-sign dilepton events in $p\bar{p}$ collisions at $\sqrt{s} = 1.96$-TeV," *Phys.Rev.Lett.*, vol. 98, p. 221803, 2007.

[90] V. Abazov *et al.*, "Search for associated production of charginos and neutralinos in the trilepton final state using 2.3 fb^{-1} of data," *Phys.Lett.*, vol. B680, pp. 34–43, 2009.

[91] J. Yamaoka, "SUSY searches at the Tevatron," *J.Phys.Conf.Ser.*, vol. 259, p. 012020, 2010.

[92] V. Abazov *et al.*, "Search for squarks and gluinos in events with jets and missing transverse energy using 2.1 fb^{-1} of $p\bar{p}$ collision data at $\sqrt{s} = 1.96$- TeV," *Phys.Lett.*, vol. B660, pp. 449–457, 2008.

[93] W. Adam, B. Mangano, T. Speer, and T. Todorov, "Track reconstruction in the CMS tracker," CMS-NOTE-2006-041, 2005.

[94] W. Adam, R. Frühwirth, A. Strandlie, and T. Todor, "Reconstruction of electrons with the gaussian-sum filter in the cms tracker at the lhc," Tech. Rep. CMS-NOTE-2005-001. CERN-CMS-NOTE-2005-001, CERN, Geneva, Jan 2005.

[95] CMS Collaboration, "Commissioning of the Particle-flow Event Reconstruction with the first LHC collisions recorded in the CMS detector," *CMS-PAS-PFT-10-001*, 2010.

[96] CMS Collaboration, "Electron reconstruction and identification at sqrt(s) = 7 TeV," *CMS-PAS-EGM-10-004*, 2010.

[97] CMS Collaboration, "Performance of muon identification in pp collisions at 7 TeV," *CMS-PAS-MUO-10-002*, 2010.

[98] G. Dissertori, I. G. Knowles, and M. Schmelling, *Quantum chromodynamics: high energy experiments and theory*, vol. 115, reprint of *International series of monographs on physics*. Oxford: Oxford University Press, 2009.

[99] CMS Collaboration, "Jet Performance in pp Collisions at 7 TeV," *CMS-PAS-JME-10-003*, 2010.

[100] CMS Collaboration, "The Jet Plus Tracks Algorithm for Calorimeter Jet Energy Corrections in CMS," *CMS-PAS-JME-09-002*, 2009.

[101] CMS Collaboration, "Particle-Flow Event Reconstruction in CMS and Performance for Jets, Taus, and MET," *CMS-PAS-PFT-09-001*, Apr 2009.

[102] M. Cacciari, G. P. Salam, and G. Soyez, "The Anti-k(t) jet clustering algorithm," *JHEP*, vol. 0804, p. 063, 2008.

[103] CMS Collaboration, "Calorimeter Jet Quality Criteria for the First CMS Collision Data," *CMS-PAS-JME-09-008*, Apr 2010.

[104] CMS Collaboration, "Jet Energy Corrections determination at 7 TeV," *CMS-PAS-JME-10-010*, 2010.

[105] CMS Collaboration, "Missing transverse energy performance of the CMS detector," 2011.

[106] "Measuring electron efficiencies at cms with early data," CERN-CMS-PAS-EGM-07-001, 2008.

[107] H. Bakhshian et al, "Computing the contamination from fakes in leptonic final states." CERN-CMS-AN-2010-261, September 2010.

[108] CMS Collaboration, "Search for new physics with same-sign isolated dilepton events with jets and missing transverse energy at the LHC," *JHEP 1106:077 (2011)*, Apr 2011.

[109] H. Bakhshian et al, "Same-sign dilepton search for supersymmetry in the first 35 pb^{-1} of 7 TeV pp collisions." CERN-CMS-AN-2010-375, November 2010.

[110] H.-L. Lai, J. Huston, Z. Li, P. Nadolsky, J. Pumplin, *et al.*, "Uncertainty induced by QCD coupling in the CTEQ global analysis of parton distributions," *Phys.Rev.*, vol. D82, p. 054021, 2010.

[111] CMS Collaboration, "Jets in 0.9 and 2.36 TeV pp Collisions," *CMS-PAS-JME-10-001*, 2010.

[112] B. Allanach, "SOFTSUSY: a program for calculating supersymmetric spectra," *Comput.Phys.Commun.*, vol. 143, pp. 305–331, 2002.

[113] M. Muhlleitner, A. Djouadi, and Y. Mambrini, "SDECAY: A Fortran code for the decays of the supersymmetric particles in the MSSM," *Comput.Phys.Commun.*, vol. 168, pp. 46–70, 2005.

[114] T. Sjostrand, S. Mrenna, and P. Z. Skands, "PYTHIA 6.4 Physics and Manual," *JHEP*, vol. 0605, p. 026, 2006.

[115] P. M. Nadolsky, H.-L. Lai, Q.-H. Cao, J. Huston, J. Pumplin, *et al.*, "Implications of CTEQ global analysis for collider observables," *Phys.Rev.*, vol. D78, p. 013004, 2008.

[116] CMS Collaboration, "Search for new physics with same-sign isolated dilepton events with jets and missing energy." CMS-PAS-SUS-11-010, 2011.

[117] CMS Collaboration, "Measurement of the Underlying Event Activity with the Jet Area/Median Approach at 0.9 TeV." CMS-PAS-QCD-10-005, 2010.

[118] CMS Collaboration, "Search for new physics with same-sign isolated dilepton events with jets and missing energy," in *Proceedings of the EPS Conference in High Energy Physics*, (Grenoble, France), 2011. CMS-PAS-SUS-11-010.

[119] R. Acquafredda *et al.*, "First events from the CNGS neutrino beam detected in the OPERA experiment," *New J.Phys.*, vol. 8, p. 303, 2006.

[120] RH sensors UPS-600 from Ohmic instruments, Link: http://www.cweb5.com/ohmic/, 2007.

[121] G. 't Hooft, "Renormalization of Massless Yang-Mills Fields," *Nucl.Phys.*, vol. B33, pp. 173–199, 1971.

[122] F. Englert and R. Brout, "Broken Symmetry and the Mass of Gauge Vector Mesons," *Phys.Rev.Lett.*, vol. 13, pp. 321–322, 1964.

[123] S. Glashow, J. Iliopoulos, and L. Maiani, "Weak Interactions with Lepton-Hadron Symmetry," *Phys.Rev.*, vol. D2, pp. 1285–1292, 1970.

[124] S. Glashow, "Partial Symmetries of Weak Interactions," *Nucl.Phys.*, vol. 22, pp. 579–588, 1961.

[125] H. Fritzsch, M. Gell-Mann, and H. Leutwyler, "Advantages of the Color Octet Gluon Picture," *Phys.Lett.*, vol. B47, pp. 365–368, 1973. Introduces the term 'color'.

[126] H. Politzer, "Reliable Perturbative Results for Strong Interactions?," *Phys.Rev.Lett.*, vol. 30, pp. 1346–1349, 1973.

[127] D. Gross and F. Wilczek, "Ultraviolet Behavior of Nonabelian Gauge Theories," *Phys.Rev.Lett.*, vol. 30, pp. 1343–1346, 1973.

[128] D. Gross and F. Wilczek, "Asymptotically Free Gauge Theories. 1," *Phys.Rev.*, vol. D8, pp. 3633–3652, 1973.

[129] F. Gianotti, "Collider physics: LHC," in *Proceedings of the European School Of High-Energy Physics ESHEP 99*, CERN-OPEN-2000-293, 2000.

[130] T. S. Pettersson and P. Lefèvre, "The Large Hadron Collider: Conceptual Design," Tech. Rep. CERN-AC-95-05 LHC, CERN, Geneva, Oct 1995.

[131] G. Giudice, R. Rattazzi, and J. Wells, "Quantum gravity and extra dimensions at high-energy colliders," *Nuclear Physics B*, vol. 544, no. 1-2, pp. 3–38, 1999.

[132] G. Giudice, *A zeptospace odyssey: a journey into the physics of the LHC*. Oxford Univ Pr, 2010.

[133] G. L. Kane, *Perspectives on LHC physics*. New Jersey, N.J.: World Scientific, 2008.